The Impact of Topography and Albedo on Weather Patterns and the Location of the Martian South Polar CO_2 Ice Cap

Farahnaz Fazel Rastgar

A dissertation submitted to the Faculty of Graduate Studies in partial fulfillment of the requirements for the degree of

Doctor of Philosophy

Graduate Programme in Earth and Space Science
York University
Toronto, Ontario

May 2013

Abstract

Meteorological and physical results from the second version of Global Mars Multiscale Model (GM3-v2) were used to investigate the impact of topography and albedo on the Martian southern polar CO_2 ice cap. Analysis of the numerical simulations revealed significant differences in the horizontal and vertical cross sections of temperature when model was run for plain topography.

Wind streamlines from Ls = 20° (early southern fall) to Ls = 200° (early southern spring) for every one Ls have been analysed. Wind streamline pattern analysis shows there are two cyclonic circulations during southern winter; one around the Hellas basin (in the eastern hemisphere) and the second one around the Argyre basin (in the western hemisphere). However, between these two cyclonic cells, the pattern is anti-cyclonic.

Since the albedo map which is used in the model represents a mean state of albedo for all seasons of the planet, the albedo values have been modified in the polar regions to allow for the formation of the surface ice in the model. Also this modification will be very important in the water cycle simulation. As a second step in this work, the albedo values at the poles (mostly focusing on south polar regions) were modified for a better representation of the physical situation.

However, the seasonal carbon dioxide ice in the polar regions is presented in the surface ice simulation by the second version of Global Mars Multiscale Model, but it does not produce a permanent south CO_2 ice cap, and so it must be modified in the physics code in order to capture the real physical and meteorological processes. The permanent south CO_2 ice cap in the model can significantly improve the representation of south polar

meteorology for example in predicted surface temperatures, surface pressures, horizontal and zonal winds over the south cap and also possible initiation of dust storms at south polar region during the southern summer period. In the final part to this thesis, the residual CO_2 ice cap is simulated in the physics code.

Dedication

This dissertation is dedicated to my mother (May she rest in peace), my dear and loving husband Abbas and my sweet daughter Farnaz who have loved and supported me always in my life.

Acknowledgements

I would like to express my deep and sincere gratitude to my supervisor, Professor Jack McConnell, who was very supportive, informative and patient all these years (May he rest in peace). Thanks to Dr. Deji Akingunnola for helping me to work with the second Generation of Mars Multiscal Model. It is my pleasure to thank all the members of our research group specially Farisa, Di, Jeniffer, Alex, Kirill, Jacek, Abdulla, Jin and Kenjiro. I am very thankful to my supervisory committee members, Professor Peter Taylor and Professor Jim Whiteway for serving on my advisory committee. Special thanks go to Professor Peter Taylor for working with me to complete my thesis revisions. Also I am very grateful to all my examiner members Professor Jim Murphy, Professor Tom McElroy, Professor Jim Whiteway and Professor John Moores for their detailed review and constructive comments. I am very thankful to Prof. Jim Murphy for introducing me some recent published papers. Thanks to Prof. Sunil Bisnath, Graduate Program Director of Earth and Space Science and Engineering. Also thanks to Marcia Gaynor, Paola Panaro, and the rest of the administrative assistant staff, for their assistance throughout my time here. I also wish to express my gratitude to York University for financial support.

Table of Contents

List of Tables

List of Figures

Chapter 1

Introduction and Objectives

1 Mars

Mars is the fourth planet from the Sun and, sharing many common aspects with Earth, it is of interest to understand its climate processes. There has been an increase in scientific understanding of the Martian atmosphere which dates back to the early 1960s, both from a theoretical and observational perspective. The first spacecraft to fly past Mars was Mariner 4 in 1965. Mariner 4 provided close range images of the surface in the hopes of revealing geologic and atmospheric processes. Mariner 6 and Mariner 7 were launched on February 24, 1969 and March 27, 1969, respectively. The main objectives of these missions were measurement of atmospheric composition, pressure, density, and temperature. Mariner 8 (also called Mariner H) was designed to be the first American spacecraft to study Mars from orbit. It was launched on May 08, 1971 but fell with technical problem shortly after launch. Mariner 9 arrived in Mars orbit on November 14,

1971 and provided the most complete view of Mars. Atmospheric structure, composition, density and pressure were to be analyzed using an infrared radiometer, an ultraviolet spectrometer and interferometer similar to those used on previous Mars Mariner missions. This mission mapped over 70% of the Martian surface with resolutions ranging from 1 km per pixel to 100 m per pixel during successive Mars orbits from an altitude of about 1,500 km. Mars' two moons, Phobos and Deimos, were also be analyzed by Mariner 9. The information acquired from this mission would later serve as the foundation for the Viking program.

NASA's Viking Mission to Mars was composed of two spacecraft, Viking 1 and Viking 2, each consisting of an Orbiter and a Lander. Viking 1 was launched on August 20, 1975 and arrived at Mars on June 19, 1976. Viking 2 was launched September 9, 1975 and entered Mars orbit on August 7, 1976. The primary objectives of this mission were to obtain high resolution images of the Martian surface, characterize the structure of the atmosphere and composition of the atmosphere and surface, and search for evidence of life by taking surface samples and analyzing them for composition. Simultaneously, the Viking 1 and 2 Orbiters studied Mars from orbit for six and four years respectively returning many images of the surface and information on the atmosphere of Mars. The two Viking Landers were the longest surviving active laboratories on the surface of Mars at that time. Years later, the Mars Pathfinder spacecraft landed on the surface of Mars on July 4, 1997 (Schofield et al., 1997) and its final data transmission was on September 27, 1997. Mars Global Surveyor (MGS) was the next successful U.S. mission launched to

Mars since the Viking mission in 1976. Mars Global Surveyor arrived in September 11, 1997 (September 12, UTC) and started its science orbit phase in March 1999. It collected data on the surface morphology, topography, composition, gravity, atmospheric dynamics and magnetic field by its scientific instruments such as MOC (Mars Orbiter Camera), MOLA (Mars Orbiter Laser Altimeter), TES (Thermal Emission Spectrometer), MAG/ER and RADIO SCIENCE (Gravity Field Experiment). After nearly a decade of discovery, MGS went silent in November, 2006.

Mars Odyssey was launched April 7, 2001 and reached Mars on October 24, 2001. Its primary science mission continued through August 2004. Still in orbit around Mars, NASA's 2001 Mars Odyssey spacecraft has collected thousands of images and continues to send information to Earth about Martian geology, climate, and mineralogy. Measurements by Odyssey have enabled scientists to create maps of minerals and chemical elements and identify regions with buried water ice. Images that measure the surface temperature have provided fantastic views of Martian topography.

Mars Express is Europe's first spacecraft to the Red Planet. Mars Express travelled to Mars in seven months arriving in Mars orbit on 25 December 2003. It carried seven instruments and a Lander. The orbiter instruments are remotely investigating the Martian atmosphere, surface and subsurface. However, the landing perform was not successful and the lander was lost The Mars Express objectives were to search for subsurface water from orbit and release a Lander to reach the Martian surface. The orbiter is now studying the Martian atmosphere, the planet's structure and its geology. The Mars

Reconnaissance Orbiter (MRO) was launched on August 12, 2005 and attained Martian orbit on March 10, 2006. The instruments zoom in for extreme close-up photography of the Martian surface, analyze minerals, look for subsurface water, how much dust and water are distributed in the atmosphere and monitor daily, global weather. The mission is examining whether underground Martian ice discovered by the Mars Odyssey orbiter is the top layer of a deep ice deposit or a shallow layer in equilibrium with the atmosphere and its seasonal cycle of water vapour. On May 25 2008 the NASA/JPL Phoenix Scout spacecraft descended to the Martian north polar surface. The mission had two main objectives. The first one was to study the geologic history of water, the key factor to understanding past climate change. The second goal was to evaluate past or potential planetary habitability in the ice-soil boundary. The Lander was supposed to complete its mission in August 2008 but it continued operating for ~ 150 sols which extended in to October 2008. On Nov. 9, 2011 a Zenit rocket was launched into space carrying Russia's Phobos-Grunt spacecraft to Mars on a mission to collect samples of the Martian moon Phobos. But it crashed and failed in its Mission to Mars' Moon.

Finally, the Mars Science Laboratory (MSL or Curiosity) is a Mars rover launched by NASA on Nov. 26, 2011. It successfully landed in Gale Crater on August 6, 2012. The rover's objectives are searching for past and present life, studying the Martian climate and geology, and collecting data for a future manned mission to Mars. In addition to direct observations (in situ and remote) and laboratory experiments, numerical studies with a

variety of Mars Global Climate Models (GCMs) have provided some understanding of the Martian atmosphere. Table 1.1 shows a chronology of these developments.

Table 1.1: A Chronology of the Development of an Understanding of Mars (http://spacescience.arc.nasa.gov/mars-climate-modeling-group/)

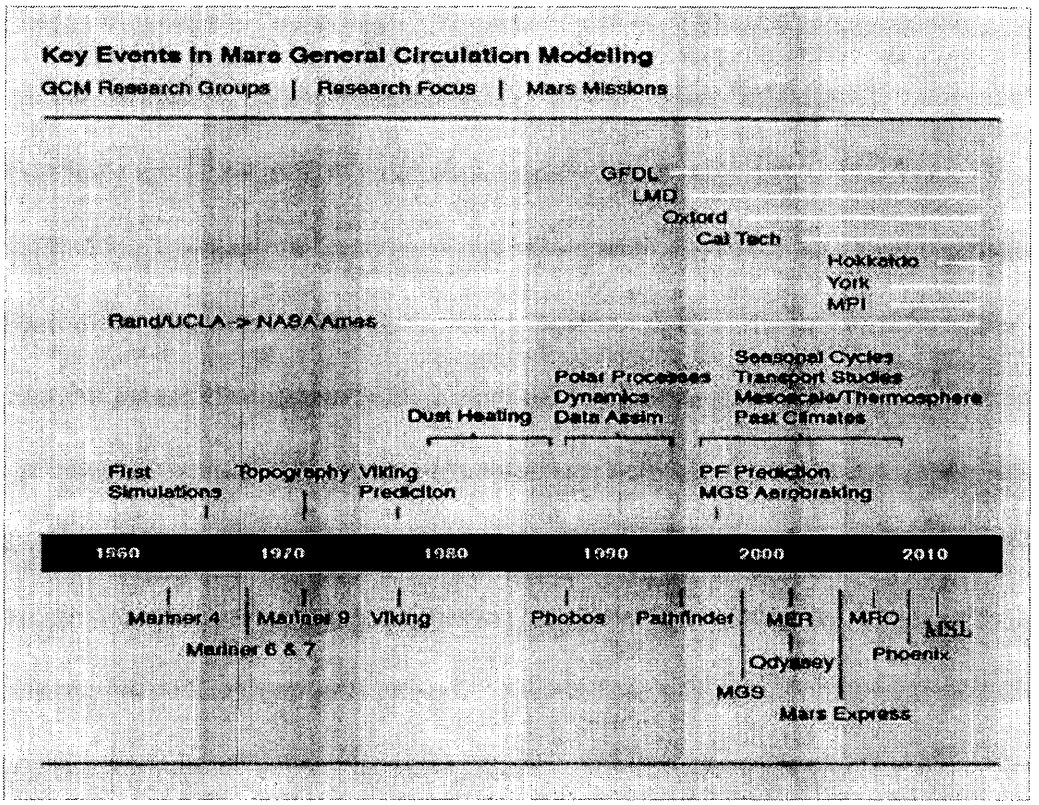

Mars is a planet almost like the Earth, of nearly half the size, similar orbital and rotational parameters, possessing an atmosphere, weather and climate phenomena and also with a solid surface. For example, the obliquity of Earth is 23.93° whereas it is 25.19° for Mars. However, Mars has significant orbital eccentricity 0.093 rather than 0.017 for Earth (Read and Lewis, 2004). The large Martian eccentricity causes the solar insolation (a measure of solar radiation energy received on a given surface area and

recorded during a given time in units of Watts per square metre on Mars to vary by 40% as the planet orbits the Sun as compared to 7% for the Earth. Because the Martian orbit has large differences in the distance from the sun, the surface of Mars can experience larger changes in temperature than does the Earth. As for the Earth, Mars' obliquity dominates the seasons, but, because of the large eccentricity (the difference between the elliptical shape of the Martian orbit and a perfect circle), southern winters are very cold and long while those in the north hemisphere are warm and short. Mars rotates about its axis with a period of approximately 37 minutes and 22 seconds longer than the length of day on Earth. It has a minimum distance of 1.38 AU[1] at the perihelion; and a maximum distance of 1.66 AU at the aphelion. Its orbital period is longer than Earth's being about 686.98 Earth days or 668.6 sols (Figure 1.1). Surface gravity on Mars is about one third that on Earth. Table 1.2 shows a comparison of some important parameters between Mars and Earth (Read and Lewis, 2004).

[1]One astronomical Unit is about 149.6 million kilometres, the mean distance from the earth to the sun.

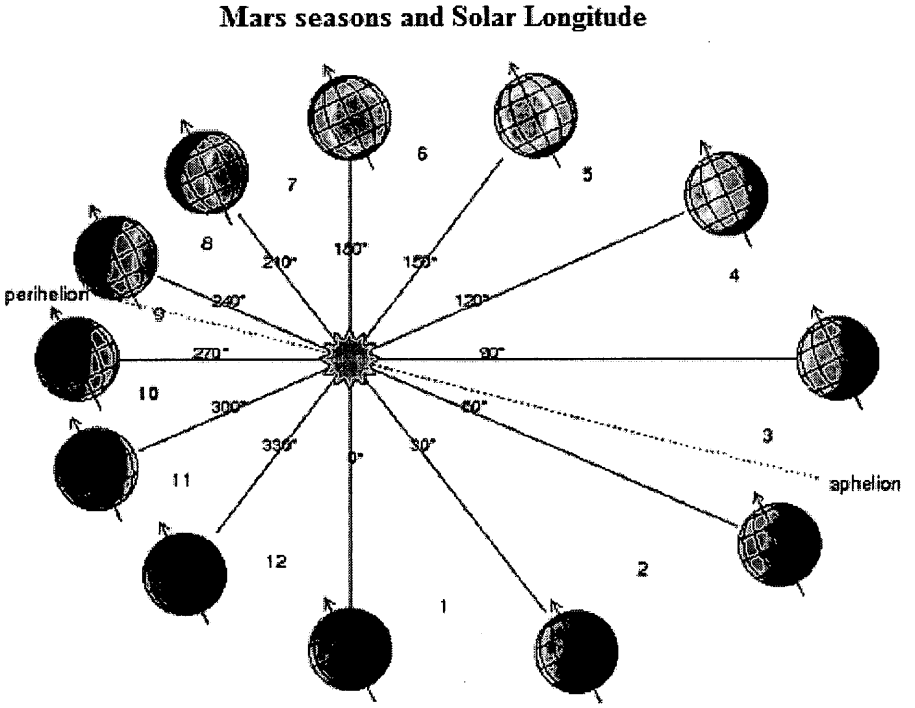

Figure 1.1: This figure shows the relative Mars position in its orbit from Sun. The aphelion occurs at Ls = 71° whereas the position of perihelion at Ls = 251°. (http://www-mars.lmd.jussieu.fr/mars/time/solar_longitude.html).

1.1 Mars Topography

Figure 1.2 shows the northern and southern Polar Cap topography (top) and the global topography (bottom) given by the Mars Orbiter Laser Altimeter from MGS (Smith, et al., 1999). Mars has large scale topographical structures such as deep valleys and high mountains which may have an important role in Martian weather. The most important topographical feature shown in the lower image is the Hellas basin centred at (42.7°S,

70°E) in the southern hemisphere which is nearly nine kilometres relief and 2,300 km in diameter (Leonard and Tanaka, 2001). Mars also has mountainous terrain including the volcano Olympus Mons at a height of nearly 22 km and about 600 km wide at (18.4°N , 226°E), which is roughly three times as tall as Mount Everest and the largest one in the solar system (Plescia, 2004).

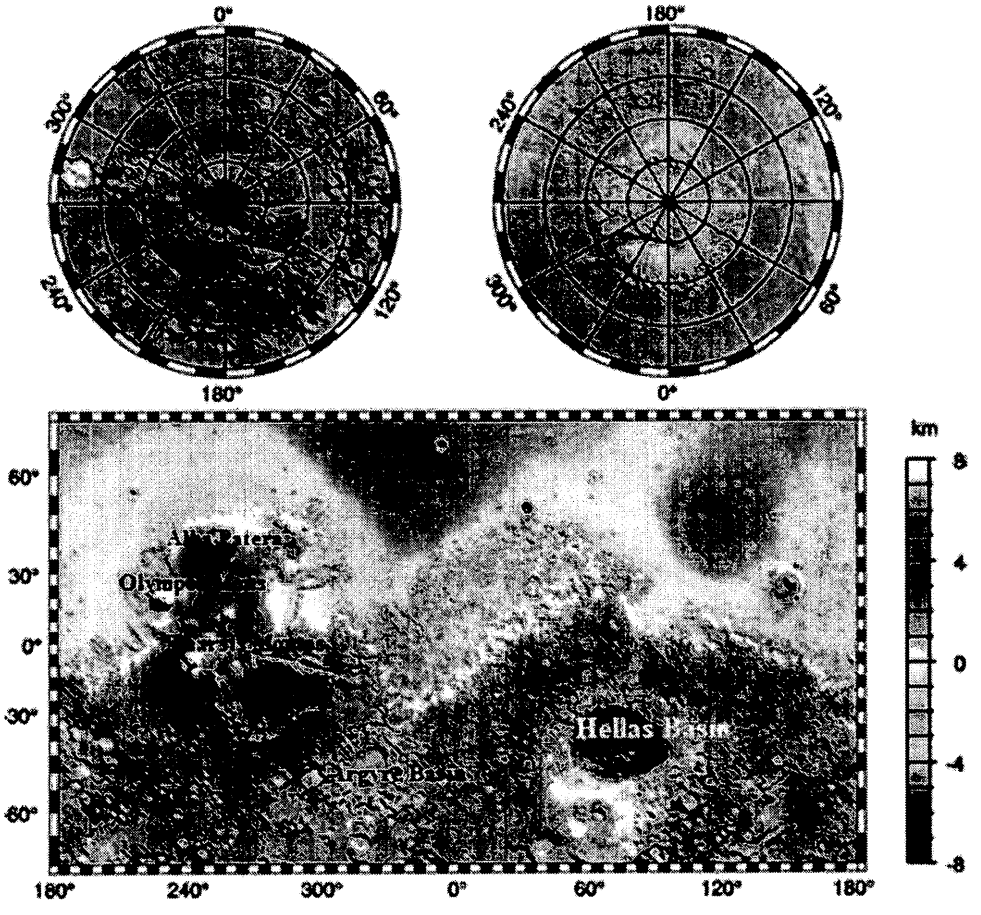

Figure 1.2: Martian south and north polar cap topography (top) and Global topography (bottom) given from NASA/MGS/MOLA (Smith et al., 1999).

1.2 The Martian Atmosphere

Compared to the Earth, Mars has a very thin and cold atmosphere composed (by volume) of 95% carbon dioxide, 2.7% nitrogen, 1.6% argon and contains traces of oxygen, water and carbon monoxide (Table 1.2). The Martian atmosphere differs from Earth in its very low surface pressure. Martian mean surface pressure is nearly 600 Pa (Read and Lewis, 2004; Kieffer et al., 1992) whereas mean surface pressure for Earth is around 985 hPa. This is in contrast to mean sea-level (MSL) pressure, which involves the extrapolation of pressure to sea-level for locations above or below sea-level. The average pressure at mean sea-level in the International Standard Atmosphere is 1013.25 hPa. The global increase from mean Martian surface pressure is about 13% between northern winter and spring (with the maximum during early southern summer) while the global decrease from mean surface pressure is nearly 14% between northern spring and summer (Woiceshyn, 1974). These pressure oscillations are correlated with the seasonal growth and decay of the CO_2 polar ice caps. The Martian atmosphere is very dry as compared to that of the Earth, with average concentrations of water vapour being (in molar fraction) less than 0.00003, whereas on Earth water vapour is always present in the air having an average molar fraction of around 0.01 (Table 1.2). However, the content of water vapour in the Earth's atmosphere may vary and the maximum amount possible of water vapour in air[2] depends on the temperature of the air. Even with the limited atmospheric water

[2]Dry air in the atmosphere of Earth contains roughly (by volume) 78.084% Nitrogen, 20.946% Oxygen, 0.9340% Argon, 0.03697% carbon dioxide and small amounts of other gases. Air also contains a variable amount of water vapour, on average around 1% (Christopherson, 2003).

vapour content on Mars, the small amount can condense and form high level water ice clouds (Heavens et al., 2010). Clouds can exist as both water ice and Carbon dioxide ice clouds (Montmessin et al., 2006). Clouds composed of CO_2 ice form when CO_2 gas condenses out in the atmosphere. The CO_2 ice clouds have been observed in the lower Martian atmosphere in the winter polar night of both northern and southern hemispheres (Pettengill and Ford, 2000), and in Mars mesosphere (around 80-100 km altitude) near the equator (Montmessin et al. 2006). The formation of CO_2 ice clouds in the northern winter polar atmosphere are also linked to baroclinic planetary waves (Kuroda et al., 2013). With the exception of some areas over Hellas basin where the pressure can exceed 600 Pa, over much of Mars the temperatures are below the triple point of water on the phase diagram for atmospheric conditions. This means that if the temperature reaches the normal freezing point of water, about 273 K, ice would directly sublime into water vapour (Figure 1.3).

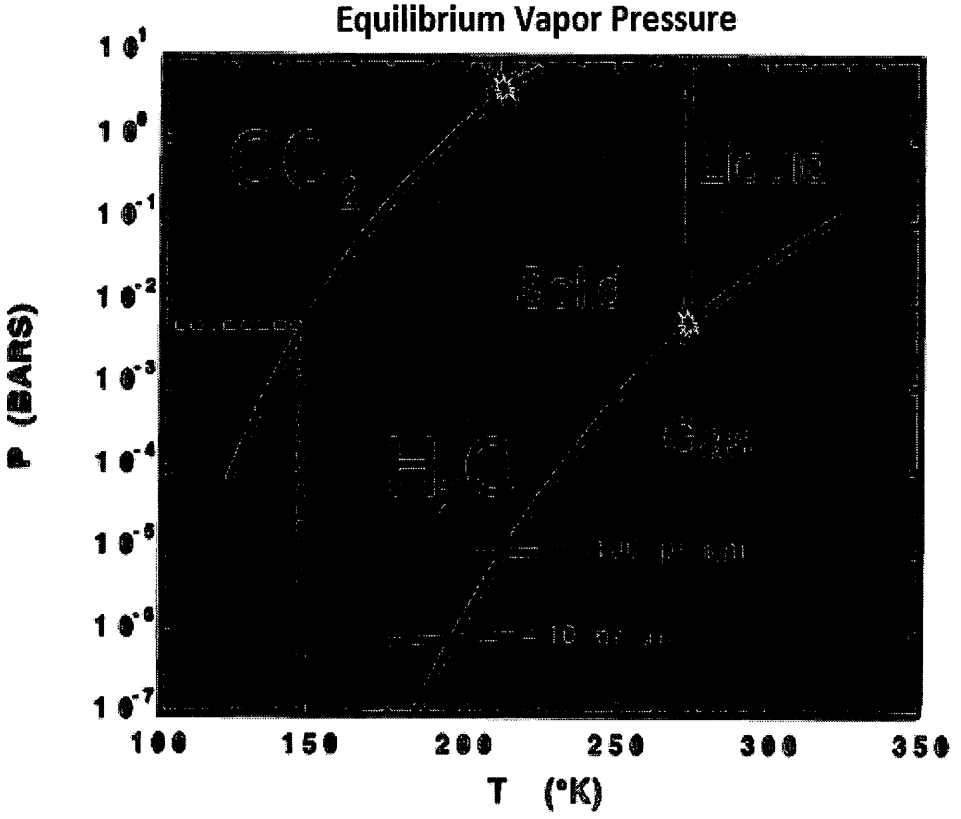

Figure 1.3: This figure shows the equilibrium vapour pressure for CO_2 and H_2O. The triple point of CO_2 is 216 K and the vapour pressure at the Martian cap is around 600 Pa (Figure from Thomas, 2010).

The Martian atmospheric circulation is driven by differential equator-pole heating from the Sun, balanced by infrared cooling from its surface and atmosphere. During Martian solstice seasons, the ascending and descending branches of the single Hadley cell are displaced much farther from the equator (30°-60° latitudes). But only near the equinox two weak, equatorially symmetric, Hadley cells occur on Mars (Jakosky and Haberle, 1992). The general circulation patterns in the atmosphere of Mars have many differences from those of the Earth. The atmosphere of Mars has a short radiative

response time of ~ $2x10^5$ s (~ 1/20 for Earth). Also the surface thermal inertia (a measure of the response of the surface for the change in thermal regime) is low (Kieffer et al., 1977). There are large changes in Martian surface pressure since condensation and sublimation of a large fraction of the atmospheric CO_2 mass occurs on Mars. Earth's primary gases N_2 and O_2, do not similarly condense. Mars's large eccentricity causes the planet to receive different amounts of the Sun's energy by the changes in its distance from the Sun. Solar insolation on Mars is about 44% more at perihelion than at aphelion (Glasstone, 1968). Also large scale dust storms occur on Mars mostly during southern summer, when Mars is closest to the sun and absorbs more solar energy (Forget, 2007). All of these factors cause significant variation on daily, monthly, seasonal, and inter-annual timescales in the Martian atmospheric circulation which are greater than those which are observed in the Earth's troposphere (Zurek et al., 1992).

Table 1.2: Important parameters for Earth and Mars (Read and Lewis, 2004)

	Earth	Mars
Mean orbital radius (10^{11}m)	1.5	2.28
Distance from Sun (AU)	0.98-1.02	1.38-1.67
Orbital eccentricity	0.017	0.093
Orbital inclination (deg)	0.000	1.850
L_s of perihelion	281	251
Planetary obliquity	23.45	25.19
Rotation rate, Ω ($10^{-5}s^{-1}$)	7.294	7.088
Solar day (s)	86,400	88,775
Year length (sol)	355.46	668.6
Year length (Earth days)	365.24	686.98
Equatorial radius (10^6 m)	6.378	3.396
Surface gravity, g (ms^{-2})	9.81	3.72
Representative Surface pressure (pa)	101,300 (M.S.L.)	600(variable)
Atmospheric constituents (molar ratio); dry air sample in Earth	N_2 (77%) O_2 (21%) H_2O (1%) Ar (0.9%)	CO_2 (95%) N_2 (2.7%) Ar (1.6%) O_2 (0.13%)
Specific Gas constant R ($m^2s^{-2}K^{-1}$)	287	200
Mean Solar Constant (Wm^{-2})	1367	589
Specific heat at constant pressure, C_p ($m^2s^{-2}K^{-1}$)	1000	860
Bond Albedo[3]	0.306	0.25
Effective temperature (K)	256	210
Surface temperature (K)	230-315	140-290
Scale Height, $H=RT_e/g$ (km)	7.5	10.8
Dry adiabatic lapse rate ($-g/C_p$) (K km^{-1})	9.8	4.3
Buoyancy frequency, N (10^{-2} s^{-1})	1.1	0.6
Deformation Radius, $L=NH/\Omega$ (km)	1100	920
Typical zonal wind at jet level (m/s)	30	80 (data from Oxford MGCM)

[3]Bond albedo is the fraction of power in the total electromagnetic radiation incident on an astronomical body that is scattered back out into space. It takes into account all wavelengths at all phase angle.

1.3 Mars Polar Caps

Mars, like Earth, has polar caps, one in the north and one in the south, but the difference is that the Earth's polar ice caps are mainly water ice, while Mars' caps are a mixture of carbon dioxide and water ice. There are two kinds of ice caps on Mars: seasonal carbon dioxide ice caps and residual or permanent ice caps. Seasonal ice caps accumulate during the winter season and sublime during the summer but the residual caps remain during the entire year. The residual north polar cap is mostly made of water ice while the residual south polar cap is made of both water ice and carbon dioxide. Mars has a 95% CO_2 atmosphere where approximately 30% condenses at each polar surface during fall and winter seasons when the temperature falls below ~148 K, the carbon dioxide frost point (James et al., 1992; Forget, 1998). Since the southern winter occurs during aphelion, the atmospheric pressure is lower as more CO_2 condenses onto the surface compared to the northern winter. Also southern winters are much colder than the northern winters as Mars is further from the Sun at that time of the Mars year. On the other hand, the southern summers (~154 sols) are shorter but more intense than the northern summers (~178 sols) since at this time Mars is closest to the Sun (perihelion). So, the north seasonal carbon dioxide ice cap completely sublimates during northern summer, leaving only the residual underlying water ice cap (Forget, 2007). The residual south polar cap experiences a shorter summer, exposing both carbon dioxide and water ice during the southern summer (Forget, 2007; Barlow, 2008). Also, during northern summer, water vapour releases into the atmosphere and due to the general circulation it is transported to the altitudes or

regions where it can condense and form water ice clouds or even deposit as surface frost in the equatorial regions (Nelli et al., 2009; Forget, 2007). Water vapour also condenses in the southern polar regions, where that carbon dioxide ice acts as a cold-trap for water ice that does not sublimate again during the southern summer (Forget, 2007). This change would have varied considerably due to changes of the Martian obliquity (the tilt of rotational axis) and eccentricity during the past several million years. Currently, it is uncertain if there is a balance between the northward and southward flow of water vapour. Water ice deposition mechanisms include both condensation and precipitation onto the surface and diffusion into the porous regolith (Schorghofer, 2007).

The Mars polar regions consist of horizontal, thick polar layered deposits (PLDs) composed of water ice, dust and silicone dioxide or silica (Tanaka and Scott, 1987). The northern and southern polar layered deposits underlay both the residual and seasonal ice caps (Barlow, 2008). North polar layered deposits (NPLDs) and south polar layered deposits (SPLDs) span approximately 1000 km in diameter and were found to be roughly 3.5 kilometres in thickness according to estimates using measurements from the Mars Orbiter Laser Altimeter (MOLA) on board Mars Global Surveyor (Plaut et al., 2007). The northern residual ice cap is composed of water ice and spans ~1000-1100 km in diameter coating the NPLDs. The north polar cap rises ~3 km above the surrounding topographically low northern plains and its centre is almost coincident with the rotational pole (Zuber et al., 1998). The ~1000-1100 km diameter cap covers much of the region poleward of 80°N (Clifford et al., 2000) and its volume is estimated between 1.1 and 2.3×10^6 km^3 (Zuber et

al., 1998; Smith et al., 2001). The southern residual cap is white, bright solid ice, very reflective and very cold (-130° C) and is composed of ~8-10 metres of permanent carbon dioxide ice overlaying water ice (Barlow, 2008; Byrne and Ingersoll, 2003; Smith et al., 2001) and spans ~ 400 km in diameter according to the Mars Advanced Radar for Subsurface and Ionosphere Sounding (MARSIS) data set (Giuranna et al., 2008). Since the southern ice cap has a much smaller diameter, the SPLDs are not completely covered such as they are in the north. The southern ice cap lies at an elevation 6 km higher than the northern cap and rises only ~2-3 km above the surrounding plains. The volume of the southern PLDs is ~ 1.6 million km^3 (Plaut et al., 2007) and it is offset from the rotational pole (Forget, 2007).

Both the north and south seasonal ice are composed of carbon dioxide. The thickness of carbon dioxide ice varies from several centimetres at the boundaries of the polar caps to 1-1.5 metres close to the poles (Smith et al., 2001). The north seasonal carbon dioxide ice cap has an almost symmetrical pattern around the pole whereas the seasonal south polar cap is not symmetric around the pole and is extended asymmetrically to 50°S along different longitudes during winter southern polar night. The southern seasonal cap measures about 4000 km across at its largest during southern winter, and the northern cap measures about 3000 km across at its largest, during the northern winter. The seasonal north polar cap is visible from space at Ls = 10° (early spring in the northern hemisphere) and extends southward to nearly 60°N (nearly its maximum winter extent) whereas the seasonal south polar cap is visible at Ls = 180° (fall in the northern

hemisphere) and extends northward to nearly 65°S (Barlow, 2008). Figure 1.4 and figure 1.5 show north and south polar residual caps respectively.

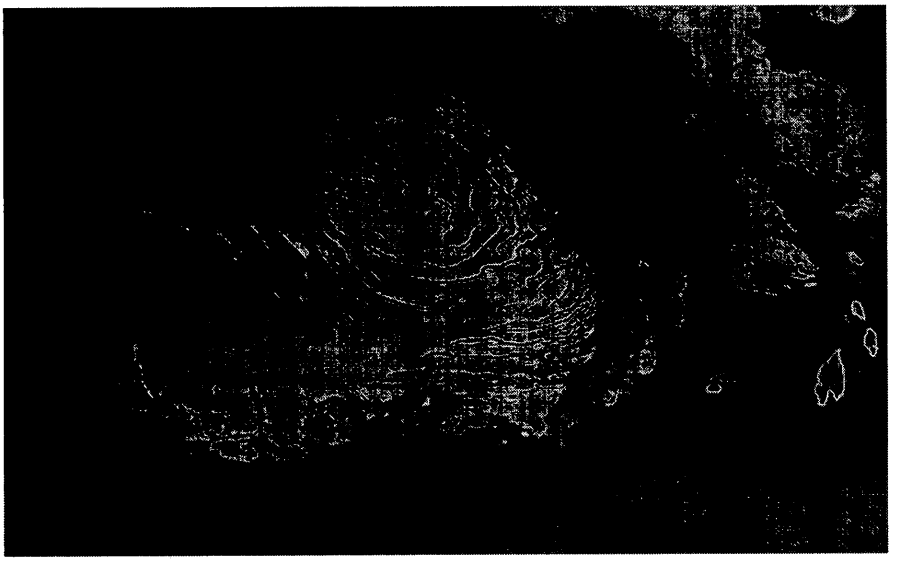

Figure 1.4: This picture shows northern ice cap during early summer (~Ls = 120°) and was taken from Mars Orbit Camera (MOC) on board Mars Global Surveyor. The ice cap diameter is about 1,100 km (Image courtesy of NASA/JPL/Malin Space Science Systems).

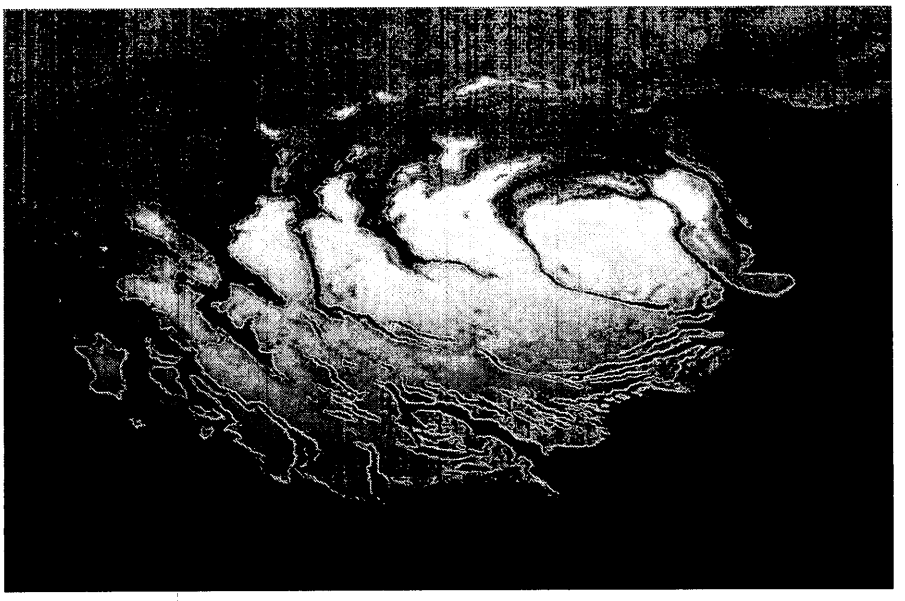

Figure 1.5: Image of south residual polar cap during late summer time (~ Ls = 341°) by Mars Orbit Camera (MOC) on board Mars Global Surveyor. South cap approximately has 400 km diameter (Image courtesy of NASA/JPL/Malin Space Science Systems).

1.4 Review of some observational data from MGS, MRO, Mars Express and Mars Odyssey

Martian weather was monitored with the wide angle of Mars Orbiter Camera (MOC) on board Mars Global Surveyor (MGS). Mars Daily Global Maps (MDGMs) from MGS show the formation of the visible frontal systems (curvilinear dust clouds for which topography is not apparently the cause) in the in the southern hemisphere, mostly between 210°-300°E and 0°-60°E during Ls = 140°–250° and Ls = 340°–60° (Wang et al., 2011). Figure 1.6 shows distribution of the Martian southern frontal events observed in Mars Daily Global Maps (MDGMs) from Ls = 150° in Mars Year 24 to Ls = 120° in Mars Year 28 (Figure from Wang et al., 2011).

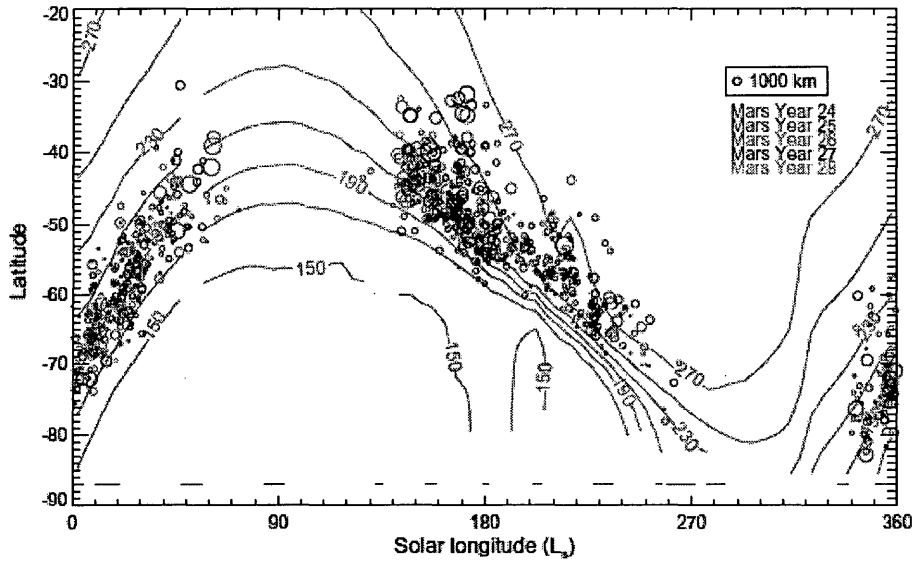

Figure 1.6: Distribution of the Martian southern frontal events (not topographically based) observed in Mars Daily Global Maps (MDGMs) from Ls = 150° in Mars Year 24 to Ls = 120° in Mars Year 28. The diameter of the circle shows the length of the frontal event, not the latitudinal extent. The gray contours represent the zonal mean surface temperatures at 2 pm in Mars Year 26 from MGS TES nadir data (Figure from Wang et al., 2011).

Mars Reconnaissance Orbiter (MRO) Mars Color Imaging (MARCI) also provided daily global imaging of Mars from September 2006. These images have given important information on CO_2 snow clouds (Renyu et al., 2012) and on CO_2 condensation above the north and south poles (Hayne et al., 2012). Measurements by the Mars Climate Sounder (MCS) instrument[4] on board MRO revealed[5] the characteristics of the particles and gases in the Martian atmosphere, such as their sizes and concentrations (Hayne et al.,

[4]The instrument has nine channels spanning the wavelength ~ 0.3-45 μm, with one visible and eight IR channels.

[5] There are significant particle characteristic model assumption employed for the derivation of the aerosol quantities from the MCS radiometer measurements.

2012). Figure 1.7 shows the distribution of small-grain CO_2 deposits formed by snowfall over the south polar cap of Mars during mid-southern winter (Ls = 112°).

The temperature and pressure profiles taken by the MRO for five Martian years have shown the conditions for the formation of CO_2 cloud particles. Also the non-ground MOLA data (lidar returns from CO_2 clouds) have indicated reflective particles in the CO_2 clouds. So by analyzing of the clouds opacity, the density of carbon dioxide in each cloud has been determined. Also by the estimation of the total CO_2 mass deposited over both poles and the number of snow particles in a given volume of snow cover, the size of the particles have been determined (Renyu et al., 2012). It is estimated that the average condensate particle radius in the northern hemisphere is 8-22μm and 4-13μm in the southern hemisphere (Renyu et al., 2012).

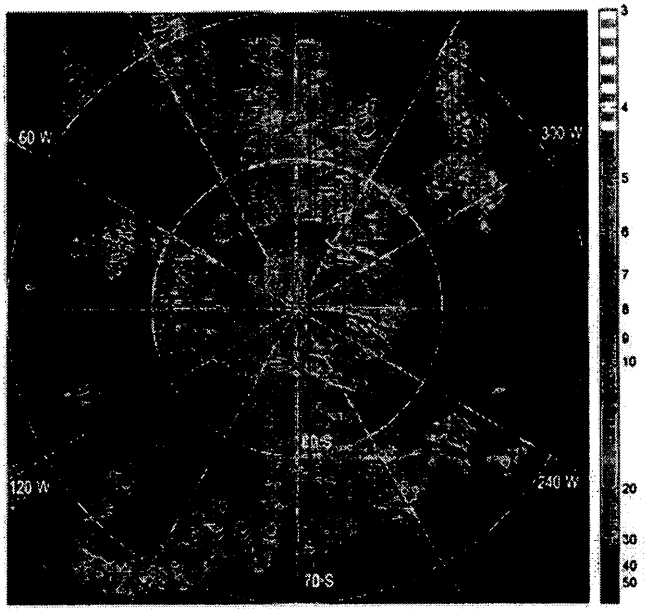

Figure 1.7: This map shows the distribution of small-grain CO_2 deposits formed by snowfall over the south polar cap of Mars. This image is based on IR measurements by the Mars Climate Sounder (MCS) instrument on the Mars Reconnaissance Orbiter (MRO). Color coding shows the mean diameter of carbon-dioxide grains detected by MRO's Mars Climate Sounder, from 4 mm (gray) to 50 mm (dark blue). Image released September 11, 2012. Credit: NASA/JPL-Caltech.

The OMEGA on board Mars Express provide important information about Martian surfaces such as south residual ice cap temperature during late summer (~Ls = 330°) and confirmed a temperature around 143 K (in section 5.7.2 the surface temperature from model prediction has been compared with OMEGA observation) on the southern permanent ice cap (Giuranna et al., 2008). The Mars Express Radio Science Experiment (MaRS) provides a study of the lower and middle Mars atmosphere between the surface and 40 km with a very high vertical resolution. MaRS experiments provide both temperature values and geopotential height information (Tellmann et al., 2013).

A comparison of the GM3 predicted air temperatures at 0.5 mb and MY26 TES observation is presented in Figure 1.8 (figure from Akingunola, 2008).

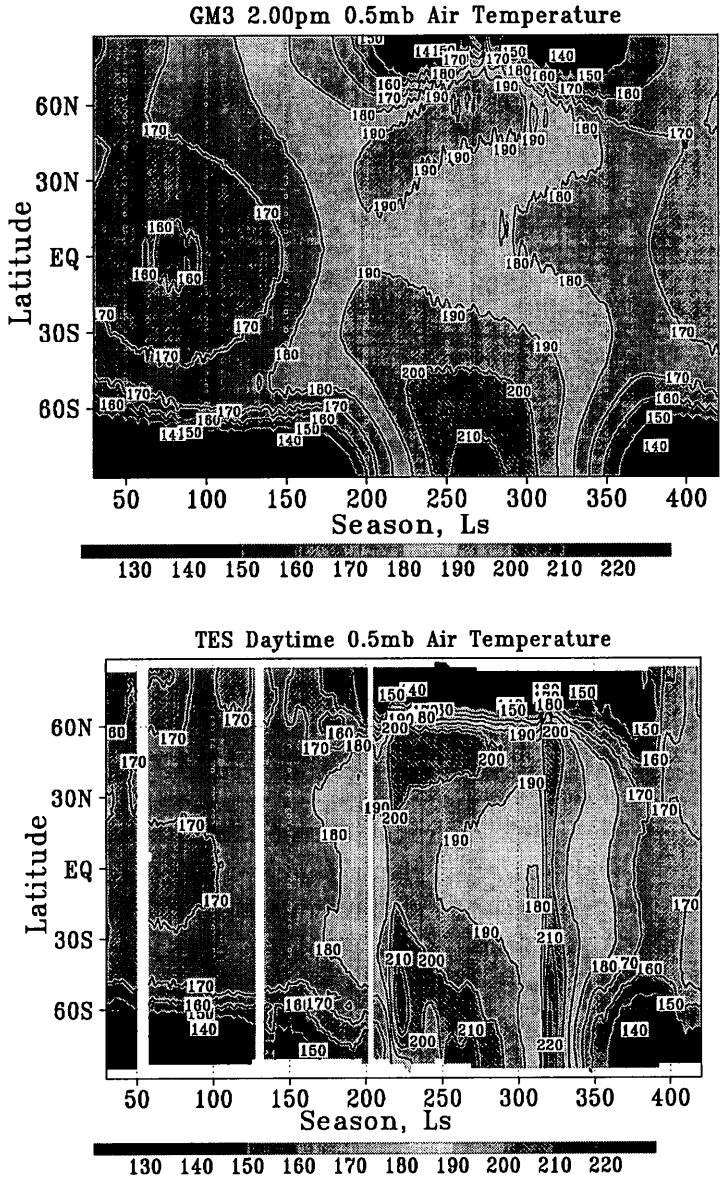

Figure 1.8: GM3 and TES zonally and temporally averaged air temperature at 50 Pa pressure level as a function of Ls. TES shows a rapid change in temperature around Ls = 330° caused by increased atmospheric dust loading from a dust event not represented in the model at that season (Akingunola, 2008).

There is a good agreement between model and TES measurements. However, there are two exceptions between the model prediction and TES observation. First the model has a low bias against TES measurements during early summer in the southern hemisphere for the equatorial region, and secondly TES shows a nearly global increase in temperature around Ls = 320°due to a global dust storm which was not predicted by the GM3 (Akingunola, 2008).

The gamma ray spectroscopy on board Mars Odyssey has provided information about atmospheric argon. This information determines how much argon remains in the atmosphere at high latitudes as carbon dioxide condenses during fall and winter seasons in each hemisphere. Also during late southern spring the area with the higher albedo has more concentration of argon than the lower albedo or cryptic region (see section 5.1). This could be associated with the faster subliming of the CO_2 in the cryptic region than in the non-cryptic regions (Sprague et al., 2012). Strong seasonal variation were observed at southern polar latitudes which show that the southern polar vortex should be strong and coherent in late autumn and early winter whereas the northern polar vortex is weaker (Sprague et al., 2012).

1.5 Research Objective

There have been many attempts to understand the nature of the Martian polar caps particularly the south polar CO_2 cap asymmetry. The caps have been observed for more than two centuries. There are, however, many questions which still need to be resolved.

There are different factors which can affect the south CO_2 ice cap characteristics including eccentricity, obliquity of the orbit, the seasonal CO_2 cycle and the local weather pattern. The local weather is very important because it can control the surface albedo by deposition of the CO_2 ice over the south polar cap and the build up of extensive snow or frost (Colaprete et al., 2005). Also results from the Mars Global Circulation Model (MGCM) from NASA Ames (Colaprete et al., 2005) show that Hellas and Argyre basins play a key role in controlling the weather patterns over the southern hemisphere.

In this research, the second version of the Global Mars Multiscale model was used to investigate the impacts of the local winter weather patterns on the asymmetrical nature of Martian South Polar CO_2 Ice Cap. In this work the meteorological fields such as temperature and wind structure were used and the analysis method provides more details and better understanding of the local weather pattern at southern mid and high latitudes which can explain CO_2 ice formation and sublimation in the form of frost or snow during each season.

In the next step, albedo and thermal inertia have been modified at the south polar areas in the GM3 physics code. These results show a better fit to CO_2 ice mass distribution near the south pole at cryptic and non-cryptic regions (see section 5.1).

The seasonal carbon dioxide ice in the polar regions is represented in the surface ice simulation by the second version of Global Mars Multiscale Model. However it does not produce a permanent south CO_2 ice cap, and so the physics code must be modified in order to capture the realistic physical and meteorological processes in the model aside

from ice formation. The permanent south CO_2 ice cap in the model can significantly improve south polar meteorology for example in predicted surface temperatures, surface pressures, horizontal and zonal winds over the south cap and also possible initiation of dust storms at south polar region during the southern summer period. In the final part to this thesis, the residual CO_2 ice cap is simulated in the physics code.

1.6 Thesis Outline

This first chapter is an introduction to the planet Mars, its atmospheric properties, polar caps and research objective. Also, the research goals have been discussed in this chapter briefly. The second chapter presents the second version of the Global Mars Multiscale Model (GM3-v2) description. The third chapter outlines the southern winter frontal weather patterns. The fourth chapter gives an insight into some dynamical effects of topography in the simulation with respect to southern weather activities. In the fifth chapter the importance of weather patterns and albedo in the asymmetrical structure of south polar cap are discussed. Also this chapter explains how albedo modification and artificial permanent CO_2 ice cap simulation is done in the model. The summary of important conclusions and the future outlook are presented in the last chapter.

Chapter 2

The Global Mars Multiscale Model

2 Description of the Global Mars Multiscale Model

The Global Mars Multiscale Model (GM3) is a three dimensional global climate model for the Martian atmosphere, which was developed at York University (Moudden et al., 2005; Moudden and McConnell, 2005; Akingunola, 2008). The model includes both physics and chemistry modules built onto the dynamical core.

2.1 Dynamical core

The dynamical core of GM3 is based on GEM (Global Environmental Multiscale Model) which was developed at the Meteorological Service of Canada for operational weather forecasting (Côté et al., 1998). GEM is a grid-point model with both global uniform and global variable resolutions with the capacity to resolve the small scale disturbances within

a high resolution sub-domain. The dynamical core of GEM can therefore provide the dual run-time capability of global scale with uniform resolution latitude/longitude grid system and also can be run in the mesoscale meteorology mode within a limited area over any portion of the globe using the global variable resolution configuration. In addition, the model can be run at very high resolution over a small domain in limited area mode (LAM). GM3 retains the GEM dynamical core except for fixed parameters such as gravity, composition, mean molecular weight, specific heat, radius and rotational rate which have to be redefined for Mars. The fundamental equations, conservation of mass, energy and momentum are solved in the dynamical core. The governing primitive equations can be solved in either hydrostatic or non-hydrostatic mode. It uses the hybrid vertical coordinate and the top boundary condition can be either rigid or elastic (Laprise and Girard, 1990). The second version of Global Mars Multiscale model is based on version 3.3.0 of the GEM dynamical core. The time-stepping is semi-implicit and the advection scheme is semi-Lagrangian.

2.2 Model Physics

The Martian physical processes are solved in the physics module. These processes include atmospheric heating, involving scattering and absorption of solar and thermal radiation, surface and sub-surface processes, orographic gravity wave drag, planetary boundary layer parameterizations, atmospheric water processes and condensation and sublimation of atmospheric constituents.

2.2.1 Heating

Dust scattering and absorption of solar and infrared radiation, CO_2 absorption in the 15 μm band and solar heating by CO_2, are calculated in this module (Akingunola, 2008). The two-stream formulation has also been extended to permit the treatment of radiation by water ice particles in the thermal (Akingunola, 2008). The non-LTE (Local Thermodynamic Equilibrium) formulation of Lopez et al. (1998) is used to calculate cooling at altitudes above ~70 km where departure from local thermodynamic equilibrium becomes important. A wide-band emittance is used in calculating the radiative fluxes due to the absorption of radiation in 15 μm band of CO_2 according to Liou, (1992), The generalized two-stream method with the quadrature approximation (Liou, 1992; Toon et al., 1989) is used to solve the set of two-stream (upwards and downward fluxes) equations (Akingunola, 2008). The fluxes are summed up, and the temperature tendency due to radiation is calculated.

2.2.2 Surface and Sub-Surface Layers

The soil scheme, surface fluxes and the calculation of the surface temperature are performed in the physics core.

The physics of the atmospheric surface layer (e.g. Figure: 2.1), which is a horizontal layer extending from the surface to a height of between 10-50 meters (depending on the surface heat flux strength), is presented in this module. The surface layer properties including the Monin-Obukhov length, the homogenous surface flux for

heat and momentum and surface friction velocity use the Monin-Obukhov similarity theory (Monion and Obukhov, 1954). This theory was confirmed for Mars's boundary layer by retrieving Mars Pathfinder temperatures in the lowest level of the Mars atmosphere (e.g. Maattanen and Savijarvi, 2004). This theory describes the relationships between temperature, near surface wind profile, and specific humidity and the surface fluxes including heat, momentum and water vapour in the surface layer. Assuming constant Monin-Obukhov length and friction velocity through the surface layer, the wind, temperature and specific humidity profile are calculated from Equations 2.16-2.21 in Akingunola (2008) and based on those according to Pielke (1990). Heat diffusion within the sub-soil and resulting soil temperatures are calculated too. This information is used to balance the surface energy budget and calculate the surface temperature (Akingunola, 2008). The diagnostic calculation of the near-surface temperature (at 1.5m) and wind variables (at 10m) using the surface flux properties is done in this module.

The amount of water adsorption and effect of the adsorption on water vapour diffusion in the regolith also is another important calculation in this module.

2.2.3 Planetary Boundary Layer

The planetary boundary layer (PBL) is the lowest level of the atmosphere and is strongly influenced by the underlying surface. In this layer, turbulence mixes heat, mass and momentum and induces some exchange between the ground and the atmosphere. The PBL on Mars has been known to be unstable and exhibits intense turbulent characteristics

during the day which can grow to more than 7km and conversely it becomes very stable during Martian night time (Smith et al., 2004). The PBL can be divided into a number of sub-regions, as indicated in Figure 2.1. The lowest layer in the PBL is the surface layer ($z/h_s < 1$), see Figure 2.1; here z is the vertical coordinate, and h_s is the surface layer height. Above this layer is the mixed layer, where strong mixing can take place to the top of the PBL. Jumping from mixed layer to the free atmosphere often forms an entrainment zone and air from free atmosphere is entrained into the underlying flow.

The planetary boundary layer calculations, based on the non-local scheme of Holstag and Boville (1993), are also performed in the physical core. In this division, the calculation of the diffusion coefficients and turbulent fluxes for heat and momentum are done. Calculations of the diffusion of heat and momentum (zonal and meridional winds) are performed by using a semi-implicit Crank-Nicholson scheme (Akingunola, 2008). The temperature and wind tendencies due to turbulence also are evaluated (Akingunola, 2008). The boundary layer height is a diagnostic quantity and is also calculated in this module.

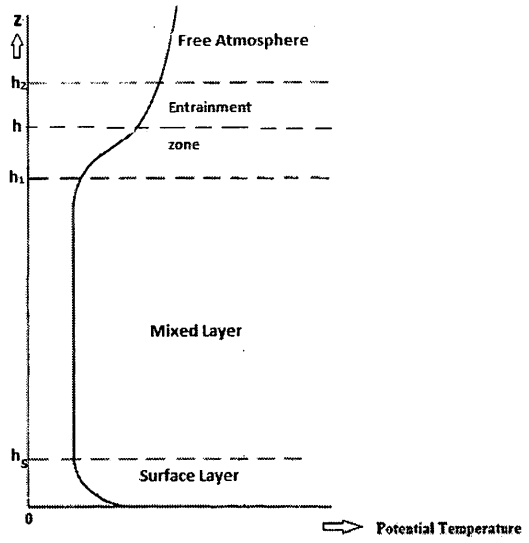

Figure 2.1: Schematic structure of the daytime convective planetary boundary layer.

2.2.4 Orographic Gravity Wave Drag

An orographic gravity wave parametrization, available in the Physics package of the terrestrial GEM model, and which follows the formulation of McFarlane (1987) and McLandress and McFarlane (1993) has been modified for Mars conditions and used in Global Mars Multiscale model (Akingunola, 2008). Orographic gravity wave drag is parametrized and applied after the surface processes are determined. This depends on the integration to calculate the gravity wave launching height, topography direction, slope and eccentricity (Akingunola, 2008).

2.2.5 Atmospheric Water Ice and Atmospheric Water Vapour

The major source of atmospheric water vapour appears to be at the Martian polar regions, while the regolith appears as both source and sink in the Martian low and mid-

latitude regions. The distribution of the atmospheric water vapour can be controlled by the thermodynamic equilibrium of water vapour and water ice, resolved transport, eddy transport (in PBL), gravitational sedimentation of water ice. Advection of both traces (water ice and water vapour) are done in atmospheric water ice and atmospheric water vapour module (Akingunola, 2008). The water ice opacity is also calculated in this section. The vertical diffusion of water vapour is carried out either in the physics code when the chemistry module is deactivated, or in the chemistry module when that is activated. The solution of the triadiagonal matrix equations is performed with the same scheme used for the turbulent diffusion in the planetary boundary layer scheme (Akingunola, 2008). For the results reported in this thesis, the chemistry module was deactivated and the model is run with the physics code.

2.2.6 CO_2 Condensation and Sublimation

In the physics module the effects of CO_2 condensation and sublimation in the atmosphere and on the surface are calculated (see later in chapter 5). Albedo and emissivity are very important in controlling the energy balance on the caps, so in this study, albedo and thermal inertia are modified based on cryptic and non cryptic region (see section 5.1) at the south polar cap. This is done within the model's dynamical core. It should be consider that the CO_2 condensation scheme in the model does not account for condensation nuclei.

2.3 Model Grid Resolution

The GM3 simulation presented here were run at resolution of 4°x4° and 5°x6°. Constant seasonal atmospheric dust optical depth values (Akingunola, 2008) were assumed for the runs (Figure 2.5). The model does not have a microphysical cloud scheme. In this thesis we run the model in 4°x4° resolution. The model has 101 vertical layers with the vertical resolution decreasing logarithmically in pressure to a top value of $7x10^{-6}$ Pa (~140km). Here, in the plotted figures the data were interpolated (bi-linearly by using the GrADS (http://www.iges.org/grads/) if needed.

2.4 Surface Albedo and Thermal inertia

The data input into the model includes the surface albedo as obtained from the Mars Global Surveyor (MGS) Thermal Emission Spectrometer (TES) visible near-IR data (Christensen et al., 2001) and the thermal inertia map derived from the MGS TES thermal bolometer data (Putzig and Mellon, 2007). The data map used in the model represents a mean state of albedo for all seasons of Mars. However, the albedo has to be modified in the polar regions to account for seasonal change, driven by the formation of surface ice (see section 5.7). This also important for more accurate prediction of the Martian water cycle. Figures 2.2a and 2.2b show surface albedo and thermal inertia maps at model resolution (Akingunola, 2008).

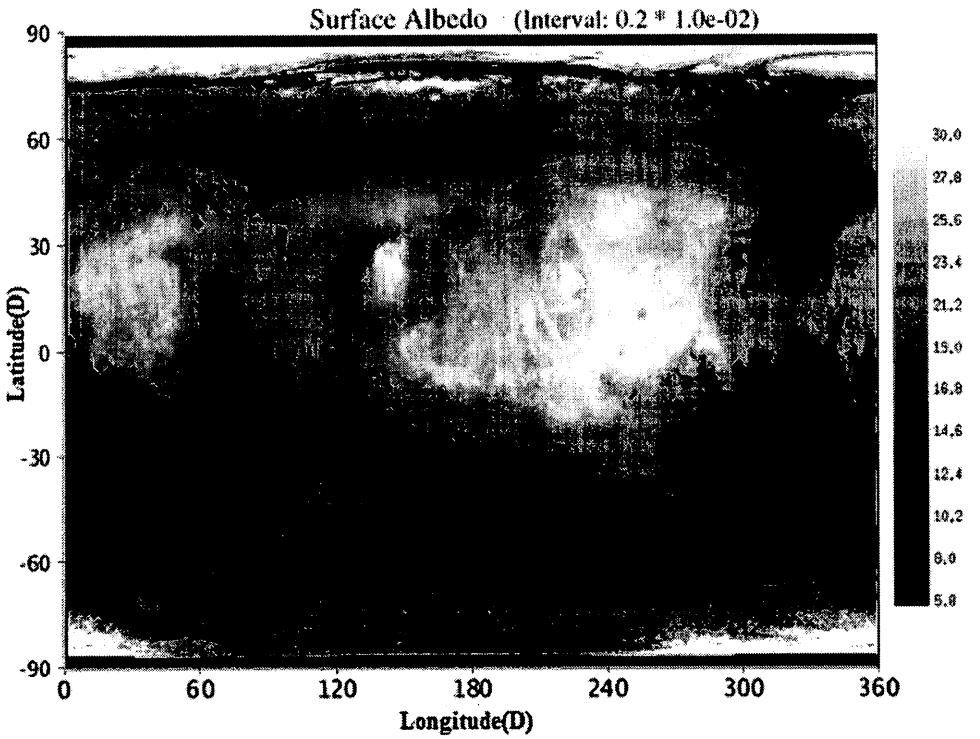

Figure 2.2a: The map of albedo of Mars (Christensen et al., 2001). Temporal variation in the surface albedo due to erosion and sedimentation of dust has not been considered in the model (Akingunola, 2008).

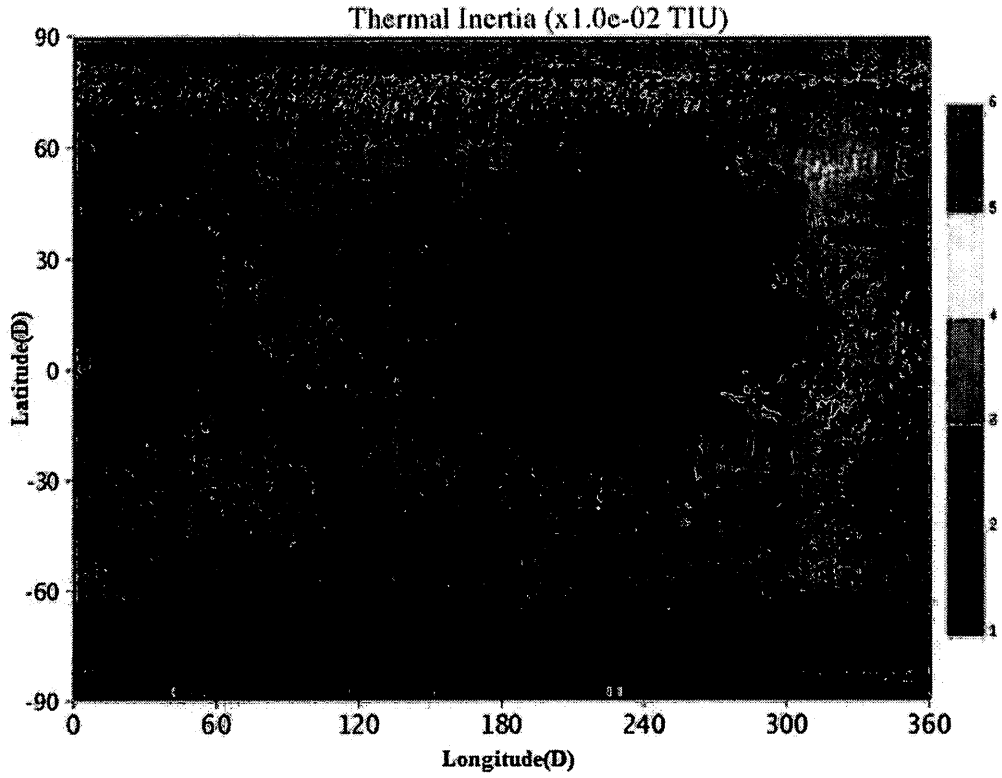

Figure 2.2b: The map of thermal inertia (from Akingunola, 2008), in thermal inertia unit (TIU) of $Jm^2K^{-1}s^{-1/2}$ (Putzig and Mellon, 2007).

2.5 Topography

The topographic data in the model is from the Mars Global Surveyor's MOLA (Mars Orbiter Laser Altimeter). The raw data are at 32 pixels per degree (ppd) resolution and are used directly to calculate the mean elevation and the unresolved orographic variance used in the gravity wave scheme (Akingunola, 2008). Figure 2.3 and Figure 2.4 show the topography of Mars obtained from MOLA observations (Smith et al., 1999) and the 'Airy-0' (within the larger crater Airy), which was chosen as the zero degrees longitude point respectively. This crater was chosen by Merton Davies as Mars's prime

meridian in 1969 based on Mariner 6 and 7 photographs. The Mars reference longitude has been updated the Airy trough time. The position of Airy has been better determined by Mars Global Surveyor (MGS) Mars Orbital Laser Altimeter (MOLA) observations with an accuracy order of 100 m in horizontal position (Figure 2.5).

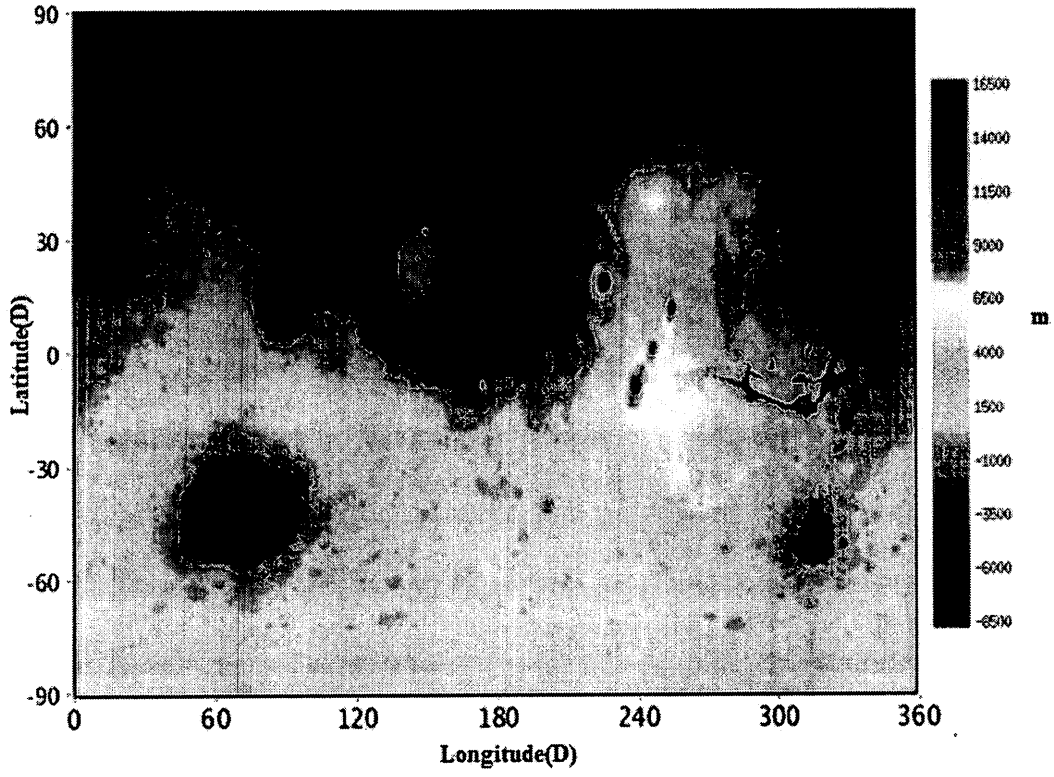

Figure 2.3: The topography of Mars obtained from MOLA observation (Smith et al., 1999). Dominant features include the low northern hemisphere, the Tharsis mountain ranges, and Hellas and Argyre basins in the southern hemisphere. The topography map has been produced from MOLA grided data from the Geosciences Node of the Planetary Data Service (Akingunola, 2008).

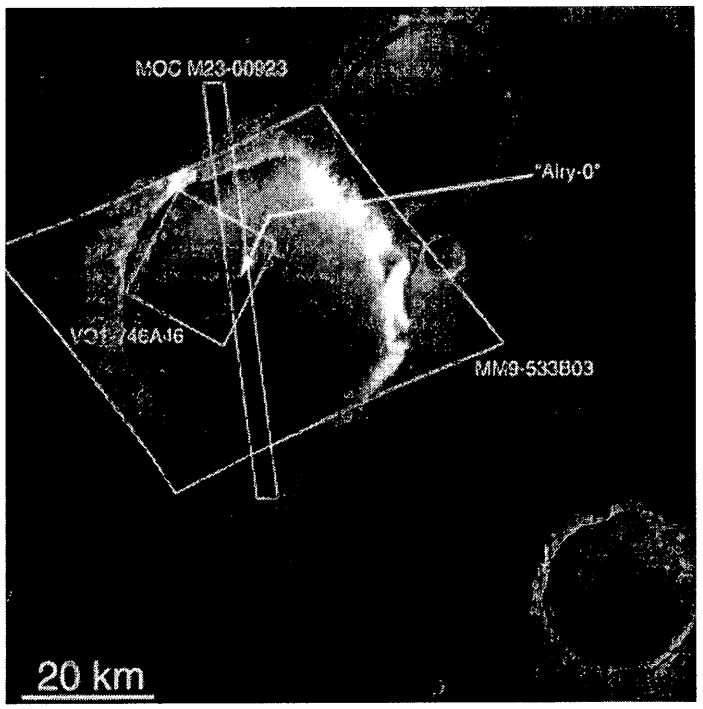

Figure 2.4: The 0.5-kilometre-wide crater, subsequently named 'Airy-0' (within the larger crater Airy), chosen as the zero degrees longitude point. Here the outlines of the Mariner 9, Viking and Mars Global Surveyor images are shown on a wide-angle context image taken by the US Mars Global Surveyor (MGS) Mars Orbiter Camera (MOC). Credits: NASA/JPL/MSSS.

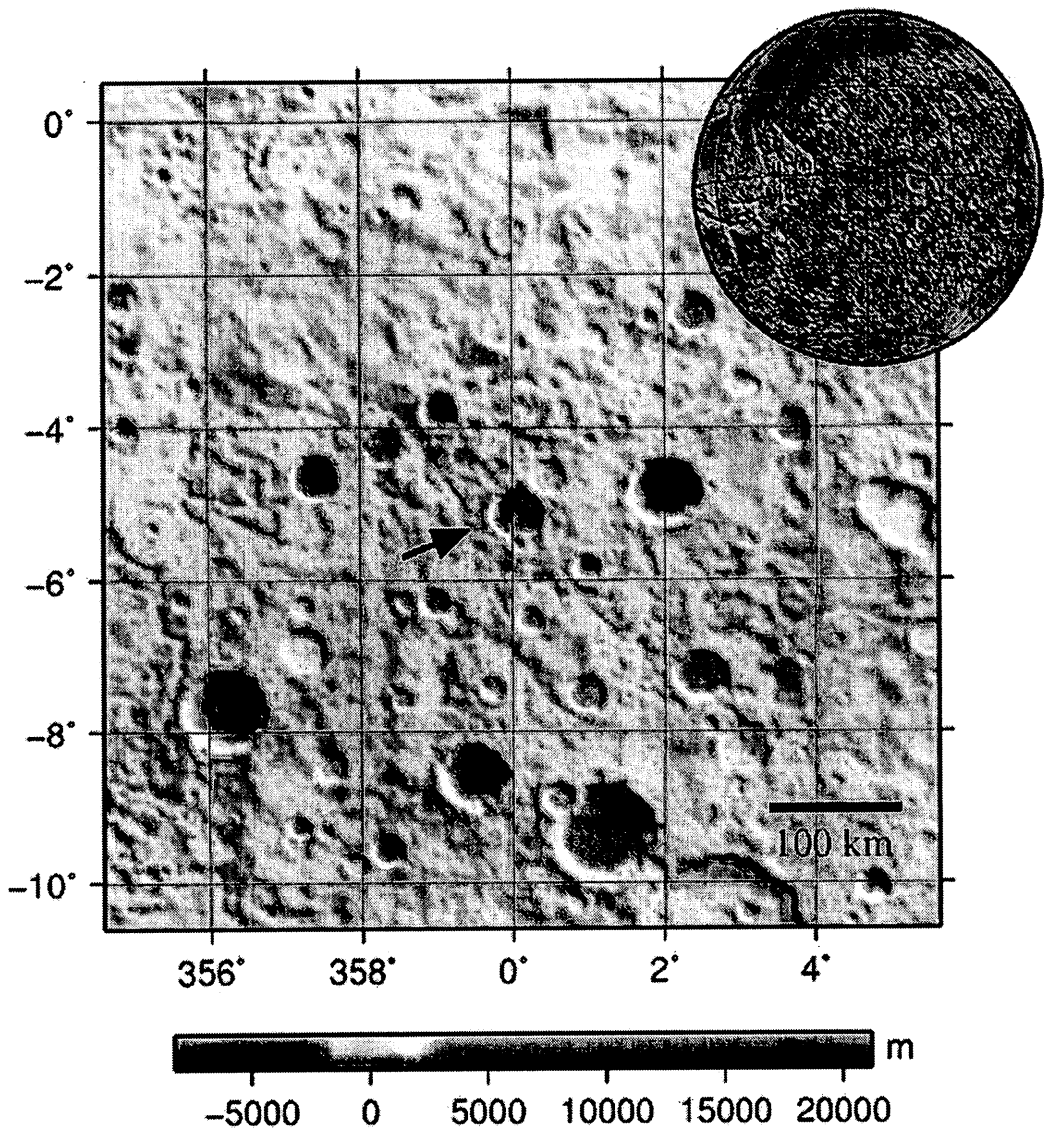

Figure 2.5: The arrow in this figure shows the Airy-0 observed by Mars Global Surveyor (MGS) Mars Orbital Laser Altimeter (MOLA). Credits: NASA/JPL.

2.6 Dust Optical Depth in GM3

Due to significant importance of the atmospheric dust loading on atmospheric

temperature and Martian weather in general (e.g. Smith et al, 2002) , an attempt has been considered in GM3 to allow for a global uniform and seasonally-varying of seasonal variation dust optical depth as can be seen in Figure 2.7(Akingunola, 2008).

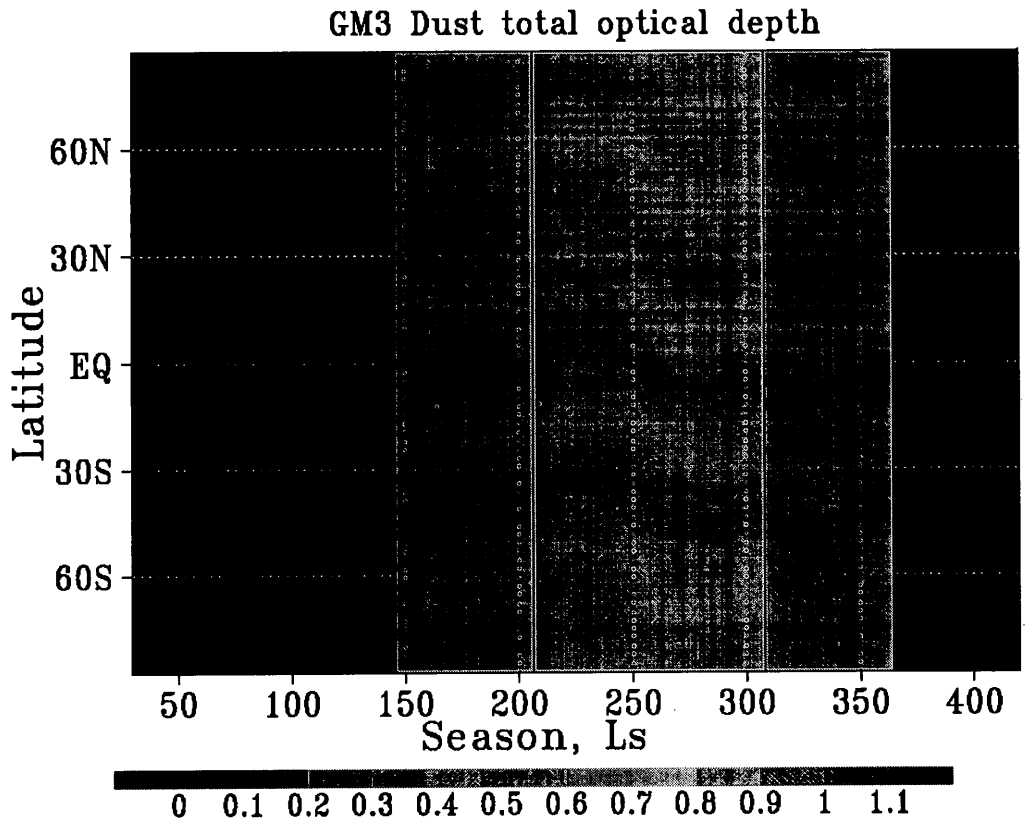

Figure 2.6: Seasonal distribution for the total dust optical depth assumed by the second version of the GM3 (Akingunola, 2008).

Chapter 3

Frontal Weather Patterns during Late Fall and Winter in the Martian South Hemisphere

3 Introduction

Weather is the state of the atmosphere at a given time in the particular place and there are three key factors to determine the weather; temperature, pressure and humidity. Mars, like Earth, has an atmosphere, so it has weather. However, there are similarities and differences between the Martian and Earth atmospheres, some of which were discussed in Chapter 1. In this chapter we see that weather fronts can form on Mars.

Frontogenesis is defined as the rate of change of the horizontal temperature gradient across a frontal boundary which separates air masses with different temperatures. A process is said to be frontogenetic if it increases the temperature gradient and

frontolytic when it weakens the front. Frontogenetic is associated with horizontal thermal advection because the air masses tend to converge towards the front. Horizontal thermal advection refers to a change in temperature caused by the movement of air by the wind. Thermal advection is a key factor in frontal activities. Mathematically, temperature advection equals

$$-U.\nabla T \tag{3.1}$$

where U is the horizontal wind vector and ∇T is the vector temperature gradient. When the wind blows from a warmer to a colder region (i.e. a negative temperature gradient), there is warm advection, which is positive because it causes local warming. This explains the negative sign (-) in the equation. There are three factors that can make the heat advection larger; the strength of the wind, a larger temperature gradient and a smaller angle between the wind direction and temperature gradient, i.e. to maximize heat advection, the wind should blow normal to the isotherms (Holton, 2004). So, weather fronts are boundaries between air masses of different temperatures. From one side of a front to the other, the properties of an air mass can change significantly (e.g., contrasts in temperature, wind direction, cloud cover, and on-going weather). There are four types of fronts; warm, cold, occluded and stationary (Ahrens, 2007). If the warmer and less dense (colder and denser) air is moving into an area previously occupied by cool air (warm), the front is termed a warm front (cold front). The slope (Z/X) of a typical warm front on Earth is very gentle (~1/150 to ~1/300) in contrast to that of a cold front (~1/50 to ~1/100). Also the mean low level wind speed in the vicinity of a cold front is much larger

than near a warm front (Ahrens, 2007). On Earth, a warm front can produce an extensive region of cloudiness and precipitation ahead of the boundary while, the cold front can result a less extensive region but with the more intense wind speed (Ahrens, 2007). The occluded front can form when, a cold front catches up with a warm front. Then the sky would be chaotic and precipitation is widespread. Fronts also may be stationary with no change. The combination of these fronts and the critical components can be seen in the extra-tropical cyclones (wave cyclones). Extra-tropical cyclones are the synoptic scale low pressure systems responsible for most precipitation at mid-latitudes (Ahrens, 2007). According to polar front theory, an extra-tropical cyclone develops by forming a wave on a frontal surface, separating a warm air mass from a cold air mass. The primary energy source of these systems is the conversion of potential energy to kinetic energy (Holton, 2004). Figure 3.1a and Figure 3.1b show the different frontal systems[6] and vertical structure of an extra-tropical cyclone respectively.

[6] Understanding of the evidence of these different types fronts mentioned here for Mars could be addressed in the future work.

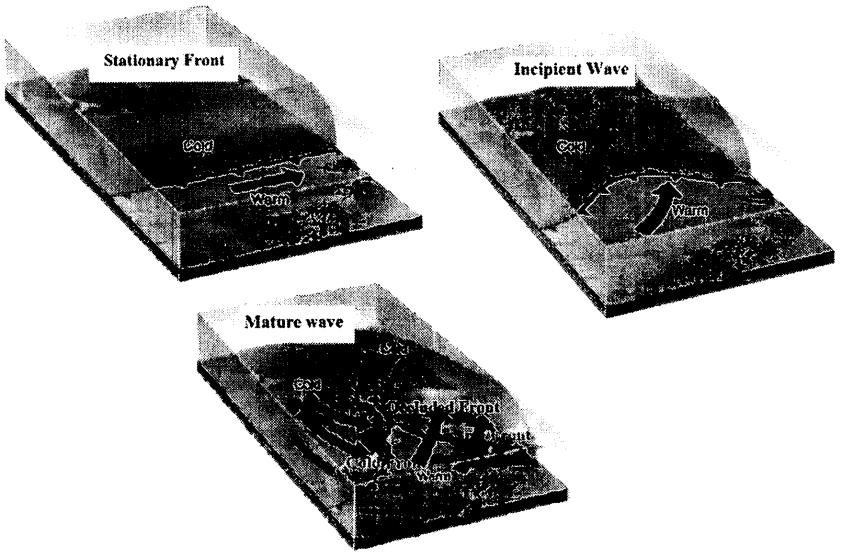

Figure 3.1a: Different frontal systems; stationary, cold, warm and occluded fronts (figure from Ahrens, 2007).

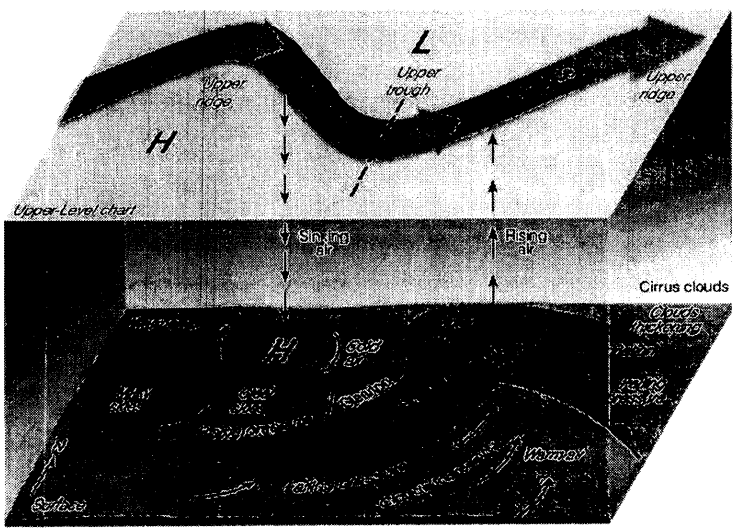

Figure 3.1b: The vertical structure of an extra-tropical cyclone (figure from Ahrens, 2007).

Frontal weather systems and extra-tropical cyclones can develop on Mars, as on Earth (Hollingsworth and Kahre, 2010). The first photograph from Mars that clearly showed the formation of extra tropical cyclones was obtained by the imager on the Viking Obiter 1. That storm system was observed at 81°N, 160°W, Ls = 105° (Figure 3.2). Another storm system was observed by Viking Orbiter 1 at Ls = 126° (northern summer) at about 66°N and 227°W (Figure 3.3). The observed brightness temperature shows that the atmosphere is too warm for the observed cloud to be composed of CO_2 ice particles (Hunt and James, 1979). Observation by the Mars Global Surveyor Mars Orbit Camera shows the southern hemisphere curvilinear clouds and dust storms, including frontal events and streaks around the south polar cap during Ls 140°–250° and Ls 340°–60° (Wang et al., 2011). Curvilinear dust features are not apparently related to topography. But when they appear in the polar hood, they are called streaks. The important factors for formation of curvilinear dust or clouds are convergence and shear in the circulation (Wang et al., 2011).

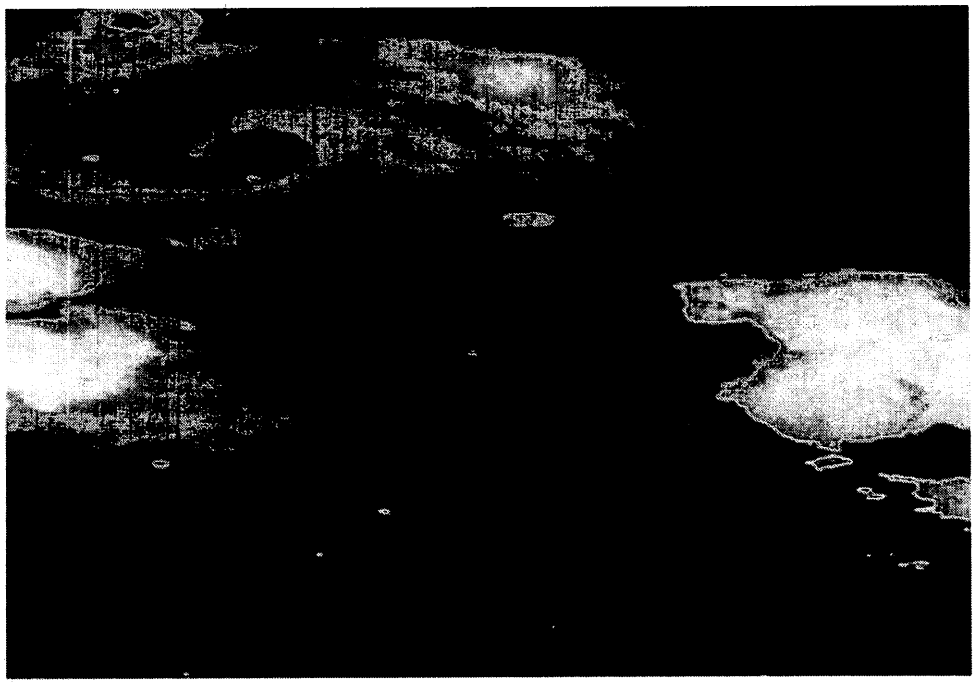

Figure 3.2: The first photograph from Mars which clearly showed the formation of an extra tropical cyclone was taken by Viking Orbiter 1. That spiral storm system (water ice clouds) was observed at Ls = 105° (northern summer) at 81°N, 160° W (Hunt and James, 1979).

Figure 3.3: This Martian storm system was observed by Viking Orbiter 1 at Ls 126° (northern summer) at 66°N, 227° W (Hunt and James, 1979)

.

Also, during autumn, periodic changes were observed in the pressure and wind vectors obtained by Viking Lander 2 which strongly suggested the passage of frontal systems to the north of the Lander site (Barnes, 1981; Barnes 1980; Hunt and James, 1979). During fall and winter (when the latitudinal temperature gradient is stronger than other seasons at these latitudes), as the fronts become stronger, the winds increase. At the Viking Lander 2 site, the wind at 1.5 m above the surface reached 23 m/sec.

Polar Regions have been recognized as areas where the dynamical process of baroclinic instability can cause the development of transient synoptic scale cyclogensis associated with frontal structures (Hollingsworth et al., 2008). These frontal systems have more

regular life cycles and are quasi-periodic compared those on Earth (Collins et al., 1997). Development of water ice clouds, which are observed at high and mid-latitudes, indicate a circulation pattern consistent with baroclinic waves which had been predicted by Mintz (1961). The wave disturbances occur on the polar front which separates the frigid and stable polar air mass from the relatively warmer mid-latitude air masses, especially during a transient seasonal period such as early spring or late autumn when there are strong temperature contrasts. These traveling disturbances also transport heat, and momentum and tracers such as water vapour, water ice and dust from low latitudes to the polar areas and high latitudes which influences atmospheric parameters such as temperature, wind, cloud, and dust amount (Hollingsworth et al., 2008; 1996). Measurements by the Mars Global Surveyor (MGS) thermal emission spectrometer (TES) instrument and Radio Science (RS) occultation measurements have shown the existence of large-scale traveling weather systems in the southern hemisphere. These traveling waves can be both barotropic and baroclinc (Banfield et al., 2003; Hinson et al., 2003). Theoretical and atmospheric modeling studies, and also the TES and RS observations, have indicated that the northern transient waves are much intense and deeper in comparison to those in the southern hemisphere (Hollingsworth et al., 2008). The temperature amplitudes of the southern traveling waves can be weaker than northern waves but with similar wave numbers 1-3 and the periods can change between two and four days at low levels and between six and twenty days or more at upper levels (Hollingsworth et al., 2008). In this chapter we analyze the weather structure in high and middle latitude regions in the

southern hemisphere during late autumn and winter, using the second generation of the Global Mars Multiscale Model in global uniform mode. This is very important because, as will be seen later in chapters 4 and 5, the regional weather patterns with respect to topography will be developed during southern fall and winter and change the south polar seasonal CO_2 ice cap structure.

3.1 GM3 Running Configuration

This section presents results from a GM3 run in the global-uniform configuration with a horizontal grid resolution of 4.0°x4.0°. The resolved spatial scale resolution at the equator is on the order of 240 km.

3.2 Model Results

The temporal average of surface (ground) temperature in the Ls range 80°-110° (northern late spring-early summer) centred around Ls 95° is shown in Figure 3.4 which indicates the large horizontal temperature gradients at the surface driven by the absorption of solar radiation with little IR heating from the atmosphere. Note the strong north-south surface temperature gradient at southern mid-latitudes.

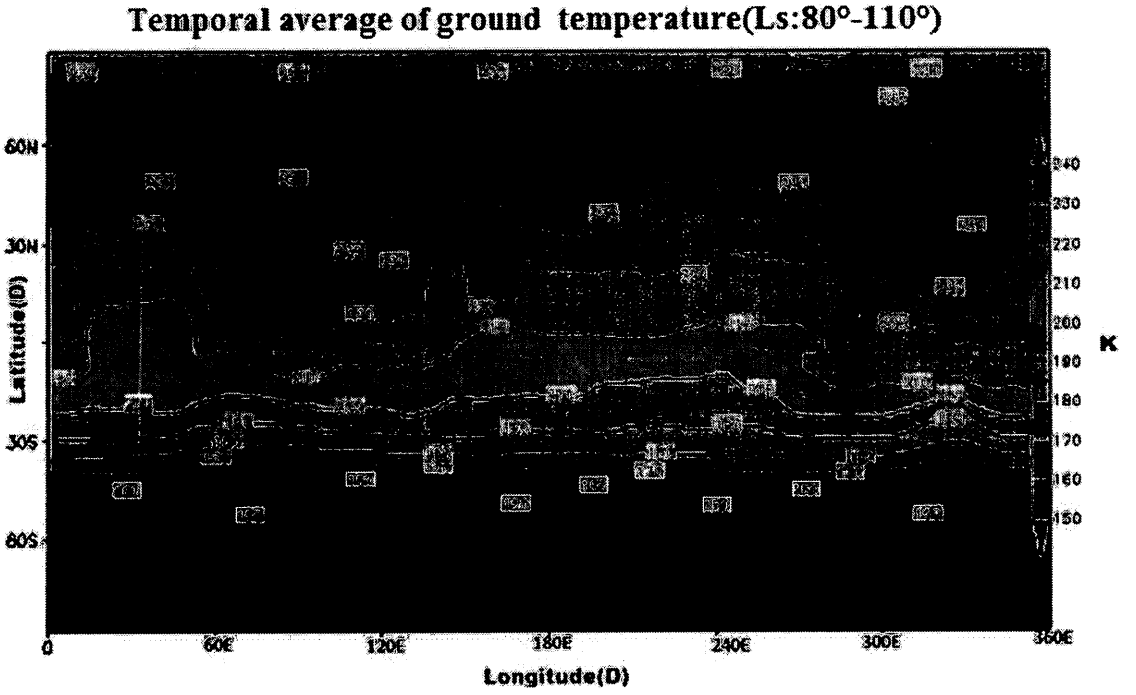

Figure 3.4: The temporal average of ground temperature in the Ls range 80°-110° (northern late spring-early summer) centred around Ls = 95°. The colour bar shows temperature in degrees Kelvin.

A zonal average of a latitude-altitude cross section of temperature in the Ls range for the same period time of Figure 3.4 is shown in Figure 3.5. At southern mid-latitudes horizontal temperature gradients are quite large compared to other latitudes. The vertical temperature structure at southern mid-latitudes shows an inversion and a very deep polar cold front which slopes slightly southward with latitude. A vertical cross-section for zonally-averaged zonal wind at the same period of time as Figure 3.4 is shown in Figure 3.6. The asymmetry can be seen in the zonal wind pattern where in the southern hemisphere the westerly polar jet is very strong with a peak speed in excess of 120 m/s

around 30 Pa in the jet core. There is also a zonal easterly jet at the equator with a peak of about 80 m/s around 5 Pa in the easterly jet core.

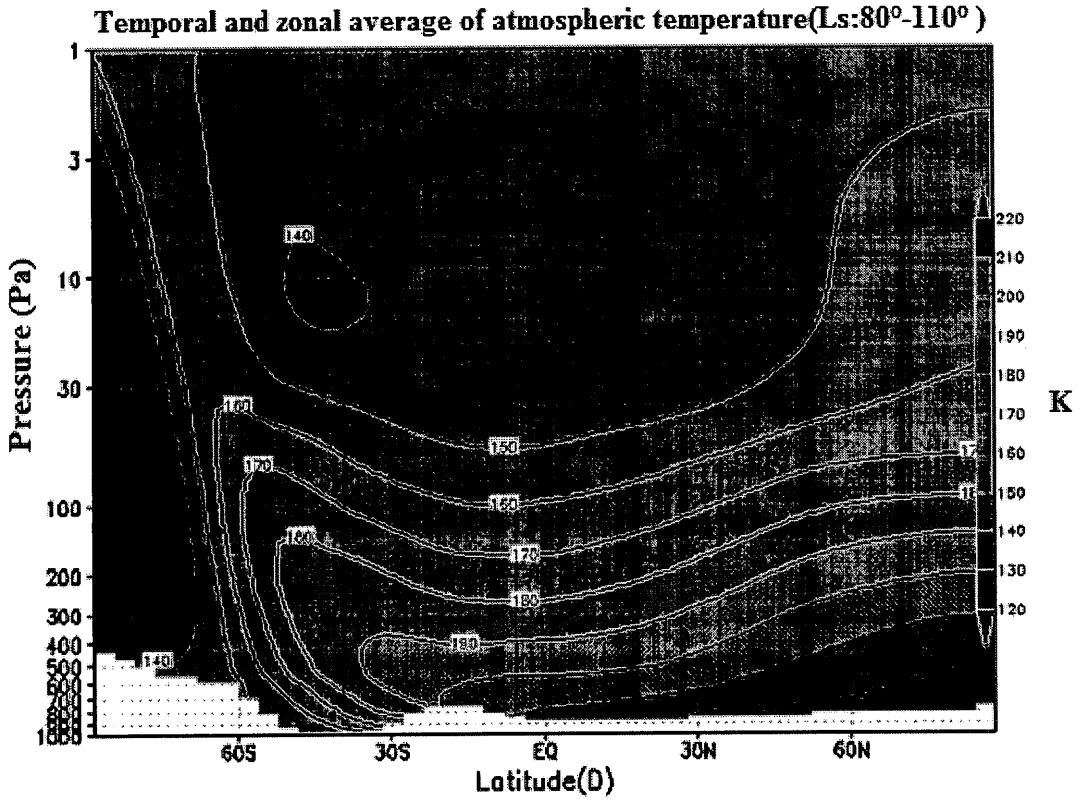

Figure 3.5: Temporally and zonally averaged temperature distribution in the Ls range 80°-110° (northern late spring-early summer) centred around Ls = 95°. The colour bar shows temperature in degrees Kelvin.

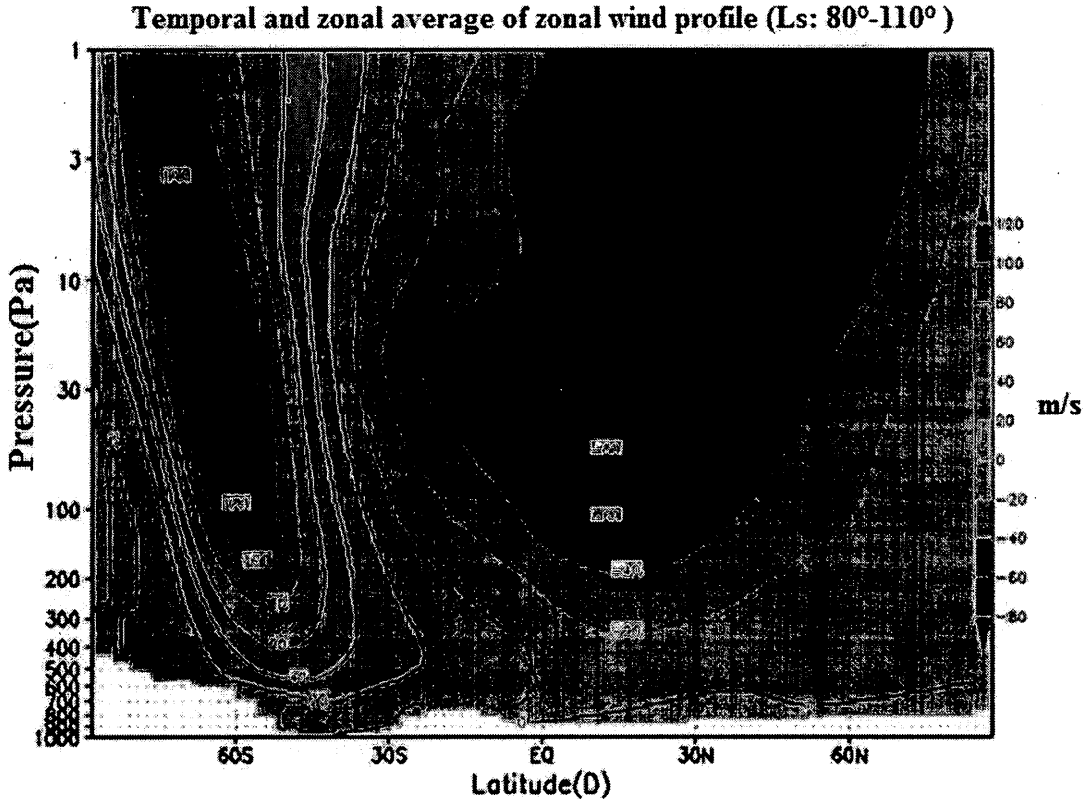

Figure 3.6: Temporally and zonally averaged zonal wind distribution in the Ls range 80°-110° (northern late spring-early summer) centred around Ls = 95°. Colour bar shows wind in m/sec. Eastward zonal winds prevail during summer at mid-latitudes on Earth, but mid-latitude zonal winds are generally westward (here in northern hemisphere) on Mars in summer (Read and Lewis, 2004; Leovy, 2001; Conrath et al., 2000).

3.2.1 Low Level Jet Stream

Figure 3.7 shows a horizontal cross-section map of the average zonal wind at 410 Pa for the same time period as Figure 3.4.

The westerly jet can be seen in the southern hemisphere. The maximum wind in the horizontal core of the south low level jet is ~ 60 m/s. The horizontal meandering pattern in the jet around 70°E and 330°E near the Hellas and Agyre basins indicates the

formation of stationary topographical Rossby waves (see chapter 4). So the winds can vary along Rossby waves and where the wind speeds up (slows down) divergence (convergence) occurs (see next section). These will then force rising or sinking motion at low levels. This shows the importance of the jet stream on weather system formation. These nearly wavy patterns can also develop in the polar front jet stream when significant temperature differences exist between warm tropical origin and polar air masses (see next section).

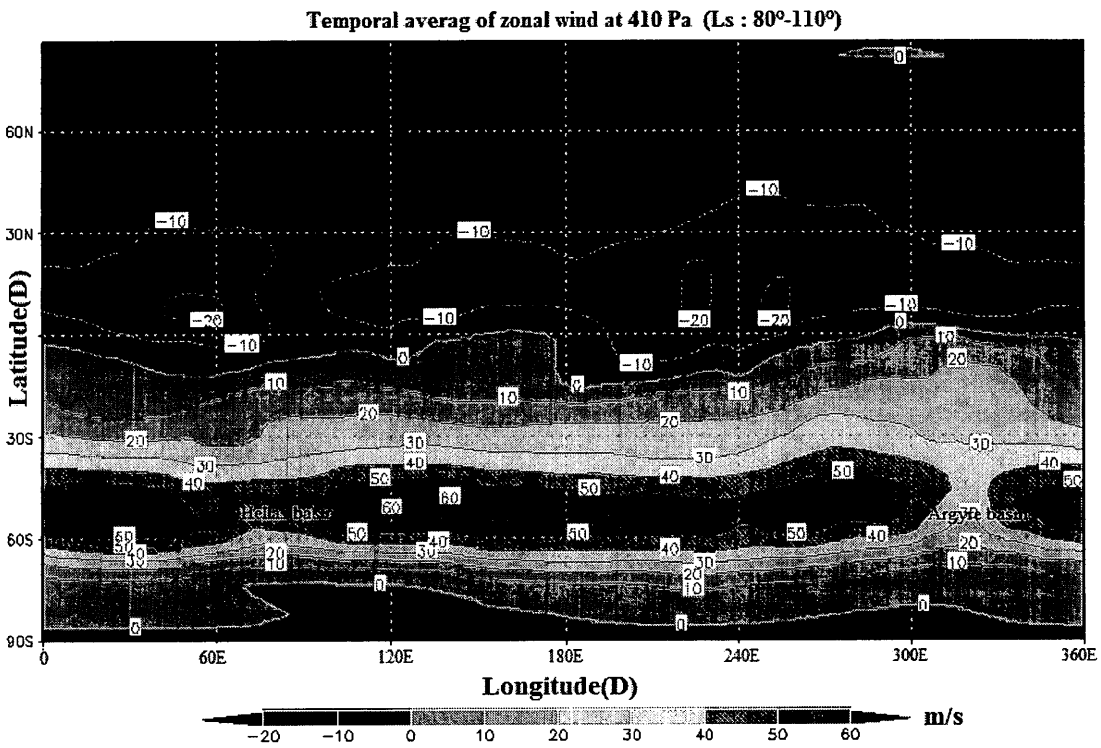

Figure 3.7: Temporally averaged zonal wind at 410 Pa in the Ls range of 80°-110° centred around Ls = 95°. The colour bar shows wind speed in m/s.

3.2.1.1 Low Level Temperature and Wind Streamline Patterns

A horizontal cross-section of temporal averaged temperature at 410 Pa for the same time period as Figures 3.4 and 3.7 is shown in Figure 3.8. With consideration of the wind flow patterns (Figure 3.9) and thermal pattern shown in Figure 3.8, it shows how distortion and moving of the colder temperature air mass flow to the south of the low level jet (polar air mass) towards the warmer southern mid-latitude air mass can cause a frontal system. Also we see the wavy pattern for isotherms around Hellas and Argyre basins.

According to polar front theory, in the mid-latitudes the polar front develops between colder air from the south high latitudes and warmer air from southern mid latitudes. The frontal boundary initially is stationary but with any small disturbance as a trigger (such as topography) leads to the development of an incipient wave (see Figure 3.1a) and a central low develops due to convergence and uplift, along with cyclonic circulation.

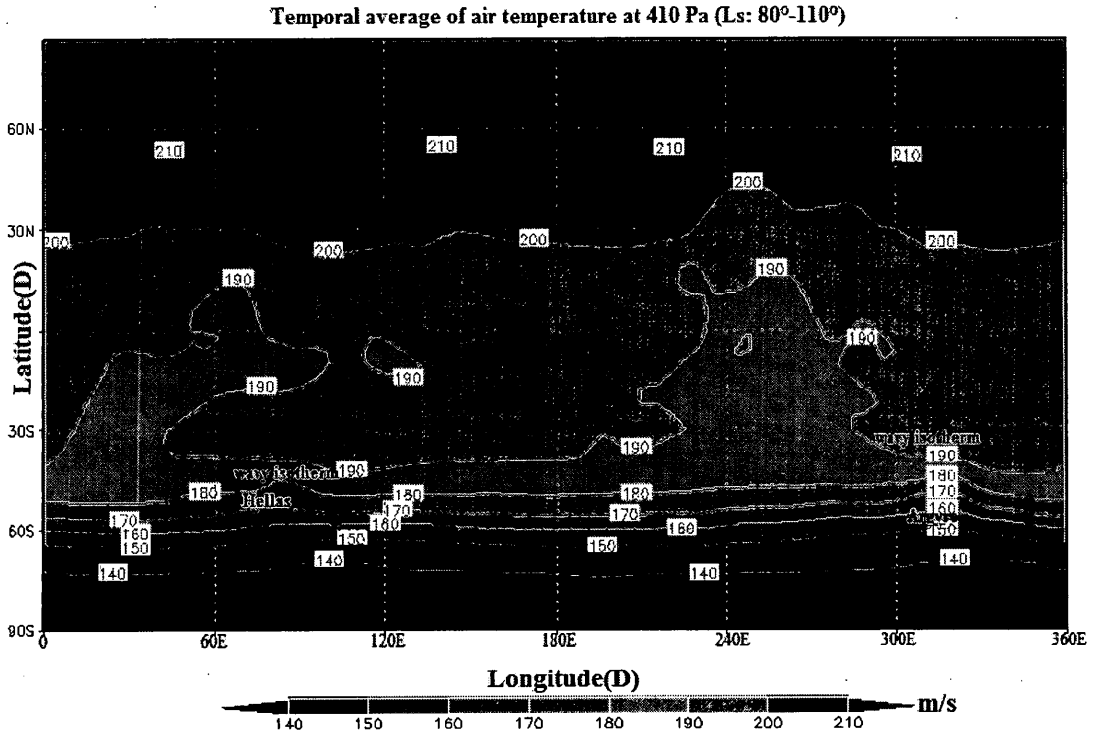

Figure 3.8: A horizontal cross section of the temporal average of air temperature at 410 Pa in the Ls range 80°-110° centred around Ls = 95°. The colour bar shows air temperature in degrees Kelvin.

This section examines the wind streamline patterns. Wind streamlines or "lines of flow" are a series of curves parallel to the wind throughout an instantaneous flow pattern. This pattern of motion can be interpreted immediately and indicates certain peculiarities which are not easily discernible from pressure patterns (Saucier, 2003). Thus, streamlines and sometimes isotachs (contours of equal wind speed) can be a useful method to illustrate the wind field patterns. Immediately, features such as lines of convergence in low level flow, forcing upward motion (so that surface air is lifted within the atmosphere) or divergence, reflecting sinking motion become apparent. For example, high values of

convergence may often denote an area with deep convection. Small arrows denote actual horizontal wind directions. The singular streamline is a line of divergence or a line of convergence. The simplest singular point (convergence or divergence) is the centre of a cyclonic or anti-cyclonic circulation, where streamlines are closed. It is good to remember that a convergence line (or zone) is not necessarily a line of maximum velocity convergence and conversely, similarly for divergence (Saucier, 2003).

Figure 3.9 shows a wind streamline analysis at 410 Pa (nearly low level at high latitudes) at Ls = 90° at 00 local time at zero longitude (the local time for all instantaneous maps shown in this research). This figure shows the presence of two cyclonic cells at 90°E and 320°E. It will be shown in chapter 5 that these two different local weather patterns impact the formation of the Martian south polar cap and its asymmetrical nature. This figure shows the formation of anti-cyclonic ridges to the north west (north west and west) and cyclonic troughs to the south of the Hellas and Argyre basins. Also formation of nearly flat λ shape thermal patterns (wavy isotherms) around 30°S, 70°E and 30°S, 320°E (Figure 3.8) shows a classical signature for mid-latitude frontal systems. The thermal field and streamline structure together (Figure 3.8 and 3.9) in both mentioned areas show the mixing of cold air coming from southern polar regions with the warm air coming from subtropical areas, can cause the formation of frontal systems[7] around Hellas and Argyre basins. In the next chapter it will be shown that the

[7] Actually a time sequence of maps is needed to illustrate if the frontal system is translating eastward and developing and decaying as is expected for a baroclinic wave system. This can be conducted in future work.

existence of the Hellas and Argyre basins can change the shape of streamlines and thermal patterns and affect the local weather around the areas discussed.

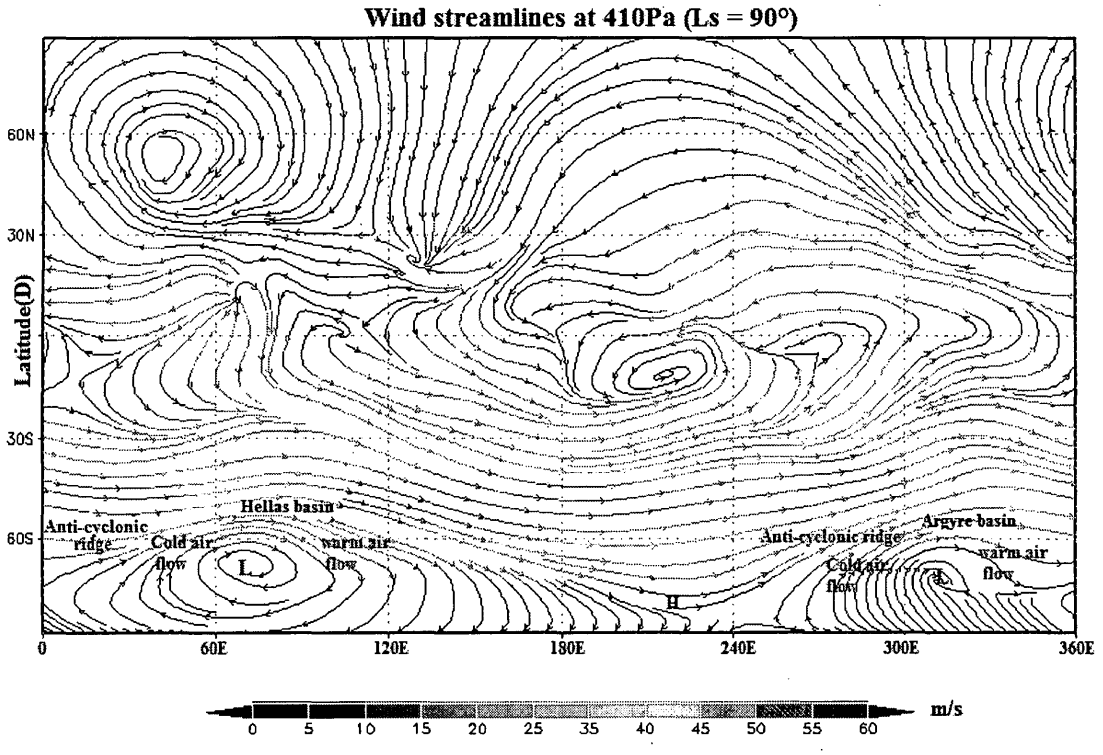

Figure 3.9: Formation of two cyclonic troughs at 410 Pa below the south low-level jet (Ls = 90°). The colour bar shows wind speed in m/s. As the figure shows the typical winter zonal winds in Martian mid-latitudes are strong westerlies.

3.2.2 Upper Level Jet Stream

Figure 3.10 shows a horizontal cross-section of zonal wind at 30Pa for the same period of time as Figure 3.4. The strong westerly jet in the southern hemisphere can be seen with a maximum intensity in the core of ~ 120 m/s.

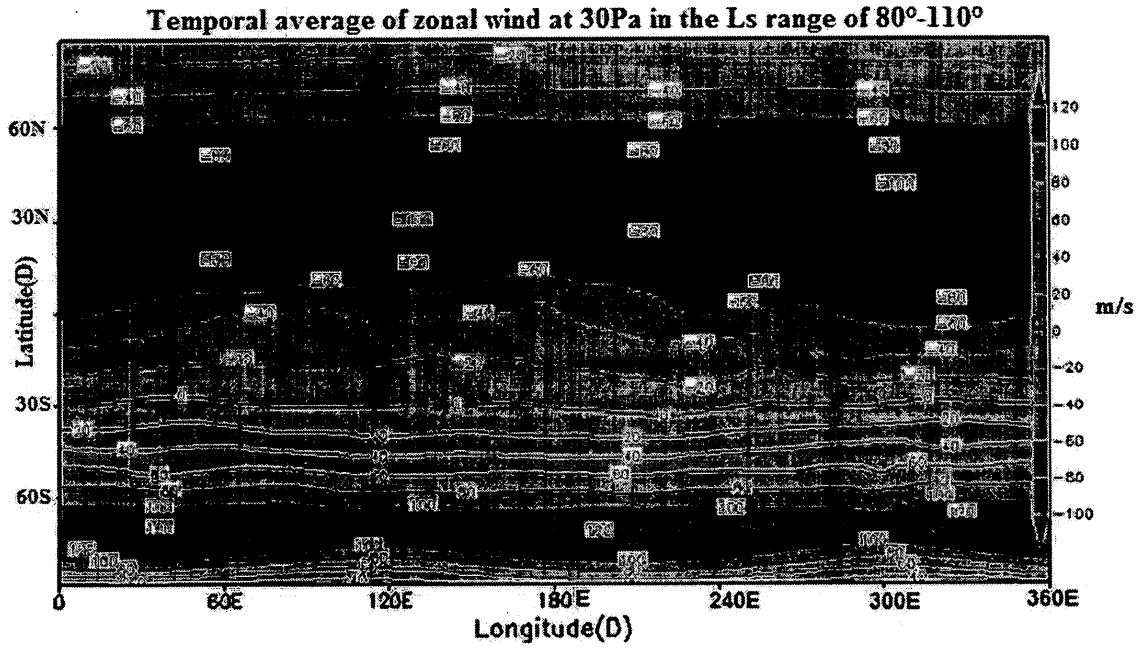

Figure 3.10: Temporal average of zonal wind at 30 Pa in the Ls range of 80°-110° centred around Ls = 95°. The colour bar shows wind speed in m/s.

Figure 3.11 shows wind streamline analysis at 30 Pa at Ls = 95°. This figure shows two elongated areas of cyclonic circulation (clockwise in southern hemisphere) below the southern high level westerly zonal jet. Between these two cyclonic circulations (L) the pattern is anti-cyclonic (H).

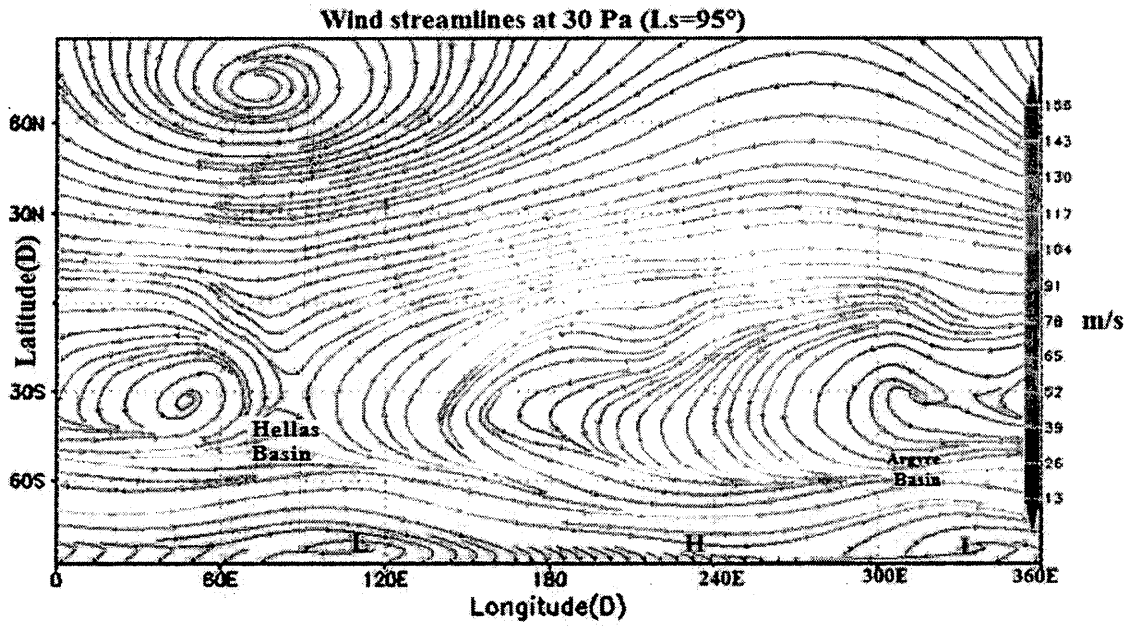

Figure 3.11: Formation of an elongated area of cyclonic circulation at 30 Pa below the south, high level jet. The colour bar shows wind speed in m/s.

3.3 Conclusions

The Global Mars Multiscale Model (GM3-v2) is used to simulate weather patterns in the Martian southern hemisphere for late local autumn and early winter time. The simulation reveals significant frontal activities during this period. It also indicates the formation a strong south polar front and its associated south polar jet stream. The general pattern shows that frontal systems at mid-latitudes can be formed because of the strong horizontal thermal gradients between the two different air masses together with cold northward winds from the polar regions and warm southward air coming from lower latitudes of the Martian southern hemisphere (Hollingsworth et al.,1996).

These form classical frontal systems very similar to those on Earth but at much lower surface pressures. A wind streamline analysis in the present study shows the formation of anti-cyclonic ridges to the north west (north west and west) and cyclonic troughs to the south of Hellas and Argyre basins. It will be shown that these two local weather patterns have an impact in the formation of an asymmetrical pattern of the Martian south seasonal CO_2 ice cap (chapter 5).

Chapter 4

Analysis of the effect of Topography on the Martian Weather Systems

4 Introduction

Mars, like the Earth, is a rapidly rotating solid planet with a shallow atmosphere. There are many similarities in the atmospheric dynamics phenomena between Mars and Earth. Also as we have noted earlier, Mars has large scale topographical structures such as deep valleys and high mountains which play an important role in the Martian weather. Results from the NASA Ames Mars General Circulation Model (Colaprete et al., 2005) show that the topography of Hellas and Argyre basins modulates the south polar atmospheric circulation. The results of numerical simulations of global atmospheric circulation patterns on Mars using the second version of Mars Multiscale Model are presented. The effect of the topographical features, Hellas basin centred at 42.7°S 70°E

and Argyre basin centred at 49.7°S 316°E (Figure 1.1) are the particular focus of this chapter. These two features play an important role in weather during the southern winter at southern high- and mid-latitudes.

4.1 GM3 Running Configuration

In this study the MOLA topography in GM3-v2 was switched off and the model was run with flat topography in order to compare the results with those for the MOLA topography. Topography can enhance horizontal temperature gradients which affect the development or intensification of the frontal systems (Hellas and Argyre basins in this case study). In this section results from a GM3-v2 run in a global-uniform configuration with a horizontal grid resolution of 4.0°x4.0° are presented. Also the albedo and thermal inertial fields were retained from standard GM3.

4.2 Temperature and Wind Streamline Patterns

Figures 4.1 and 4.2 show the surface temperature distribution, averaged over the Ls range 80°-110° (northern late spring-early summer) centred around Ls = 95° in the realistic and flat topography model simulations respectively. Generally the low-level temperature field in the flat topography is smoother than in the realistic topography case in the southern mid-latitudes. In the realistic topography simulation around the northern parts of the Hellas (42.25°S,70°E) and Argyre (49.7°S, 316°E) basins the temperature contrast with a nearly λ-shape pattern. This pattern cannot be seen in the flat topography

simulation. As Figure 4.2 shows albedo and thermal inertial are important responsible fields for longitude ground temperature structure at equatorial and northern middle latitudes in the flat topography simulation (Saito, 2006). Figures 4.3 and 4.4 are the same period but at 410 Pa. In the flat topography simulation the temperature field around Hellas and Argyre basins is completely zonal. Figures 4.5 and 4.6 show the geopotential height[8] and wind streamlines at 410 Pa for the realistic and flat topography simulation at Ls = 90°. As can be seen in the realistic topography simulation (Figure 4.5) cellular patterns have been formed in the southern hemisphere which are not seen when the topography is removed (Figure 4.6). The formation of these cellular patterns is the result of topographic stationary Rossby wave formation (Holton, 2004). Topographic Rossby waves are planetary waves which are created due to conservation of potential vorticity. The waves are generated when large scale topographical features (here such as Hellas and Argyre basins) lie across the zonal flow (southern night polar jet).

Figures 4.7 and 4.8 show the wind streamlines at 298 Pa for the realistic and flat topography simulation at Ls = 90°. Also we can see in the realistic topography simulation (Figure 4.7) that cellular patterns have been formed in the southern hemisphere which cannot form when the topography is removed in the model simulation (Figure 4.8). Also the wind streamline analysis at the time of Figure 4.5 for different heights below (200 Pa) shows the same result (Figures have not shown here).

[8] Since the planetary Rossby number on Mars is larger than Earth (0.2 rather than 0.05), ageostrophic motions are expected on Mars (Leovy 2001).

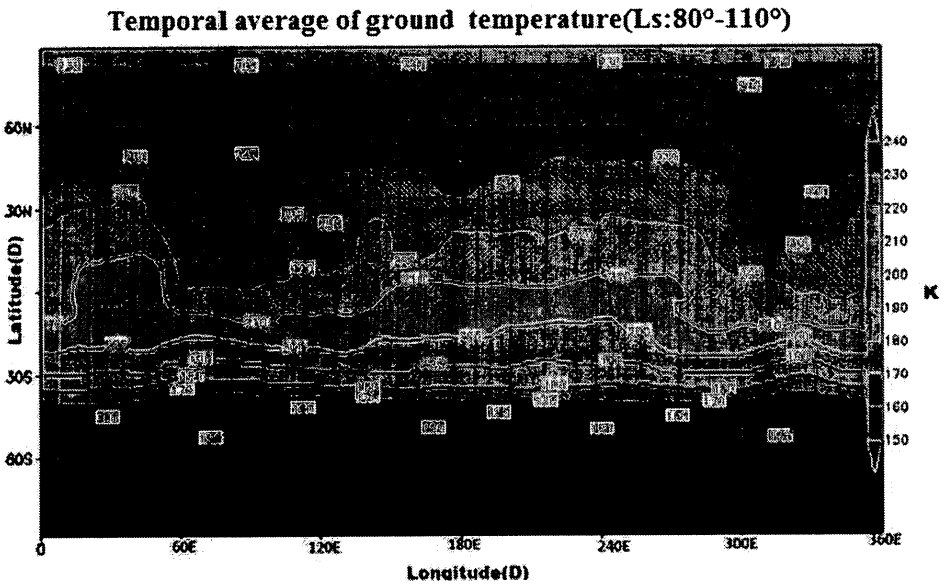

Figure 4.1: Temporal average of ground temperature in the Ls range 80°-110° (northern late spring-early summer) centred around Ls = 95° in the realistic topography simulation. The colour bar shows temperature in degrees Kelvin.

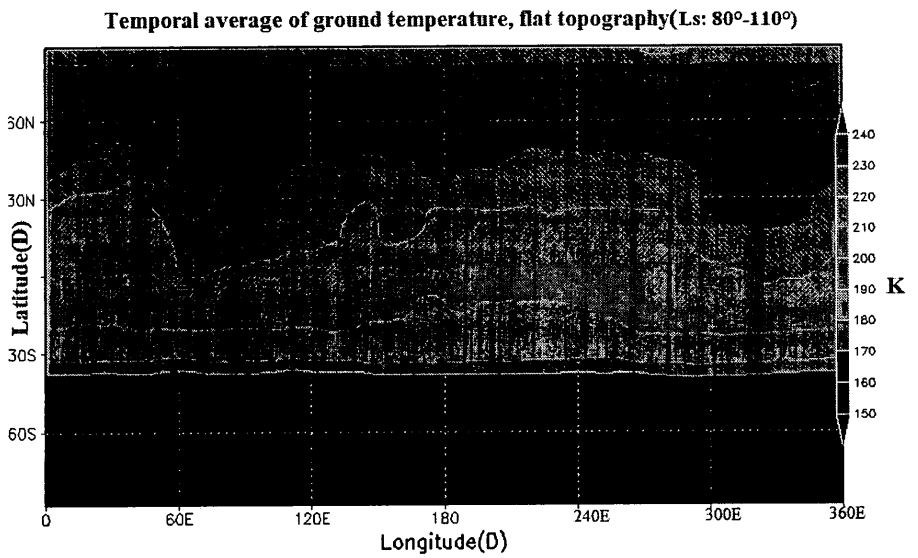

Figure 4.2: Temporal average of ground temperature in the Ls range 80°-110° (northern late spring-early summer) centred around Ls = 95° in the flat topography simulation. The colour bar shows temperature in degrees Kelvin.

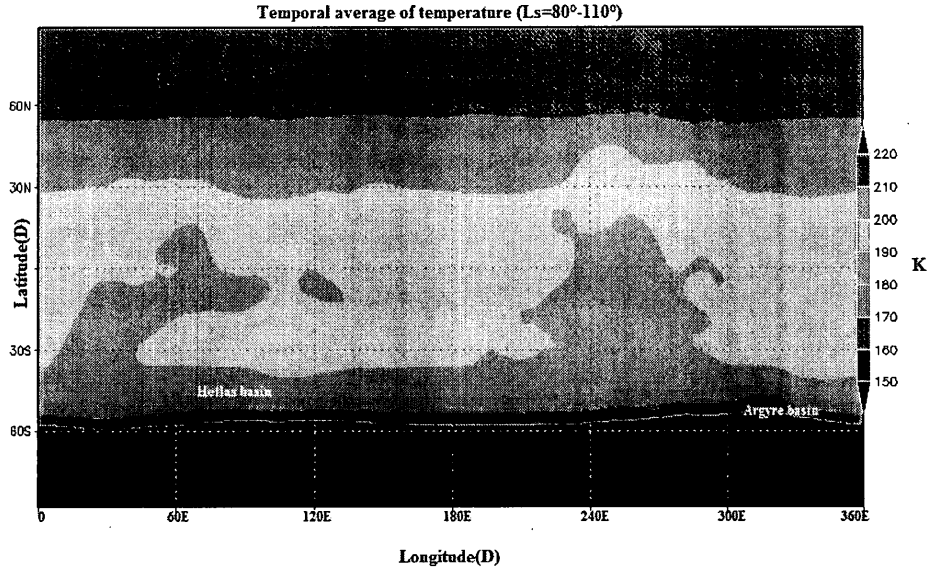

Figure 4.3: Temporal average of air temperature (Kelvin) at 410 Pa centred on Ls = 95° in the realistic topography simulation (Ls = 80°-110°).

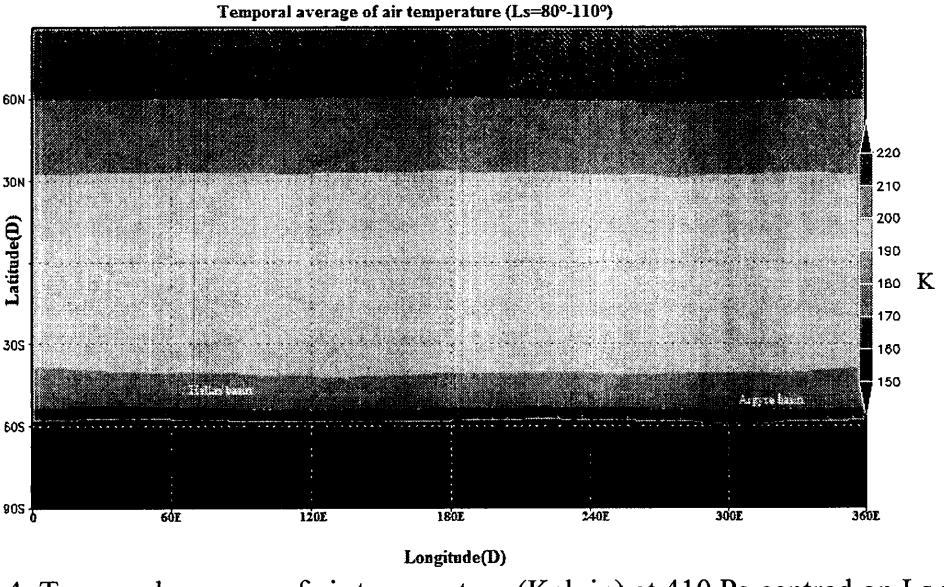

Figure 4.4: Temporal average of air temperature (Kelvin) at 410 Pa centred on Ls = 95° in the flat topography simulation (Ls = 80°-110°).

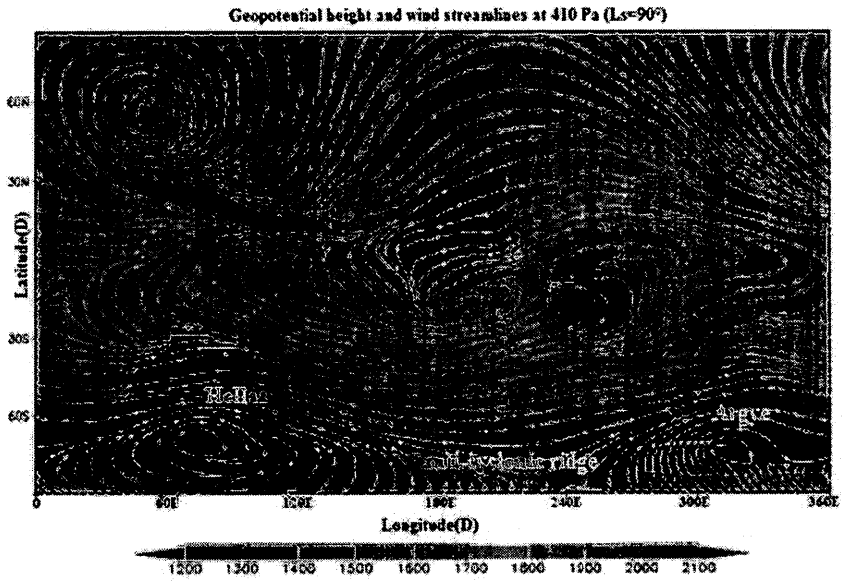

Figure 4.5: Instantaneous geopotential height and wind streamlines in the realistic topography model simulation at 410 Pa (Ls = 90°). The colour bar shows geopotential height. Since the planetary Rossby number on Mars is larger than Earth (0.2 for Mars rather than 0.05 for Earth, Leovy 2001) the ageostrophic motions are more expected on Mars.

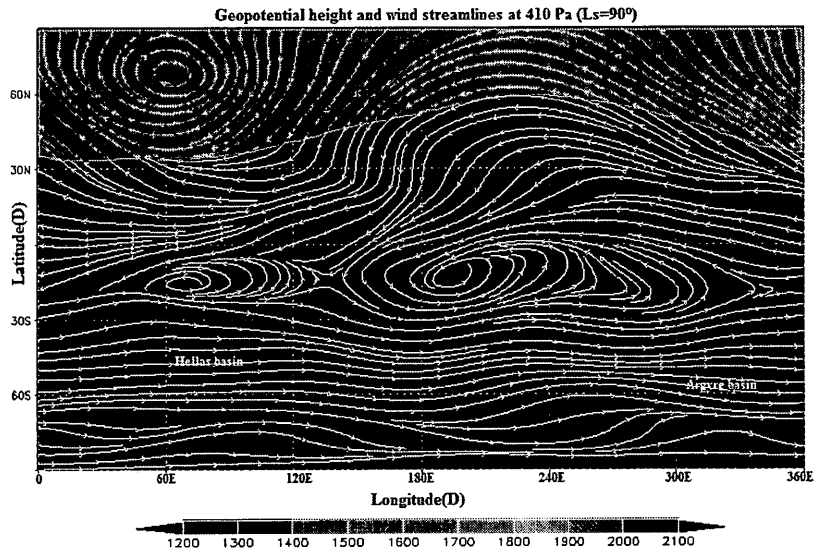

Figure 4.6: Instantaneous geopotential height and wind streamlines in the flat topography model simulation at 410 Pa (Ls = 90°). The colour bar shows geopotential height.

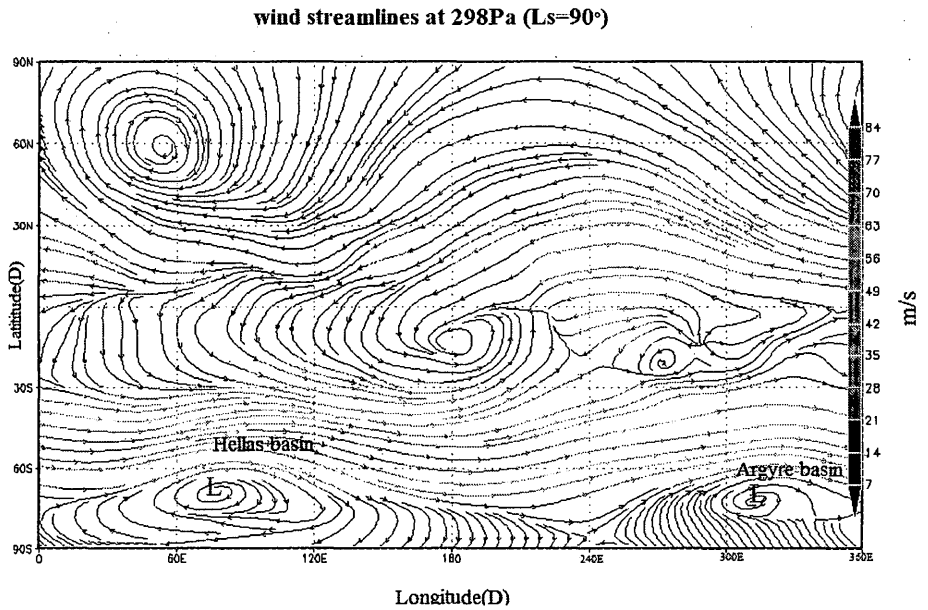

Figure 4.7: Wind streamlines in the realistic topography model simulation at 298 Pa (Ls = 90°).

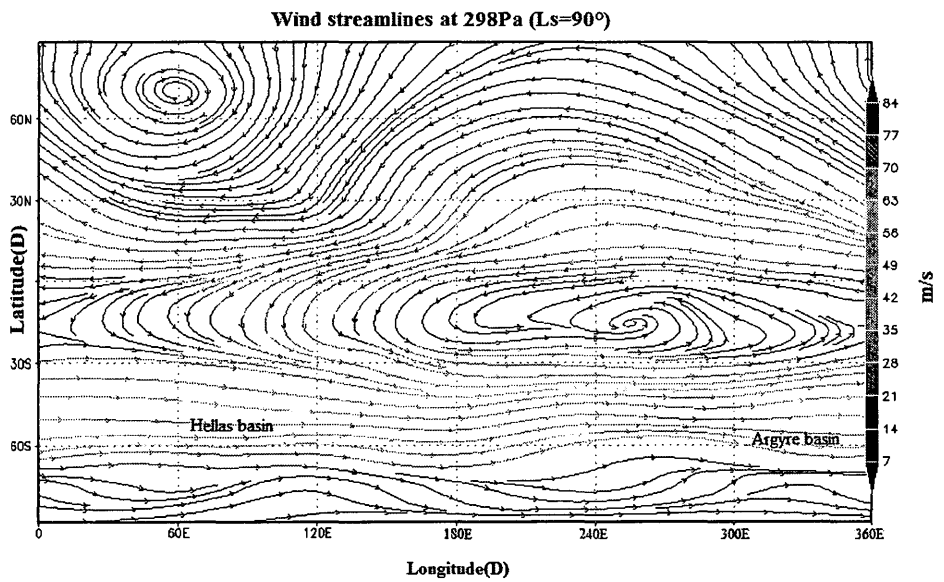

Figure 4.8: Wind streamlines in the flat topography model simulation at 298 Pa (Ls = 90°).

In order to gain a better understanding the weather patterns during fall to spring in the Martian southern hemisphere, the wind streamlines from Ls = 20° (early southern fall) to Ls = 200° (early southern spring) at a frequency of one degree of one Ls have been analyzed and will be explained in chapter 5.

4.3Rossby Waves

Rossby waves are long-waves or planetary-scale waves which have key influences on the atmospheric circulation. These waves are generated in the troposphere by ocean-land temperature contrasts or topographic forcing (e.g. winds flowing over mountains). These waves can be in both barotropic and baroclinic forms. In an inviscid barotropic fluid of constant depth (where the divergence of the horizontal velocity can be neglected), the barotropic Rossby wave is an absolute vorticity-conserving ($\eta = \zeta + f$, where η is absolute vorticity, is the relative vorticity and f is Coriolis parameter) motion that owes its existence to the variation of Coriolis parameter with latitude (beta effect). While in a baroclinic atmosphere, the Rossby wave is a potential vorticity-conserving motion (Equation 4.3) that owes its existence to the isentropic gradient of potential vorticity (Holton, 2004). Following Holton (2004) chapter 7.7, the barotropic Rossby wave zonal phase speed (c) relative to the mean zonal wind ($\bar{u}$) is

$$c - \bar{u} = -\beta/K^2 \tag{4.1}$$

where $\beta \equiv \frac{df}{dy}$, is the planetary vorticity gradient which arises because of the meridional variation of the coriolis force caused by the spherical shape of the Earth. Assuming the one dimensional wave case ($K^2 \equiv k^2$ where $k = 2\pi/L$) and when $\beta = 2\Omega cos\Phi/a$, then we have

$$c - \bar{u} = -(2\Omega \cos\Phi/4\pi^2 a)L^2 \qquad (4.2)$$

where Ω is angular velocity of the planet, Φ is the latitude, a is the mean planet radius and L is the wavelength. Therefore the number of waves in any particular latitude band is dependent upon a fine balance between the air flow speed through the trough/ridge system and the wavelength squared. Figure 4.9 shows a simple schematic of Rossby wave and low and upper level convergence and divergence.

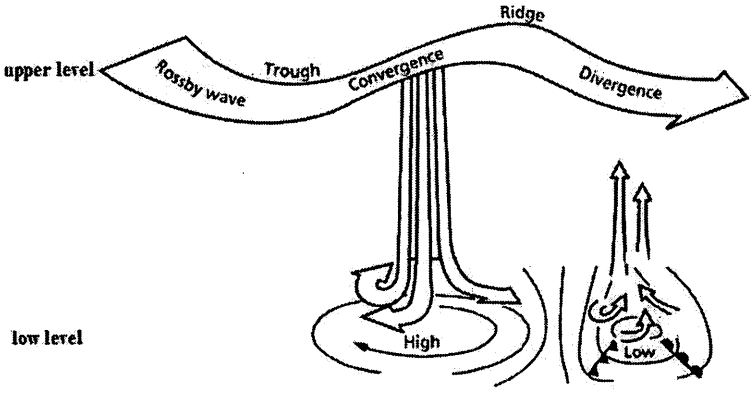

Figure 4.9: A simple schematic of Rossby wave and low and upper level convergence and divergence (from McGraw-Hill Dictionary of Scientific and Technical Terms, 6th edition).

4.3.1 Rossby Waves Vertical Propagation

On Earth Rossby waves can propagate vertically into the stratosphere where they are forced by topographical features (e.g. Himalaya and Rocky mountains in the Earth or Hellas basin and Argyre basins in the southern Martian hemisphere) or by land-sea diabatic heating differences (e.g. on Earth). Following Holton (2004) chapter 12.3, choosing a mid-latitude β-plane, where $\beta \equiv \frac{df}{dy}$ is constant and also by using the log-pressure coordinate system as $z = -H\, ln(\frac{p}{p_0})$ where H is a constant scale height, the quasi-geostrophic potential vorticity (QGPV) equation is written as

$$\frac{dq}{dt} = 0 \tag{4.3}$$

or $$\left(\frac{\partial}{\partial t} + V_g.\nabla\right) \mathrm{q} = 0$$

where

$$q \equiv f + \nabla^2\psi + \frac{f^2}{\rho_0 N^2}\frac{\partial}{\partial z}\left(\rho_0 \frac{\partial \psi}{\partial z}\right).$$

Here $\psi = \frac{\Phi}{f_0}$ is the geostrophic streamfunction, $f_0$is constant mid-latitude reference value of the Coriolis parameter and $N^2 = g\frac{d\, ln\theta_0}{dz}$ is the Brunt–Väisälä frequency squared. The Rossby waves are manifested as a small-amplitude disturbance on a constant zonal-mean flow. The flow is broken up into a mean state and perturbation state, such that $\psi = \bar{\psi} + \psi'$ and $\mathrm{q} = \bar{\mathrm{q}} + \mathrm{q}'$. If the decompositions are substituted into the equation 4.3 and linearized the perturbation field satisfies

$$\left(\frac{\partial}{\partial t}+\bar{u}\frac{\partial}{\partial x}\right)q'+\beta\frac{\partial\psi'}{\partial x}=0 \tag{4.4}$$

where $$q'\equiv\nabla^2\psi'+\frac{f^2}{\rho_0 N^2}\frac{\partial}{\partial z}\left(\rho_0\frac{\partial\psi'}{\partial z}\right).$$

Equation (4.4) has separate solutions in form of,

$$\psi'(x,y,z,t)=\psi(z)e^{i(kx+ly-c_x t)+z/2H} \tag{4.5}$$

where $c_x$is the zonal phase speed. Substituting (4.5) into (4.4) gives

$$\frac{d^2\psi}{dz^2}+m^2\psi=0 \tag{4.6}$$

where

$$m^2\equiv\frac{N^2}{{f_0}^2}\left[\frac{\beta}{(\bar{u}-c_x)}-(k^2+l^2)\right]-\frac{1}{4H^2}$$

If we assume stationary Rossby waves, then $c_x=0$ and m^2 must be positive for waves which propagatevertically, we see that vertically propagating modes can only exist when the mean zonal flow satisfies following condition:

$$0<\bar{u}<\beta[(k^2+l^2)+\frac{{f_0}^2}{4N^2H^2}]^{-1}=U_c \tag{4.7}$$

where is the Rossby critical velocity. So vertical propagation of the Rossby waves can only occur in the presence of westerly winds weaker than a critical value which depends on the horizontal scale of the waves. Also equation (4.6) shows that only the long waves are able to propagate vertically (i.e. smallk^2).

4.4 Vertical structure of South the Polar Front Jet

Figure 4.10 shows the vertical cross-section of the zonally averaged wind streamlines around Ls = 90°. The appearance of a discontinuity line (i.e. when the wind direction changes from easterlies into the westerlies) around 78°S, which is smoothly tilted to higher altitudes, is associated with the breaking up of the south polar jet stream or south polar front jet. This sharp shift in wind illustrates cold polar front and therefore we see that the streamlines are terminated at the cold front. The vertical wind shear (e.g. Figure 3.6) which extends below the core of the south polar jet is associated with southern hemisphere latitudinal temperature gradients that extend to the surface (e.g. Figure 3.5). Based on polar front theory this vertical shear is associated with a southern cold polar front. As was showed in the previous section, this cold front jet can be broken up into Rossby waves and form cellular patterns (cyclonic and anti-cyclonic). Figure 4.11 is same as Figure 4.10 but for the flat topography simulation. So the structure described above cannot be seen when topography has been removed in the model simulation.

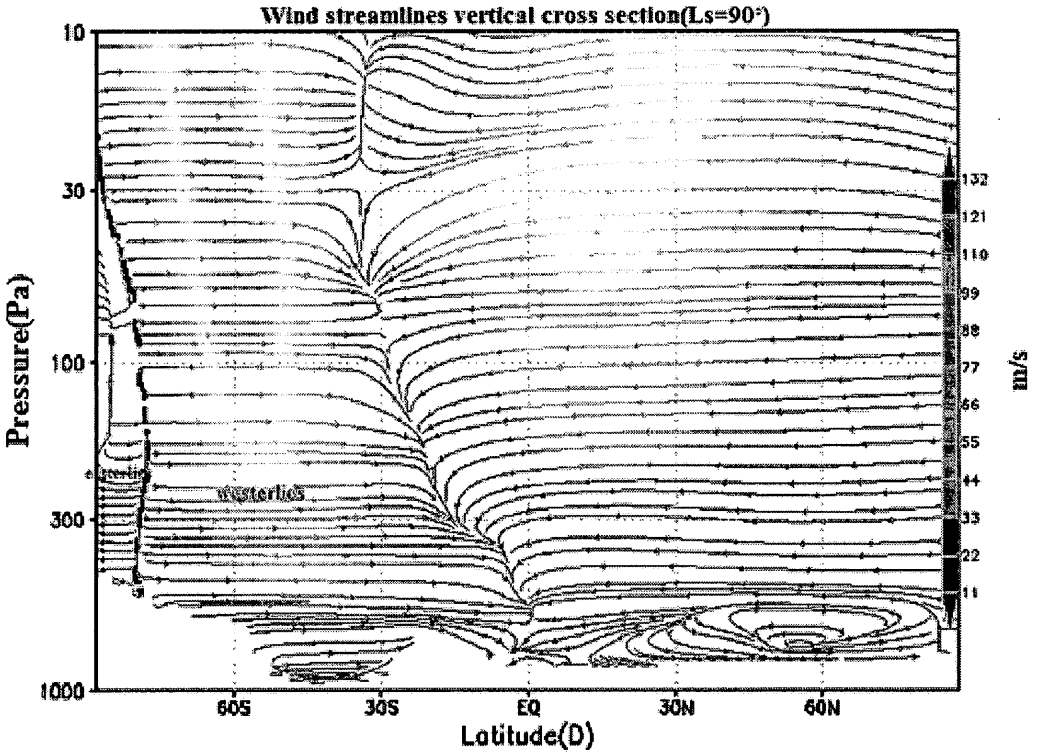

Figure 4.10: Vertical cross section of the wind streamlines for the realistic topography model simulation (Ls = 90°).

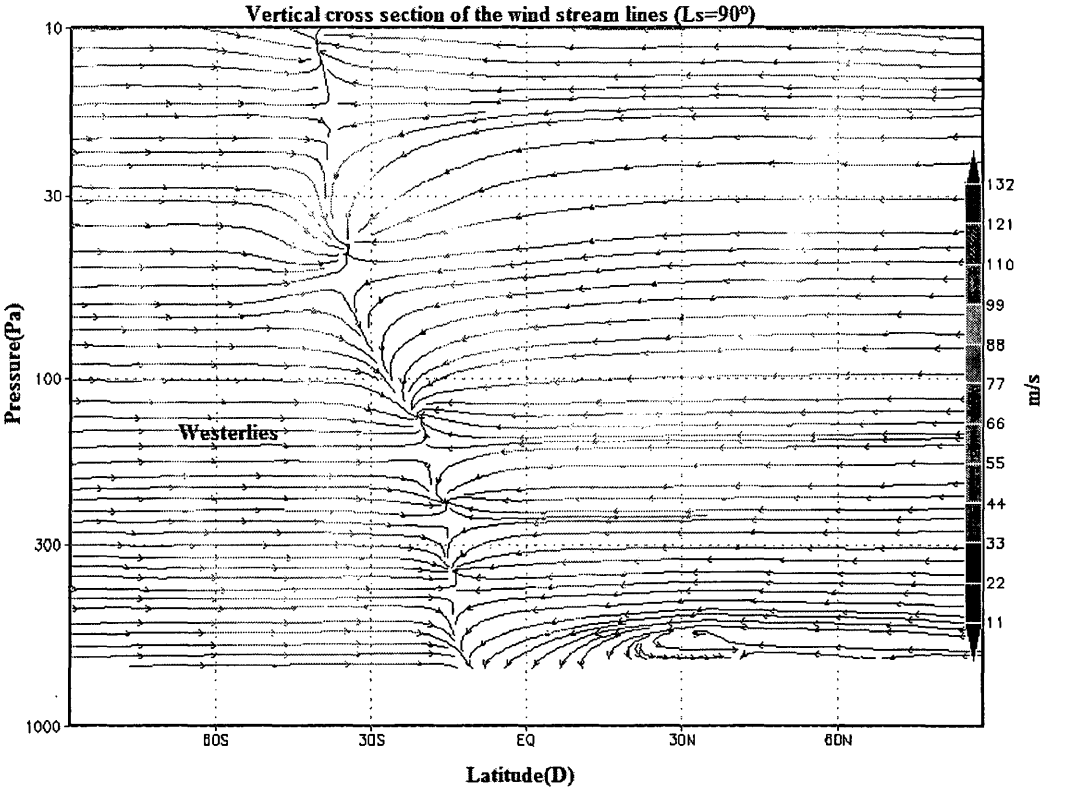

Figure 4.11: Vertical cross section of the wind streamlines for the flat topography model simulation (Ls = 90°).

4.5 Conclusions

Generally, the low-level air temperature pattern in the flat topography simulation is very smooth in comparison with the realistic topography for southern and northern mid-latitudes. The temperature and wind patterns in the southern mid-latitudes during southern winter in the flat topography simulation have nearly zonal structures whereas in the realistic topography simulation they have cellular structures with cyclonic and anti-cyclonic patterns which are important in the southern Martian winter weather (chapter 3

and chapter 5). The south polar jet stream band has a smooth pattern in the flat topography simulation whereas in the realistic topography simulation the night polar jet core has a broken pattern, as a result of the stationary topographic Rossby wave formation.

Chapter 5

Topography and Albedo Impacts at the Martian South Polar CO_2 Ice Cap

5 Introduction

The Martian atmosphere is approximately 95% CO_2 where about 30% condenses at each polar surface during fall and winter seasons when the temperature falls below ~148K around the carbon dioxide condensation temperature (James et al., 1992; Forget et al., 1998). Due to the seasonal variation in solar radiation at the polar regions, CO_2 can alternatively condense during late fall and winter and sublimate in at late spring and summer. Variations in the solar insolation also controls both the depth and horizontal extent of the CO_2 layers and drives exchange of CO_2 content between caps and the atmosphere (see sections 1.2 and 1.3).

5.1 Martian South Polar Cap

The Martian south pole is characterized by a longitudinally asymmetric residual ice-cap composed of both CO_2 ice and water ice (Section 1.3). On the other side (compared to the residual ice cap) there is an ice free region during summer called the cryptic region[9]. The southern residual ice cap is confined between 240°E and 360°E and 0°E and 30°E longitude and nearly from the pole to ~82.5°S. The opposite side i.e. the cryptic region mostly covers between 75°S and 85°S in latitude and 50°E to 210°E in longitude and is characterized by low albedo (Titus et al., 2003 and Kieffer et al., 2000). Some properties of ice polar caps have been explained in section 1.3.

Due to the different reflectance properties of CO_2 ice and water ice, the spectral information indicates the differences between them. Figures 5.1a and 5.1b (from Mohammed, 2010), show the transmission spectra that were acquired from Bernard Schmitt and Sylvain Douté in Grenoble, France at the Laboratoire de Glaciologie et Géophysique de l'Environment (LGGE) in association with CNRS (centre national de la recherché scientific). Figure 5.1a shows that the absorption features for carbon dioxide ice are located primarily at 1.4μm, 1.6μm and a few lines surrounding 2.0μm depending on thickness of carbon dioxide ice sample whereas absorption lines for water ice (Figure 5.1b) are broad and centred primarily at 1.5μm and 2.0μm (Langevin et al., 2006a).

[9] During the disappearing of the seasonal ice cap when the sun's rays make into the deeper layers, the spots, spiders and fans developing in the cryptic region, they were detected by Mars Orbiter Camera on Mars Global Surveyor.

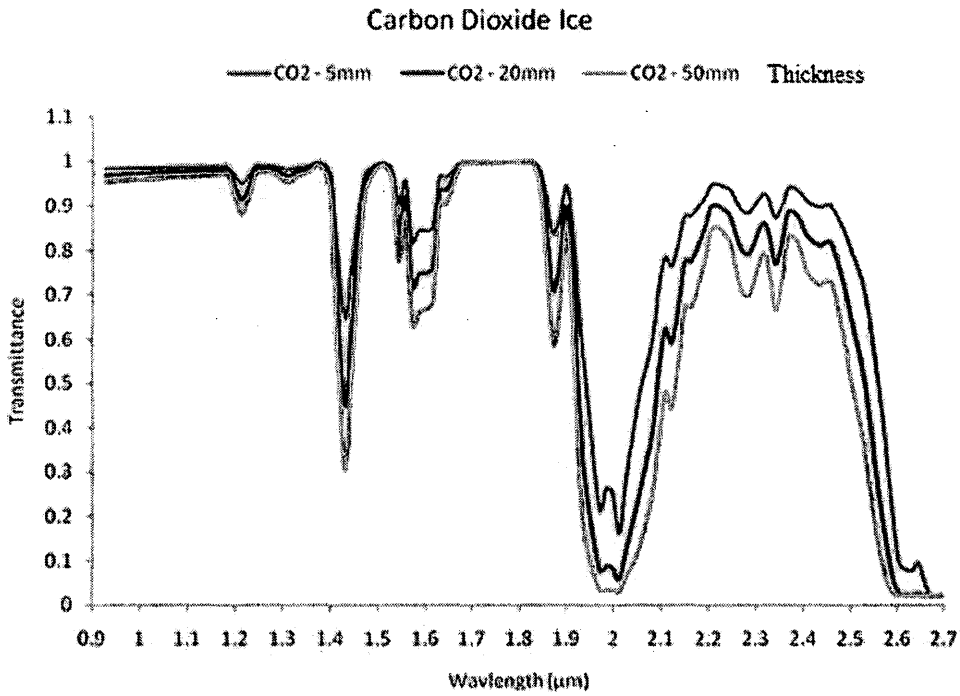

Figure 5.1a: Carbon dioxide ice transmittance spectra from LGGE. Narrow absorption bands are located primarily at 1.4 μm, 1.6 μm and a few lines surrounding 2.0 μm (Langevin et al., 2006a). The blue, red and green spectra are for 5 mm, 20 mm and 50 mm sample thickness, respectively (Figure from Mohammed, 2010).

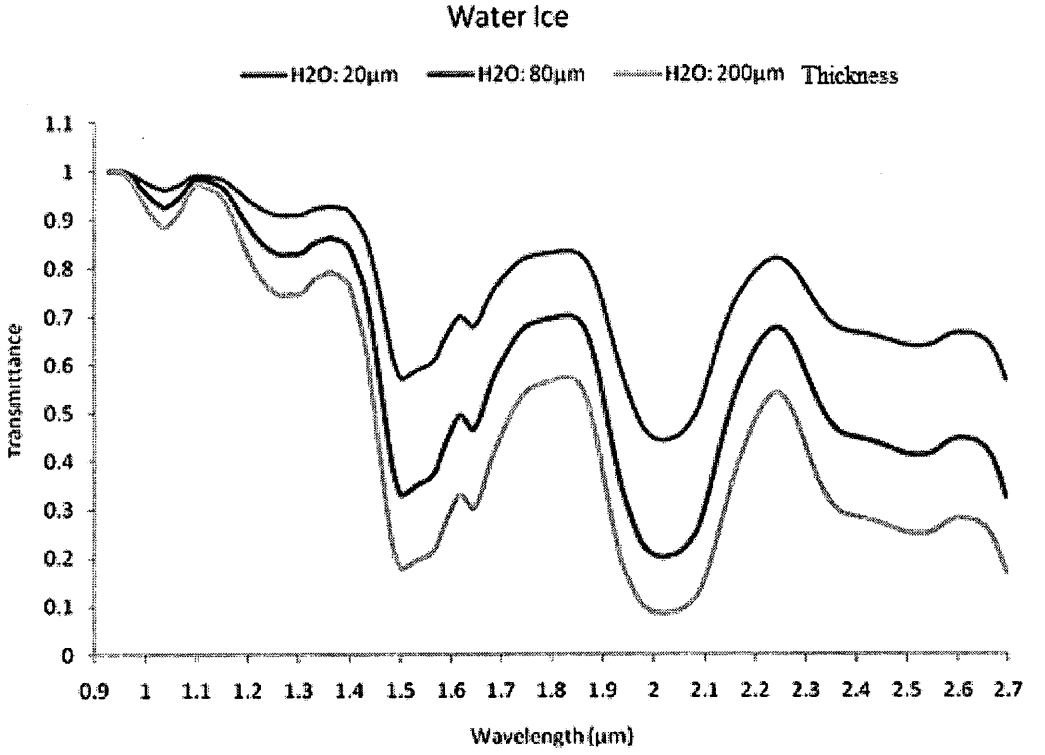

Figure 5.1b: Water ice transmittance spectra from LGGE. Broad absorption bands are centred at 1.5μm and 2.0μm (Langevin et al., 2006a). The blue, red and green spectra are for 20mm, 80mm and 200mm sample thickness, respectively (Figure from Mohammed, 2010).

Figure 5.1c is a mosaic image which was built from ten observations by the OMEGA Visible and Infrared Mineralogical Mapping Spectrometer onboard ESA's Mars Express, during the Martian early to mid southern spring. The albedo is evaluated assuming a perfectly diffusive surface (Lambert albedo). The grey scale extends from 10% (black) to 80% (white). Over part of the image, a false colour scheme is implemented, with each of the three colour channels remaining proportional to the reflectance factor at 1.08 μm; the red channel is enhanced proportionally to the CO_2 band depth at 1.43 μm; and the blue and green channels are enhanced proportionally to the

H_2O ice band depth at 1.5 μm. The low albedo region within the cap very closely matches the cryptic region determined by Thermal Emission Spectrometer (TES). Most of the seasonal and residual ice cap spectra are dominated by CO_2 ice (reddish tones), with very bright regions ('a': 345° E, 86.2° S, albedo ~80%) and less bright regions with much stronger CO_2 ice signatures ('b': 68° E, 73° S, albedo ~42%). The seasonal cap is compositionally very heterogeneous between longitudes 60° E and 220° E. Relatively bright (albedo >40%) areas are spectrally dominated by either CO_2 ice (reddish tones) or H_2O ice (bluish tones; for example, region 'c' at 200° E, 72.8° S). Within the cryptic region itself, defined by albedos <30% at latitudes higher than 70° S, signatures of both CO_2 ice and H_2O ice are much weaker than those observed in other areas of the seasonal cap. A representative area (80° E, 82.5° S), with an albedo of ~25%, is labelled 'd'.

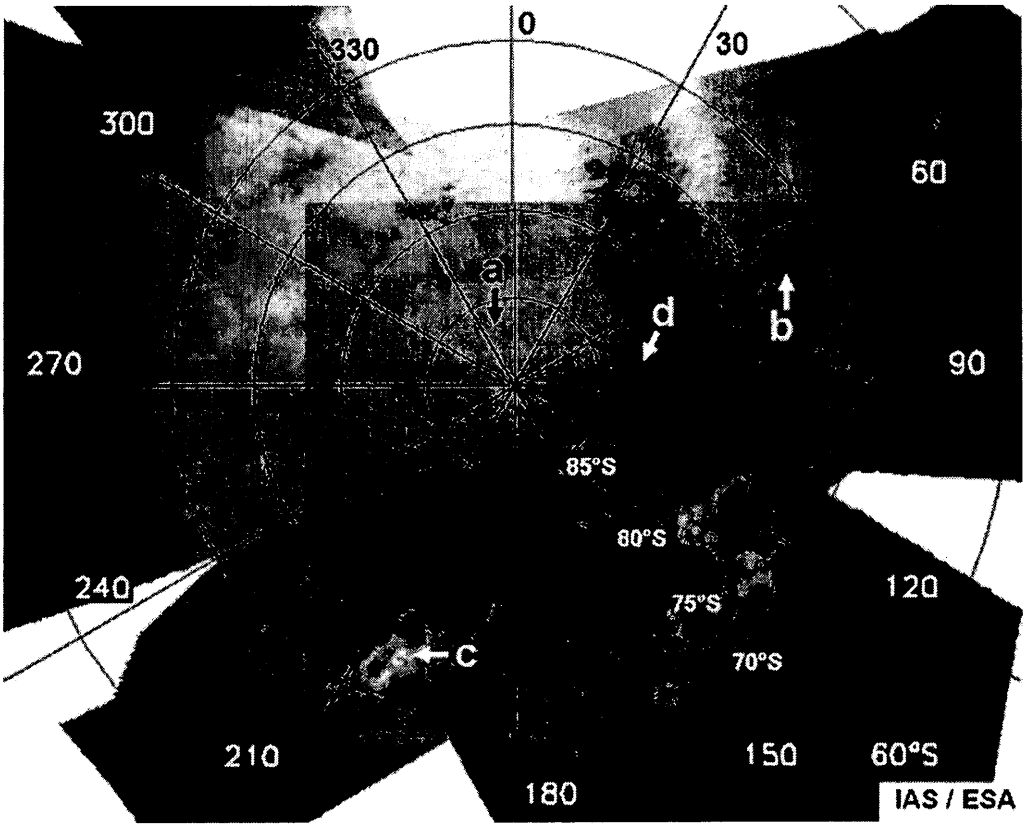

Figure 5.1c: This mosaic image was built from ten observations by the OMEGA Visible and Infrared Mineralogical Mapping Spectrometer on board ESA's Mars Express, during the Martian early to mid-Spring. a: bright, fine-grained "CO_2 ice" (reddish tone changes base on spectral properties e.g. Figure 5.1a), b: larger grained "CO_2 ice" which is not quite as bright, c: water ice frost, d: cryptic region.

5.1.1 CO_2 Ice Accumulation Mechanism at Martian South Polar Cap

The style of surface CO_2-ice formation over the Martian south polar regions has two different mechanisms that can build up a seasonal ice cap. One possibility is that the frost formation is due to the direct deposition of CO_2-ice when the surface temperature and the air temperature in the bottom atmospheric layer near the surface is less than the

frost point temperature of CO_2 (~146-148 K)[10]. However, precipitation of CO_2 snow occurs by condensation in the atmospheric column followed by CO_2 snow falling to the surface and surviving if the surface temperature is equal or less than CO_2 freezing temperature. Thus, these two different deposition processes can control the south polar cap albedo. It is anticipated that small CO_2 ice grains or CO_2 snow, freshly precipitated to the surface results in bright surfaces or higher albedo while direct-depositing ice forms larger and rougher CO_2 frost grains in the surface resulting in darker surfaces and smaller albedo (Kieffer et al., 2000; Titus, et al., 2001). Therefore, it is the darker frosty zones (cryptic region) that sublimate more rapidly during late spring and summer rather than the brighter areas covered by snow (Kieffer et al., 2000; Piquex et al., 2003). Therefore, the darker frosty zones can completely disappear during the summer. In addition, these deposition mechanisms are dependent on two different types of regional weather which occur during late fall and winter. These two mechanisms result from different aspects of the dynamical forcing of the large scale topographical impacts of the Hellas and Argyre basins. These can be seen from the NASA Ames Mars General Circulation Model (Colaprete, et al., 2005) and the second version of Global Mars Multiscale Model simulations.

[10] The frost point temperature of CO_2 is a function of atmospheric pressure (see section 5.2.2).

5.2 CO_2 Condensation and Sublimation in the Model

Here we describe how the condensation and sublimation of CO_2 on the ground and in the atmosphere are calculated in the model. The condensation and sublimation of carbon dioxide on the ground is primarily controlled by relatively simple physical processes. When the surface temperature falls below the condensation temperature, CO_2 condenses and releases the latent heat required to keep the solid-gas interface at the condensation temperature. Conversely, when CO_2 ice is heated, it partially sublimes to keep its temperature at the frost point temperature. Also the loss of atmospheric CO_2 mass due to condensation (or conversely the gain due to sublimation) has to be taken into account to modify the surface pressure at each time step.

5.2.1 CO_2 Condensation and Sublimation in the Atmosphere

The model atmosphere consists of N layers (Akingunola, 2008). In each layer, at each computational time step, the CO_2 gas condensation occurs when the predicted temperature T_k is less than the local condensation temperature of CO_2, $T_{CO_{2_k}}$ in Kelvin, at any vertical level k in the model. The frost-point temperature is a function of CO_2 pressure, $P_{co_2}(Pa)$ given by, Read and Lewis (2004) as (Figure 5.2);

$$T_{CO_2} = 149.2 + 6.48 \ln\left(0.00135 P_{co_2}(Pa)\right), \tag{5.1}$$

If T is low enough, then the mass of the atmospheric CO_2 gas which may condense out of the topmost layer ($k = N$) of the atmosphere is obtained from the heat energy balance by;

$$\delta m_N = C_P M_N \frac{(T_{CO_{2N}} - T_N)}{L_H}, \quad (5.2)$$

where δm_N is the mass of ice that has condensed (and is greater than zero when condensing), M_N is the mass of the CO_2 in the topmost layer, C_P the specific heat of CO_2 at constant pressure, and L_H = 5.9x10^5 J kg^{-1} is the latent heat of condensation of CO_2. This ice is assumed to be instantaneously transported to the layer below (this is a simple representation of the settling process). Below this level, the fact that the atmosphere might have condensed in the layers above must be taken into account (Forget et al., 1998) as;

$$\delta m_k = C_P M_k \frac{\left(T_{CO_{2_k}} - T_k\right)}{L_H} - \frac{1}{L_H}\left[g(z_{k+1} - z_k) + ci_k \left(T_{CO_{2_{k+1}}} - T_{CO_{2_k}}\right)\right] \sum_{l=k+1}^{N} \delta m_l \quad (5.3)$$

where, z_k is the altitude in middle of layer k; g is the acceleration due to Mars gravity, and ci_k= 349 + 4.8 T_K in J kg^{-1} K^{-1} is the specific heat of CO_2 ice. The term $[g(z_{k+1} - z_k)] \sum_{l=1}^{k-1} \delta m_l$ corresponds to the potential energy released by this amount of CO_2 ice falling from layer $k+1$ (aerodynamical friction). The term $\left[ci_k \left(T_{CO_{2_{k+1}}} - T_{CO_{2_k}}\right)\right] \sum_{l=k+1}^{N} \delta m_l$ corresponds to the energy used to heat the ice mass $\sum_{l=k+1}^{N} \delta m_l$ from the temperature $T_{CO_{2_{k+1}}}$ to $T_{CO_{2_k}}$. Also the ice in the atmosphere can resublime during its descent. On decent, condensed atmospheric CO_2 ice resublimes if it encounters a warmer layer when the predicted temperature is greater than the CO_2 frost point temperature. Then an amount $\delta m_k < 0$ is sublimed, and the layer temperature is set to the frost-point temperature. However, if all the condensed CO_2 ice falling from upper layers sublimes in

a layer, i.e. if $-\delta m_k > \sum_{l=k+1}^{N} \delta m_l$, then δm_k is set equal to $-\sum_{l=k+1}^{N} \delta m_l$, and the updated layer temperature is given by;

$$T_k^{new} = T_k + \frac{1}{C_P M_k}\left[-L_H + g(z_{k+1} - z_k) + ci_k\left(T_{CO_{2_{k+1}}} - T_{CO_{2_k}}\right)\right]\sum_{l=k+1}^{N} \delta m_l \quad (5.4)$$

5.2.2 CO_2 Condensation and Sublimation on the Ground

The total mass of CO_2 ice deposited on the ground surface in each time step is the sum of atmospheric CO_2 ice falling to the ground, and that formed at the surface layer. The mass of condensate on the ground is calculated using the same equation as that of the atmospheric condensation (equation 4.3) with $k = 0$ and replacing $C_P M_k$ to $C_s A$, where C_s =833.4 J m^{-2} K^{-1} is the surface heat capacity (Christiansen and Moore, 1992) and A is the surface area of the grid mesh. At each time step, the mass $\sum_{l=0}^{N} \delta m_l$ is added to the amount of ice on the ground m_0 . Then $T_0 = T_{CO_{2_0}}$, unless the ground ice completely sublimes (when $-\delta m_0 > m_0 + \sum_{l=1}^{N} \delta m_l$ is predicted). Then δm_0 is set to $\delta m_0 = -m_0 - \sum_{l=1}^{N} \delta m_l$ and new surface temperature is calculated as:

$$T_0^{new} = T_0 - \frac{L_H}{C_s A} m_0 - \frac{1}{C_s A}\left[L_H - g z_1 - ci_0\left(T_{CO_{2_1}} - T_{CO_{2_0}}\right)\right]\sum_{l=1}^{N} \delta m_l \quad (5.5)$$

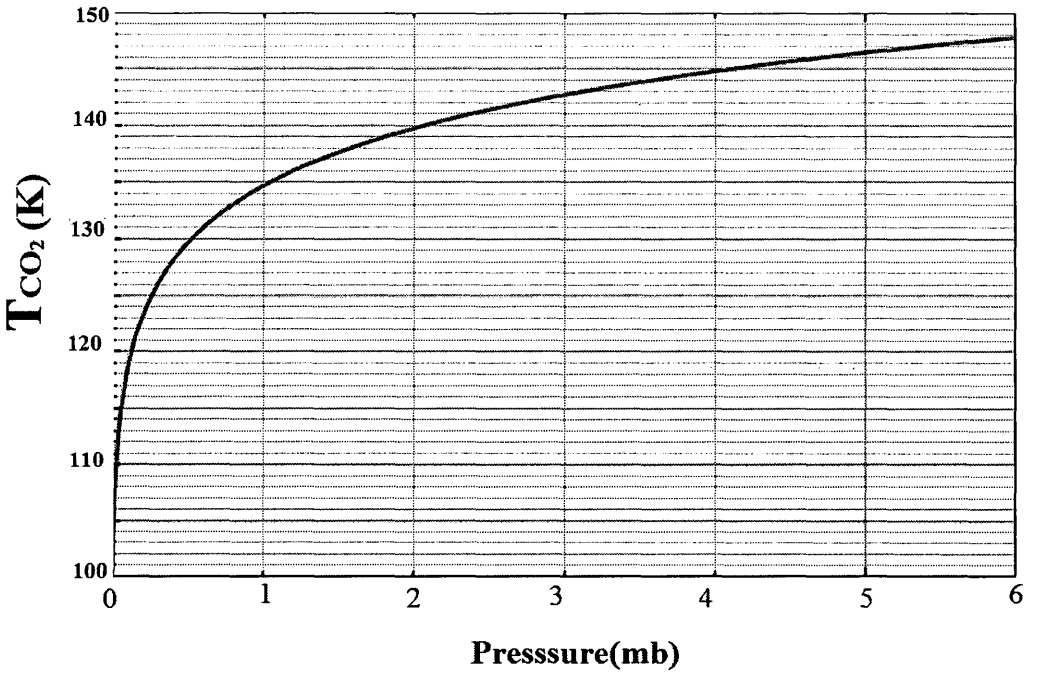

Figure 5.2: The frost-point temperature is as a function of CO_2 pressure given by Read and Lewis, (2004).

5.3 Model Results

In the following sub-sections the temporally averaged temperature distribution in different seasons (i.e. winter, spring, summer and fall) at different sub-polar latitudes will be discussed to understand the asymmetrical nature of the south polar ice cap during ice formation or sublimation based on temperature structure.

Here, in the plotted figures the data were interpolated or extrapolated (bi-linearly by using the GrADS (http://www.iges.org/grads/) if needed.

5.3.1 Model Results (L_S: 60°-80°)

The late fall season is very important for the study of ice caps for both hemispheres because the atmosphere cools and the seasonal ice cap begins to build up. The maximum expansion rate of the south seasonal CO_2 ice cap occurs in the Ls range 80°-90° (Forget, 1998). In this study, we look at the vertical structure of temperature for fixed latitudes but different longitudes. Figures 5.3a and 5.3b show the temporally averaged temperature-pressure distribution in the Ls range 60°-80° (southern late fall) centred around Ls = 70° at 56°S and 64°S , respectively. Figure 5.3a shows a wide warm column air between 30°-240°E (cryptic region) below 80 Pa and a cold column of air around 60°W (300°E) below ~200 Pa. Figure 5.3b shows that near 60°W (300°E), the cold column of air can make atmospheric condensation possible, and thus, snow precipitation can occur (i.e. from the Figure 5.2, the CO_2 condensation temperature at pressure ~5-5.5mb is calculated ~146-147 K). Between 160°E and 240°E (120°W), and also between 30°E and 65°E, with an upper warmer air column, direct deposition can occur on the surface if the near surface (in bottom atmospheric layer) temperature permits condensation, thus forming frost over the cryptic region. Another cold air column below 300 Pa, although rather weak, can be seen around 120°E.

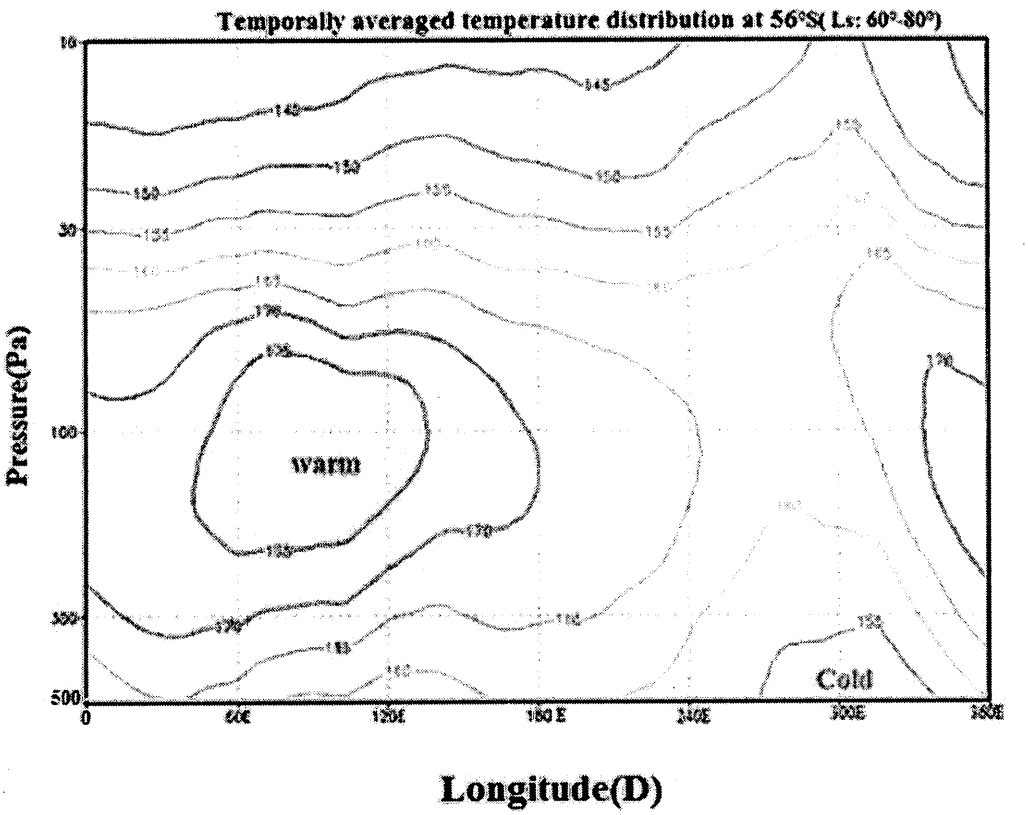

Figure 5.3a: A 2D temporally averaged temperature-pressure distribution at 56°S in the Ls range 60°-80° (southern late fall) centred around Ls = 70°.

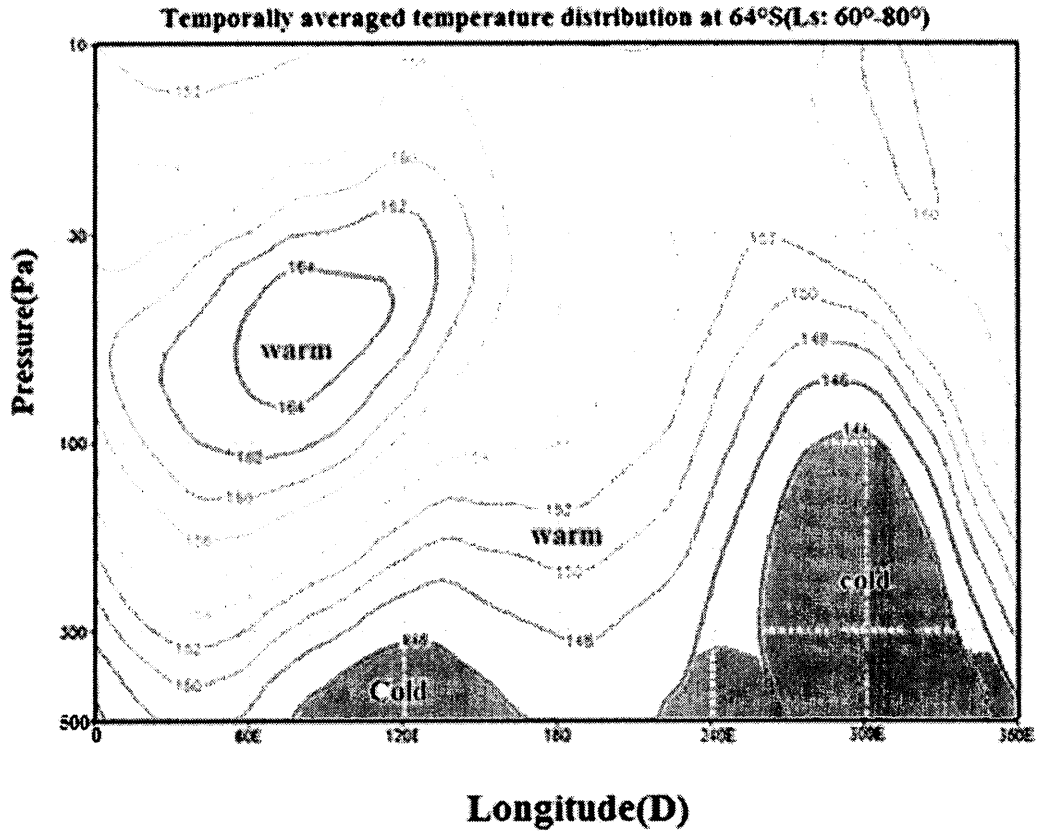

Figure 5.3b: A 2D temporally averaged temperature-pressure distribution at 64°S in the Ls range 60°-80° (southern late fall) centred around Ls = 70°. The approximate area where the temperature is below the condensation point of CO_2 is marked in blue.

5.3.2 Model Results (L_S: 80°-100°)

Figures 5.4a and 5.4b show the temporally averaged temperature-pressure distribution in the Ls range 80°-100° (southern late fall-early winter) centred around Ls = 90° at 60°S and 68°S respectively. Figure 5.4a shows two cold troughs centred around 90°E and 300°E below 100Pa. Also two warm air ridges around 30°E and 180°E can see in this figure. Figure 5.4b shows two cold columns centred around 100°E and 300°E

below 100Pa. Similar to figure 5.4a, around 35°E and 180°E two warm air ridges can see. Both Figures 5.4a shows longitudinal temperature variation in the southern sub-polar regions

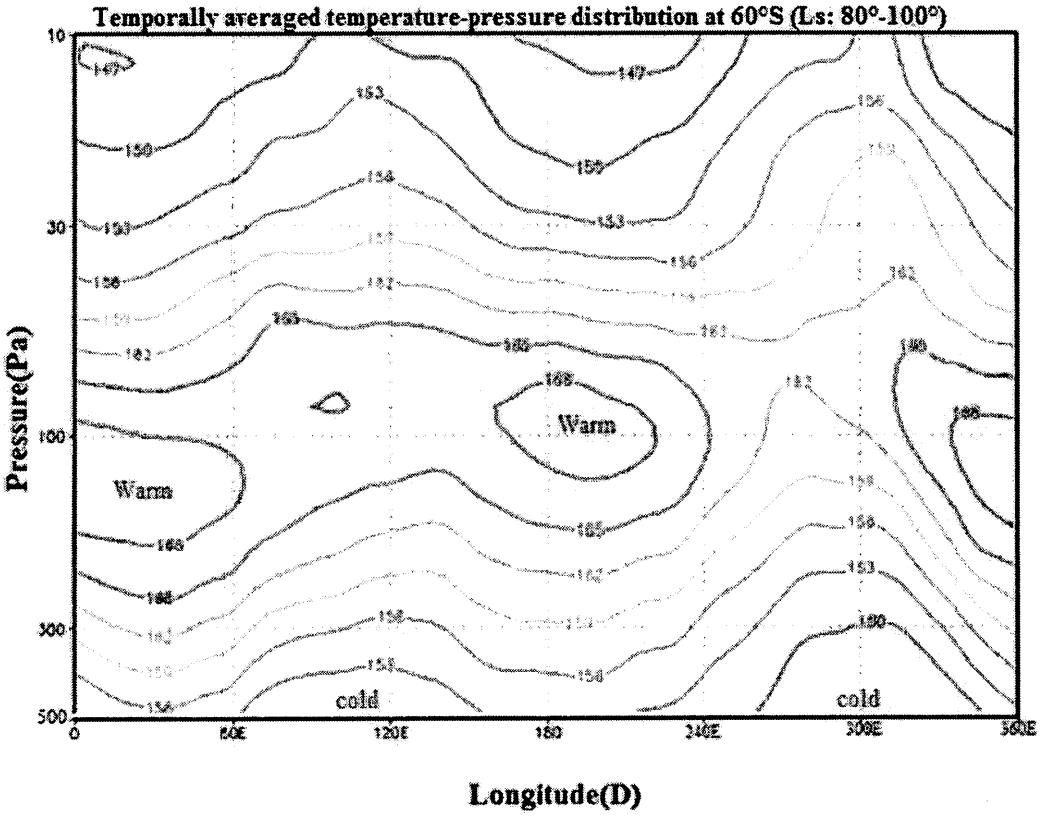

Figure 5.4a: A 2-D temporally averaged temperature-pressure distribution at 60°S in the Ls range 80°-100° (southern late fall-early winter) centred around Ls = 90°.

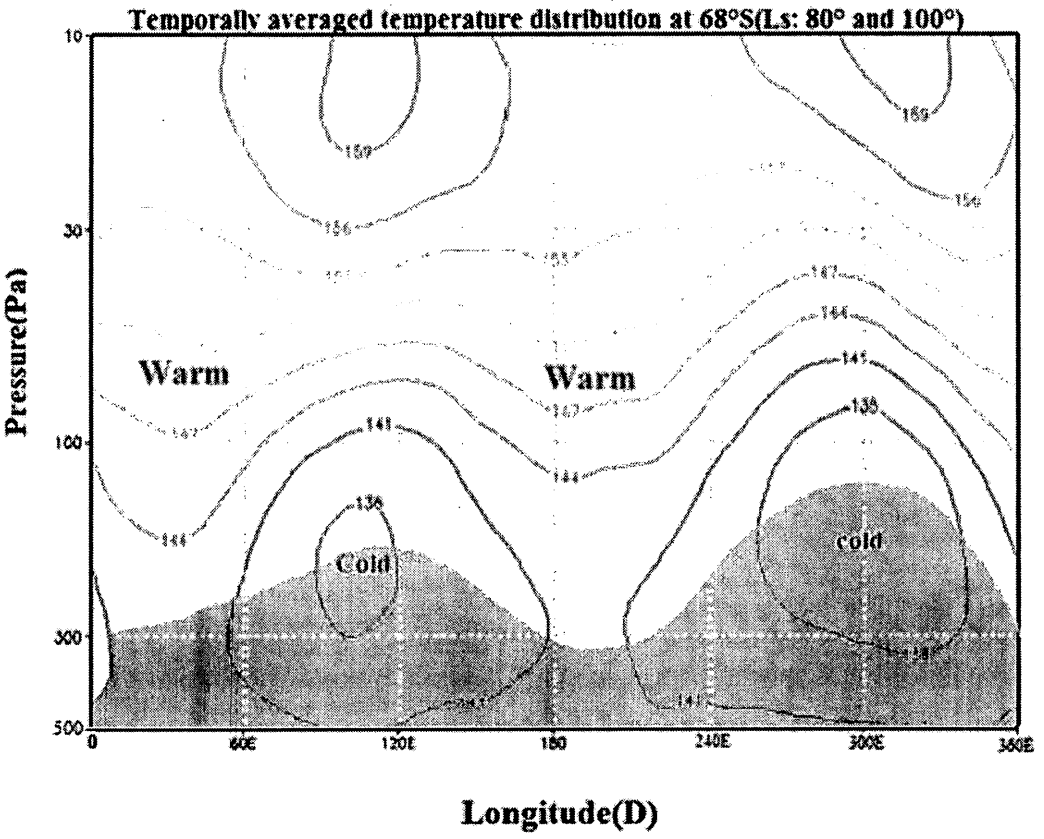

Figure 5.4b: A 2-D temporally averaged temperature-pressure distribution at 68°S in the Ls range 80°-100° (southern late fall-early winter) centred around Ls = 90°. The approximate area where the temperature is below the condensation point of CO_2 is marked in blue. Here, in the plotted figure the data were interpolated or extrapolated (bi-linearly by using the GrADS (http://www.iges.org/grads/) if needed.

5.3.3 Model Results (L_S: 170°-190°)

The spring polar cap is characterized by small-scale inhomogeneities in the polar cap boundary and in the albedos within the frost-covered region (Forget, 1998). Thus, the south seasonal CO_2 ice cap in the frost-covered regions loses CO_2 ice faster than the snow-covered regions (Forget, 1998).

This section will present the temporally averaged temperature-pressure distribution during the southern, late winter to early spring. Figures 5.5a and 5.5b show the temporally averaged temperature-pressure distribution in the Ls range 170°-190° (southern late winter-early spring) centred around Ls = 180° at 68°S and 80° respectively. Figure 5.5a shows a wide warm air column centred around 240°E below 100Pa. Figure 5.5b show longitudinal asymmetry for temporally averaged temperature-pressure distribution for southern sub-polar regions during L_S ~170°-190°. A warm air column with maximum temperature around 156 K can be seen around the Martian cryptic region (80°S, 220 °E) whereas around non-cryptic region (between 240°E and 360°E and 0°E and 30°E longitude) the temperature is colder than in the cryptic regions.

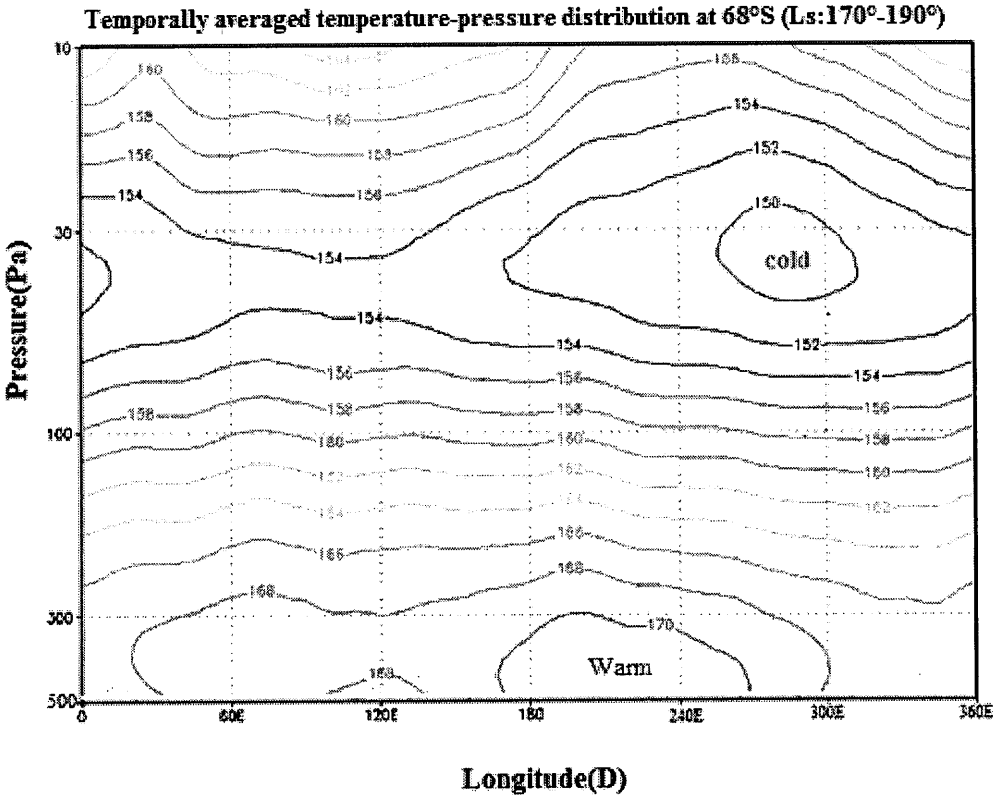

Figure 5.5a: A 2-D temporally averaged temperature-pressure distribution at 68°S in the Ls range 170°-190° (southern late winter-early spring) centred around Ls = 180°.

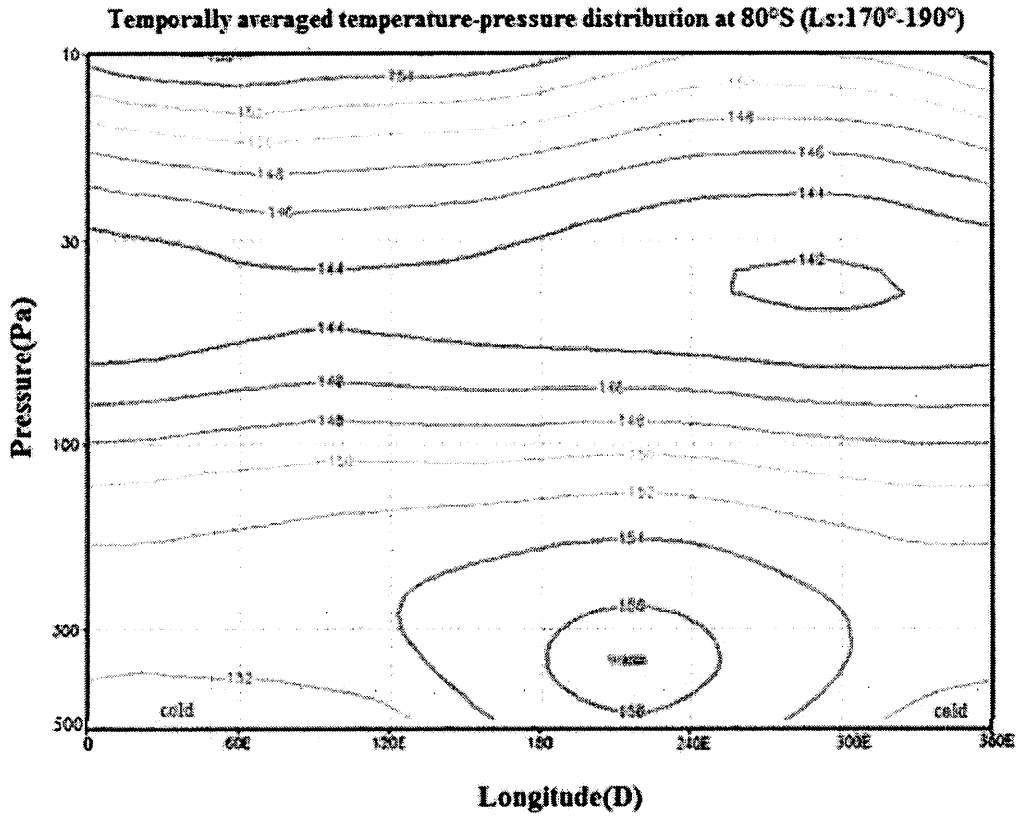

Figure 5.5b: A 2-D temporally averaged temperature-pressure distribution at 80°S in the Ls range 170°-190° (southern late winter-early spring) centred around Ls = 180°.

5.3.4 Model Results (L_S: 260°-280°)

At the end of spring and shortly before the summer solstice in the southern hemisphere (Ls = 262.6°) the south polar cap (which does not sublimate completely), as observed by Viking Orbiter 2 during the extended Viking mission, had an asymmetric shape and its centre was displaced by about 6° in latitude from the pole (James et al., 1979).

In this section the temporally averaged temperature-pressure distribution during southern late spring to early summer in the southern sub-polar region will be discussed.

This section will present the temporally averaged temperature-pressure distribution during northern late fall to early winter at northern sub-polar regions to compare with the pattern already seen in section 5.3.2 during southern late fall to early winter season.

Figure 5.6 shows the temporally averaged temperature-pressure distribution at 76°S in the Ls range 260°-280° (southern late spring-early summer) centred around Ls = 270°. This Figure shows that a relatively warm summery air mass dominates the southern hemisphere and the longitudinal asymmetry in the temperature pattern does not occure during this time period.

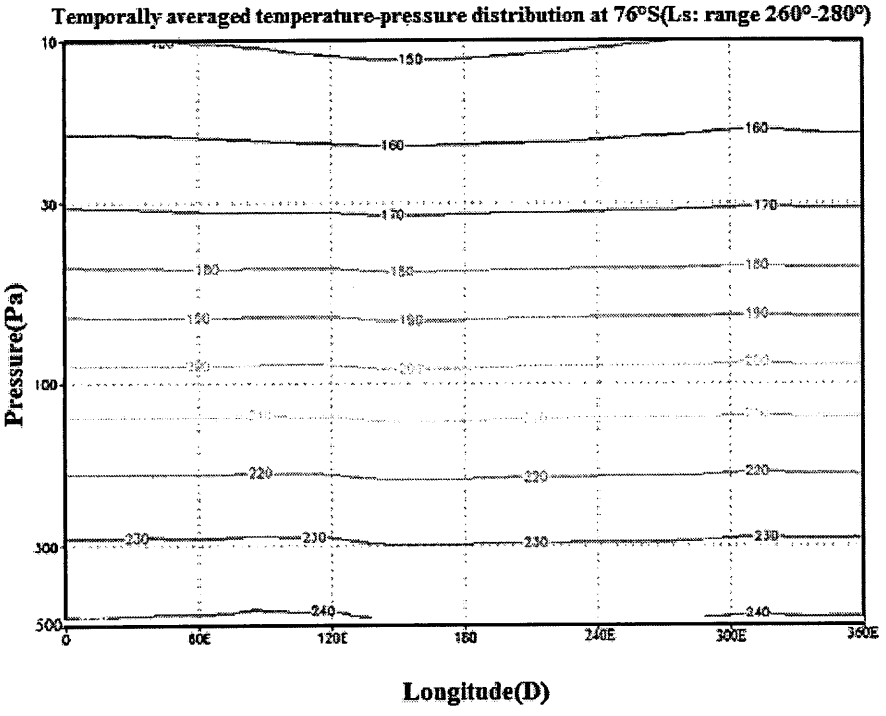

Figure 5.6: A 2-D temporally averaged temperature-pressure distribution at 76°S in the Ls range 260°-280° (southern late spring-early summer) centred around Ls = 270°.

Figures 5.7a and 5.7b also show the temporally averaged temperature-pressure distribution in the Ls range 260°-280° (northern late fall-early winter) centred around Ls = 270° at 60°N and 68°N respectively. Figure 5.7a shows that the temporally averaged temperature at 60°N is above the CO_2 frost temperature. The general pattern is nearly symmetric at different longitudes. Figure 5.7b shows a similar pattern as figure 5.7a. A cold trough with a temperature around 150 K can be seen below 300Pa. In both Figures 5.7a and 5.7b, the isotherms have nearly flat patterns and there is no remarkable longitudinal temperature variation.

By comparison of the general pattern of the temporally averaged temperature-pressure distribution for southern late fall-early winter (Figures 5.4a and 5.4b) and northern late fall-early winter (Figures 5.7a and 5.7b) remarkable longitudinal temperature variations in the southern sub-polar regions can be seen whereas there are nearly flat isotherms in its counterpart at nearly the same seasonal condition. The cause of longitudinal variation temperature in the Martian southern hemisphere is related to topographical Rossby wave formation during its winter season (sections 4.2, 4.3 and 5.4).

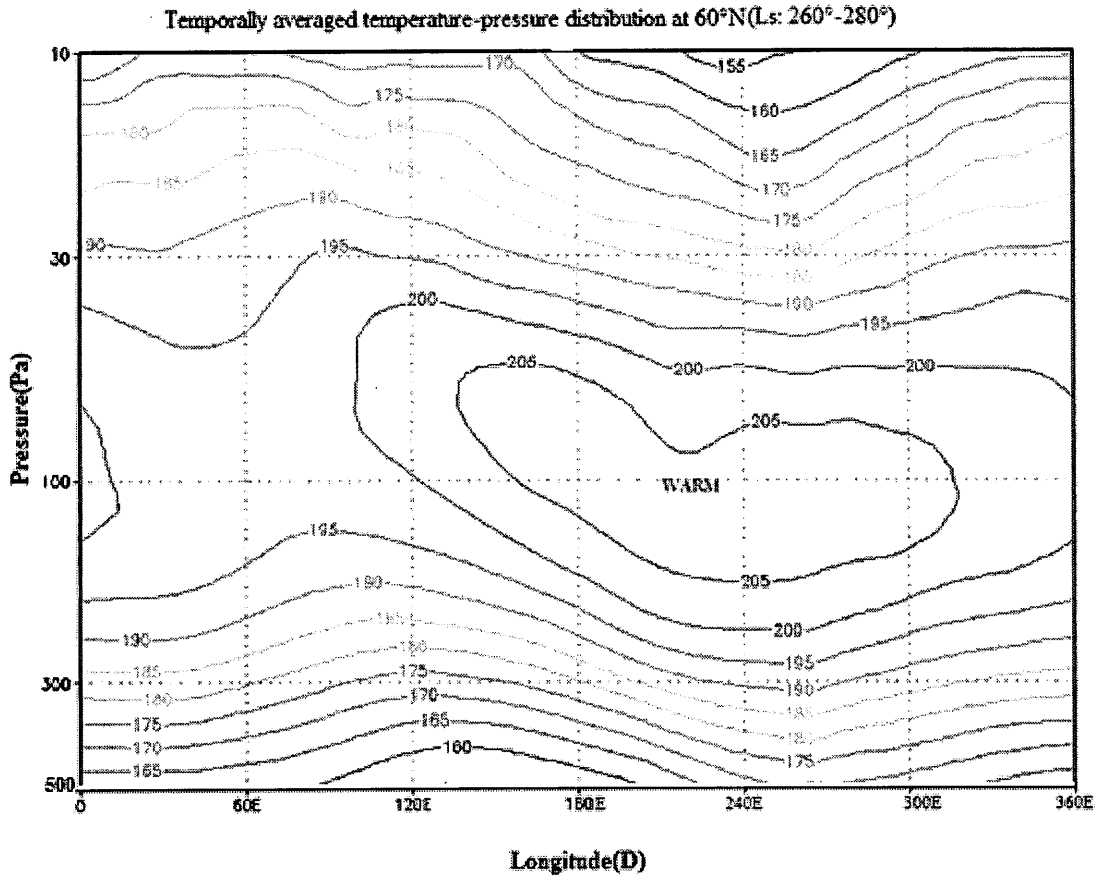

Figure 5.7a: A 2-D temporally averaged temperature-pressure distribution at 60°N in the Ls range 260°-280° (northern late fall-early winter) centred around Ls = 270°.

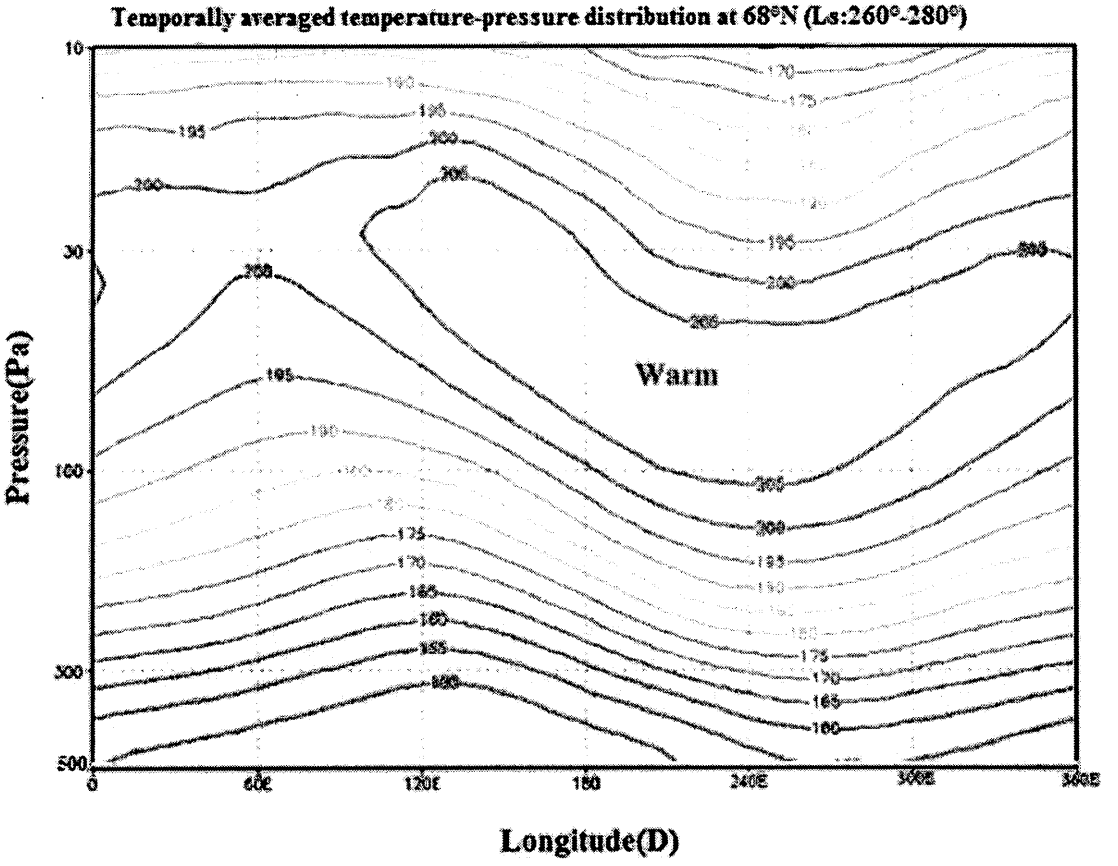

Figure 5.7b: A 2-D temporally averaged temperature-pressure distribution at 68°N in the Ls range 260°-280° (northern late fall-early winter) centred around Ls = 270°.

5.3.5 Model Results (L_S: 350°-10°)

By reversing the zonal wind from easterly to westerly (changing the horizontal temperature gradient pattern) during the fall season in the southern hemisphere again expects to see longitudinal variations in temperature caused by topographical Rossby wave formation in the southern mid-latitudes (Leovy, 2001).

Figures 5.8a and 5.8b show the temporally averaged temperature-pressure distribution in the Ls range 350°-10° (southern late summer-early fall) centred around Ls = 360° at 72°S and 80°S respectively. All three figures illustrate the longitudinal asymmetry of the vertical temperature distribution for southern sub polar regions for this time. In these figures, the warm air around the cryptic region can be seen whereas the temperatures around non-cryptic regions (~0°-30°E and ~310°-360°E) are colder than cryptic region (~60°-210°E). The cause of the longitudinal variation temperature in the Martian southern hemisphere is related to topographical Rossby wave formation during this period of time (e.g. sections 4.2, 4.3 and 5.4).

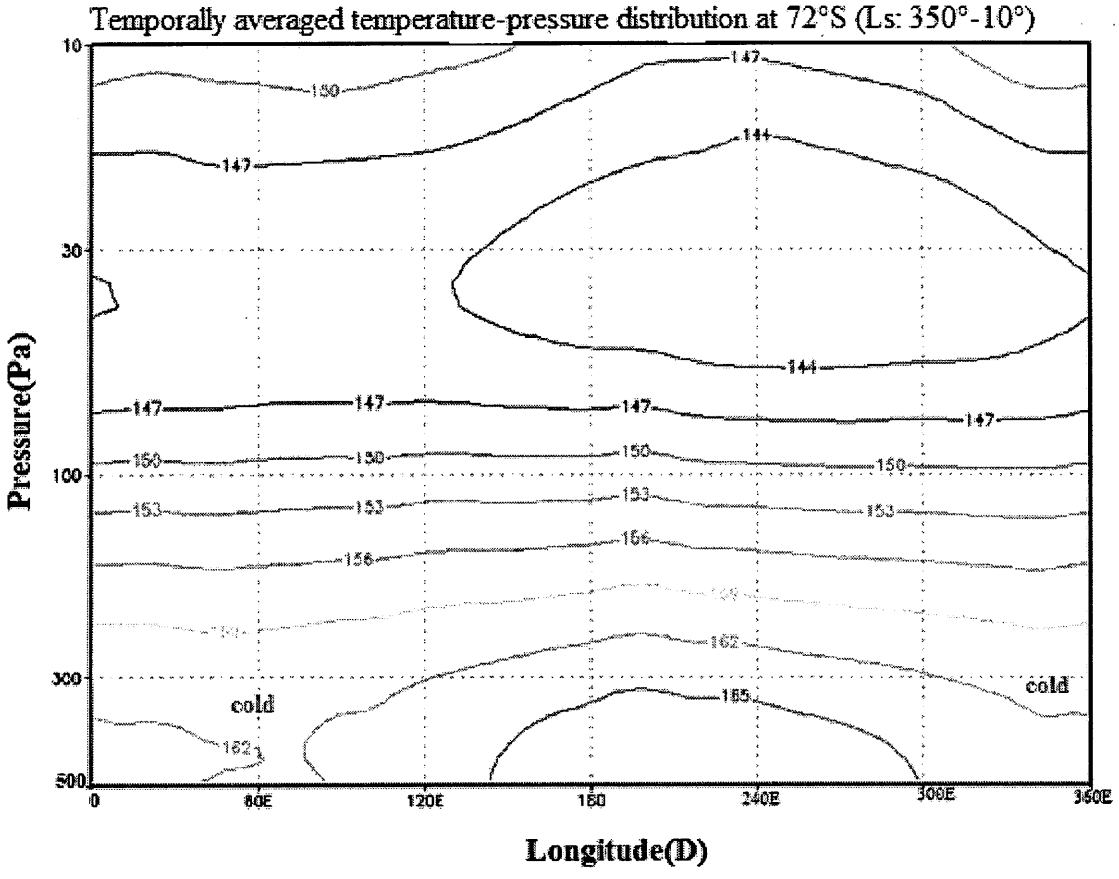

Figure 5.8a: A 2-D temporally averaged temperature-pressure distribution at 72°S in the Ls range 350°-10° (southern late summer-early fall) centred around Ls = 360°.

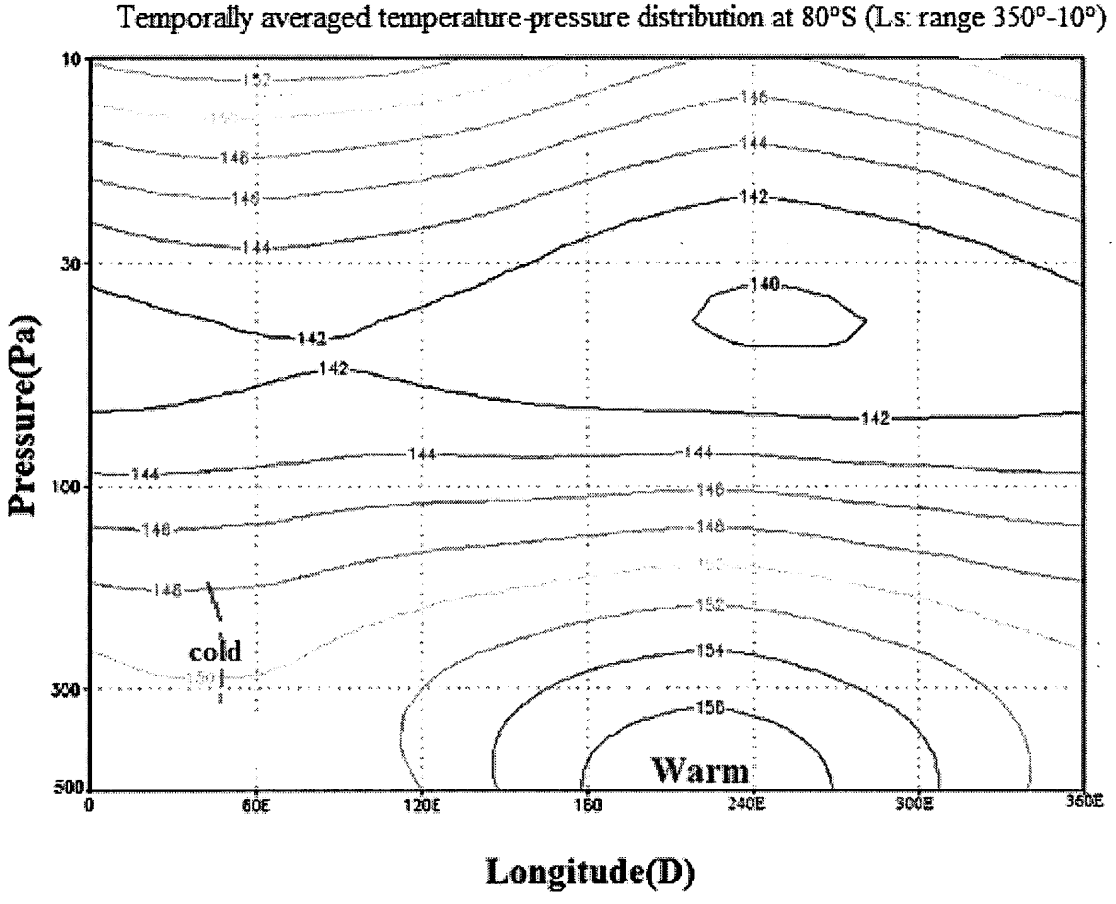

Figure 5.8b: A 2-D temporally averaged temperature-pressure distribution at 80°S in the Ls range 350°-10° (southern late summer-early fall) centred around Ls = 360°.

5.4 Topography Impact on the Martian South Polar Winter Weather

In this section the GM3-v2 dynamical simulation results such as temperature and wind fields (for both realistic and plane topography) showing the effect of topography on local weather patterns in the Martian mid and high latitudes will be discussed. The temperature patterns (time averaged pressure distribution for three sols centred on Ls = 90° for every 15 minutes time step running) and also the wind streamlines patterns (e.g.

sections 3.2.1.1 and 5.5) at Ls = 90° (Martian southern winter solstice) and for both standard model and plane topography will be analyzed.

Figure 5.9a shows temporally averaged temperature-pressure distribution in the three sols around Ls = 90° (southern hemisphere winter) at 64°S. Between 150°E and 240°E (around cryptic region) a warm air tongue has formed whereas cold air columns occur over 80°E-130°E and the area between 250°E and 360°E (around permanent CO_2 ice cap) can be seen. Figure 5.9b shows the temporally averaged temperature-pressure distribution for the same time period when plane topography is used in the model. This figure shows nearly flat and cold temperature distribution at latitude 64°S for different longitudes whereas in the standard model the warm tongue between 150°E and 240°E (around cryptic region) is very remarkable which cannot be seen in the plane topography. The cause of this longitudional variation in temperature (can be seen in the figure 5.9a) is topographical Rossby wave formation in the southern mid-latitudes during southern winter solstice (e.g. sections 4.2, 4.3 and 5.4). Thus the comparison of figures 5.9a and 5.9b confirms that topography has important role in driving longitudinal asymmetry in the temperature-pressure distribution for southern mid and high latitudes (figures for other latitudes are not shown here).

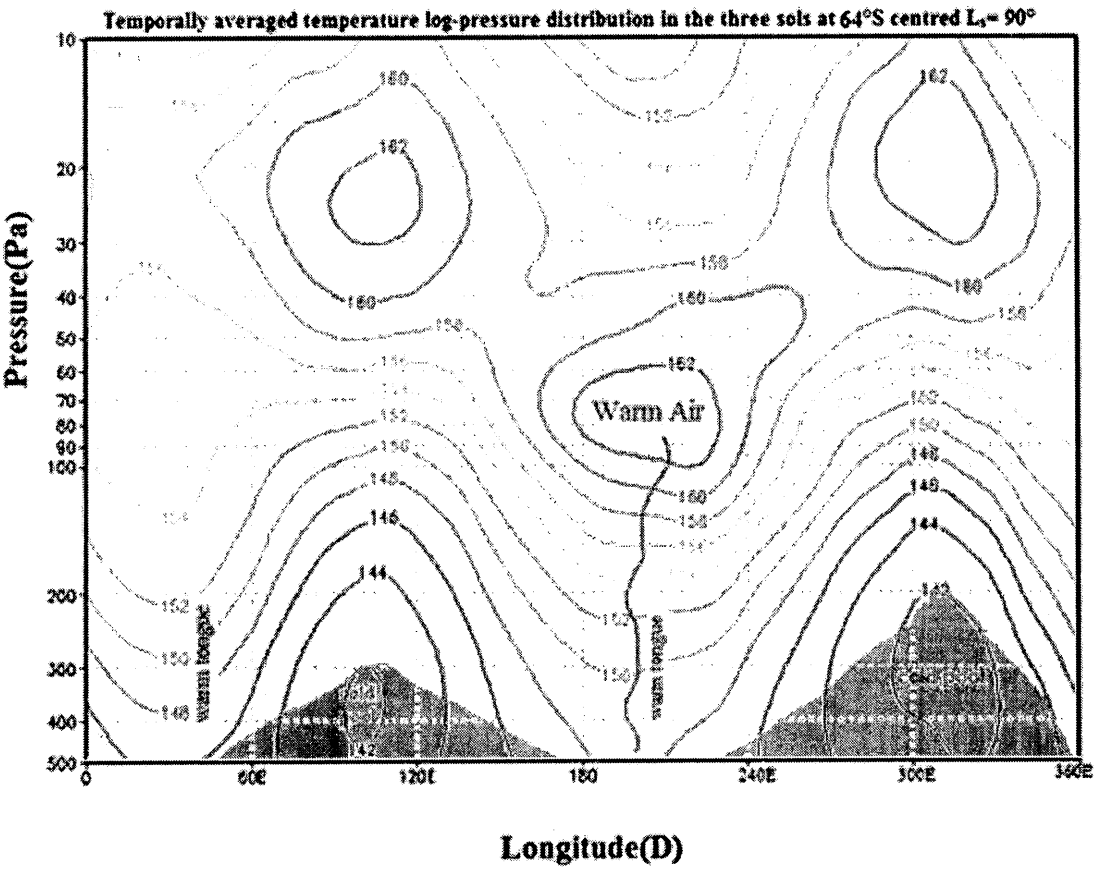

Figure 5.9a: A 2-D temporally averaged temperature-pressure distribution in the three sols around Ls = 90° (southern hemisphere winter) at 64°S (standard model). The approximate area where the temperature is below the condensation point of CO_2 is marked in blue.

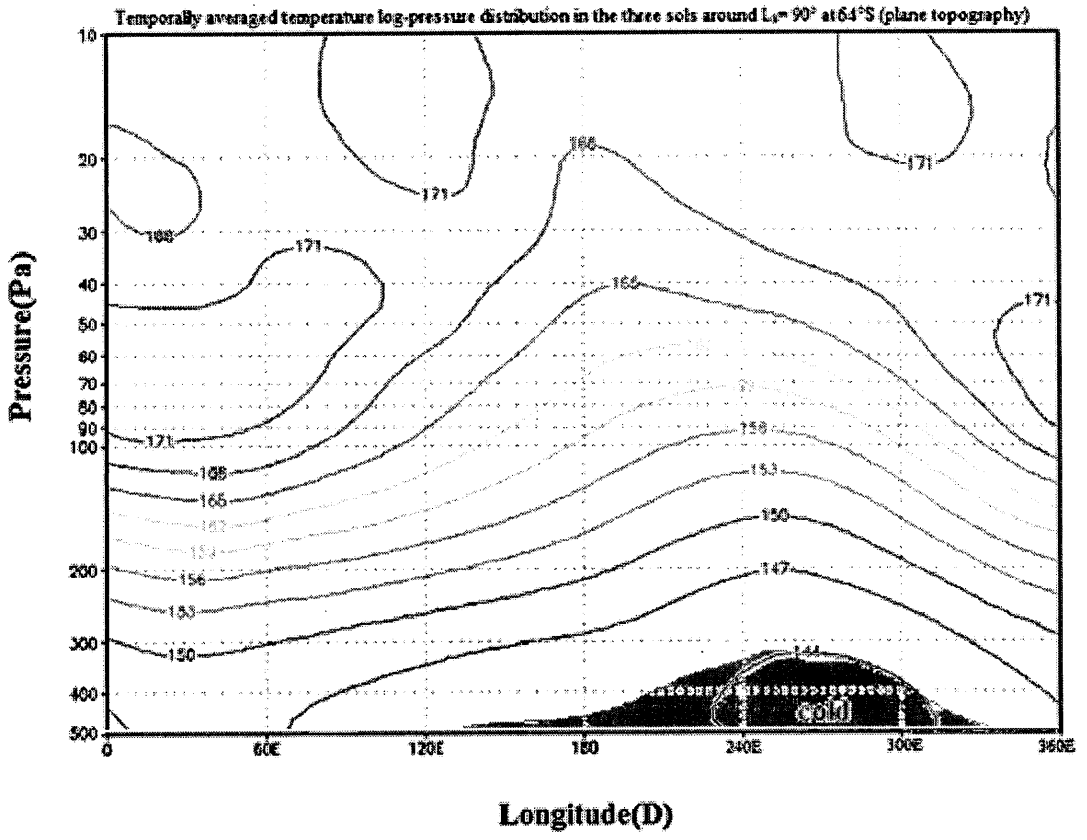

Figure 5.9b: A 2-D temporally averaged temperature-pressure distribution in the three sols around Ls = 90° (southern hemisphere winter) at 64°S (plane topography). The approximate area where the temperature is below the condensation point of CO_2 is marked in blue.

Figure 5.10a shows the horizontal temperature advection (see section 3) averaged over 3 sols centred on Ls = 90° (southern winter solstice) at 460 Pa. Figure 5.10b is the same but for the plane topography. In the standard model simulation, the presence of warm air advection at southern high latitudes mostly around cryptic regions and cold advection at mid-latitudes around the Hellas and Argyre basins is notable compared to that resulting from plane topography. For example, around 60°S, 180E warm advection is

about (0.0001K/s versus 0.00005K/s) nearly twice as strong as that for flat topography and cold advection is four times (-0.0040K/s versus ~ -0.0015-0.0005K/s) stronger in the standard model around the Hellas and Argyre basins. So topography can act to moderate the temperature field in the Martian southern hemisphere weather during wintertime by transporting relatively warmer (colder) air from mid-latitudes (high latitudes) to high latitudes (mid-latitudes) associated by wind pattern structures (see chapter 3).

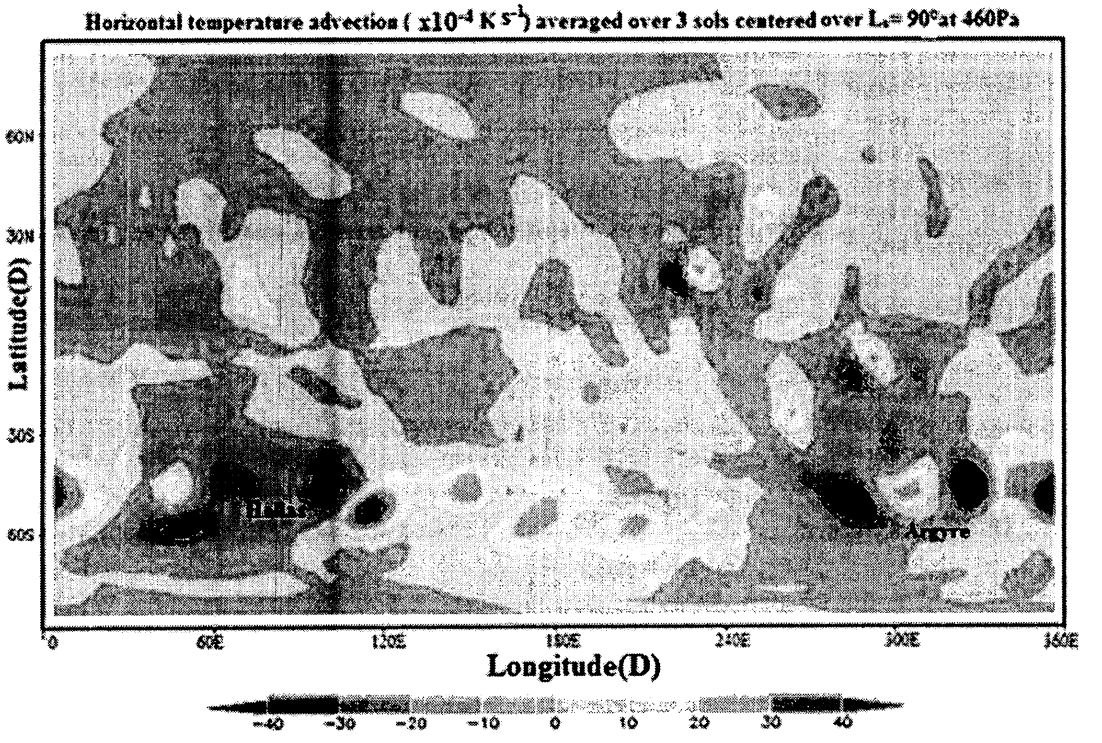

Figure 5.10a: A 2-D map of horizontal thermal advection ($x10^{-4}K\ s^{-1}$) averaged over three sols centred over Ls = 90° at 460 Pa (standard model).

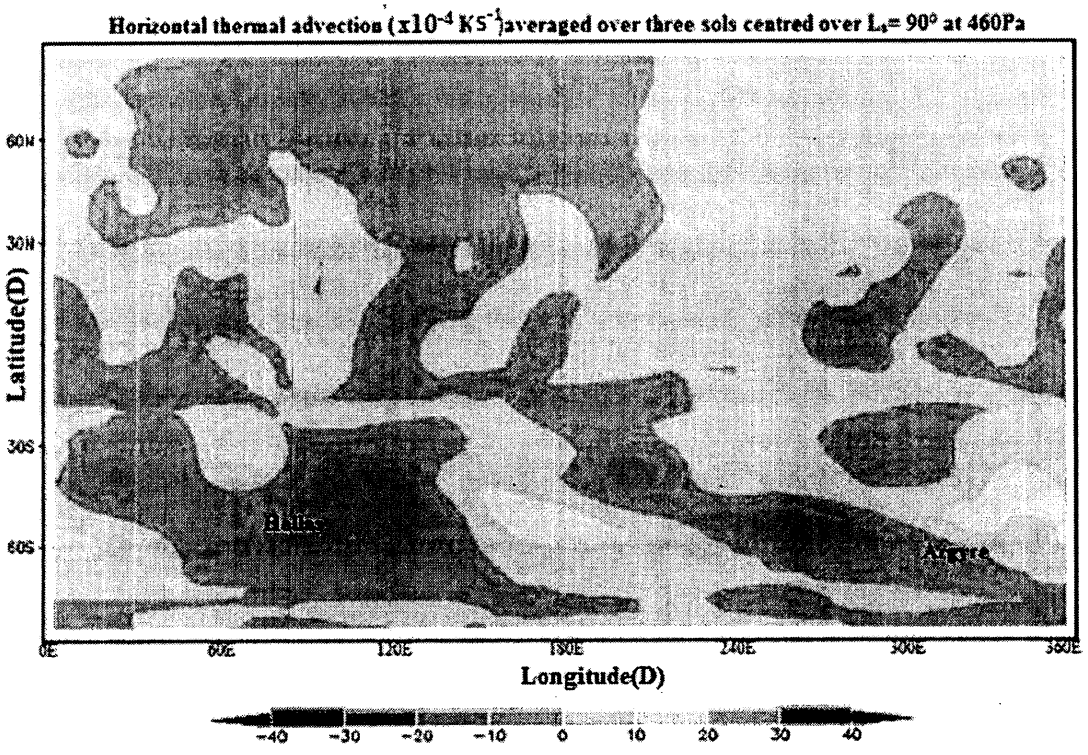

Figure 5.10b: A2-D map of horizontal thermal advection ($x10^{-4}K\ s^{-1}$) averaged over three sols centred over Ls = 90° at 460 Pa (plane topography).

5.5 Weather Patterns during Southern Fall, Winter and Early Spring in the Southern Hemisphere

To better understand the variation of Martian southern hemispheric local weather patterns for different seasons, we use wind streamline analysis is used as a very good method to show the areas of convergence and divergence of the mass flow (see 3.2.1.1). In this section, the wind streamlines from Ls = 20° (early southern fall) to Ls = 200° (early southern spring) have been analysed for every degree of Ls in order to understand the weather patterns during this time period (all of the figures are not presented here but a movie has been prepared for documentation). Wind streamline pattern analysis shows that

around early southern fall (Ls = 22°), a cyclonic trough develops (Figure 5.11a) to the south east of Hellas basin (centred at 42.7°S and 70°E) in the eastern hemisphere. At this time we can see another cyclonic trough system (weaker than eastern one) in the south west of Argyre basin (centred at 49.7°S and 316°E) in the western hemisphere (Figure 5.11a). Also wind streamline pattern analysis shows that around the middle of the southern fall (Ls = 47°), a cyclonic cell develops (Figure 5.11b) to the south east of Hellas basin the eastern hemisphere and after ~30 sols (Ls = 63°) a second cyclonic system develops to the south west of Argyre basin in the western hemisphere (Figure 5.11c). Here it has been shown that there are two cyclonic circulations; one around the Hellas basin in the eastern hemisphere and a second one around the Argyre basin in the western hemisphere. These results confirm what has been reported by Barnes and Tyler, (2007), Forget et al., (1998) and Leovy, (1979). However, between these two cyclonic cells, the pattern is anti-cyclonic (Figure 5.11c). The anti-cyclonic system extends to the cryptic region while the expansion of the cyclonic systems covers the non-cryptic regions. These two different regional weather patterns (cyclonic and anti-cyclonic systems) dominate most of the southern winter. In addition, they (cyclonic and anti-cyclonic systems) have an important impact on the CO_2 vapour deposition during the Martian winter around the pole. A cyclonic system causes cold and unstable or stormy weather (e.g. cloud formation and precipitation[11]) and therefore surface ice accumulation is dominated by snow precipitation (Colaprete et al., 2005) with rather higher albedo (see

[11] Perhaps that precipitation is forced by cooling.

section 5.1.1) while the anti-cyclonic system causes relatively warm and clear air and thus frost accumulation with lower albedo (see section 5.1.1) is dominated by direct CO_2 vapour deposition at the surface. It is the differences between these deposition modes that likely determine the cap albedo (Colaprete et al, 2005). The simulation also shows (Figures 5.11d and 5.11e) that the anti-cyclonic pattern dominates the weather between the two large-scale basins and includes the cryptic region. The eastern cyclonic system around the Hellas basin dominates the seasonal southern sub-polar weather pattern and persists longer than the western cyclonic system. These two cyclones decay around Ls = 145°. Figure 5.11e for Ls = 140° shows that the western cyclone has opened up to form a cyclonic trough, whereas the eastern cyclonic cell has remained. However, wind streamline analysis from Ls = 150° to Ls = 200° shows a gradual weakening of these two cyclonic troughs (Figures 5.11h and 5.11i). Figure 5.11i shows that the cold polar jet has weakened considerably, because of the decreasing latitudinal temperature gradient during late southern spring. This weakening of the winter weather pattern and the beginning of the southern spring weather pattern, which increases the temperature in the polar regions, results in a gradual shrinking of the ice cap (see section 5.1.1).

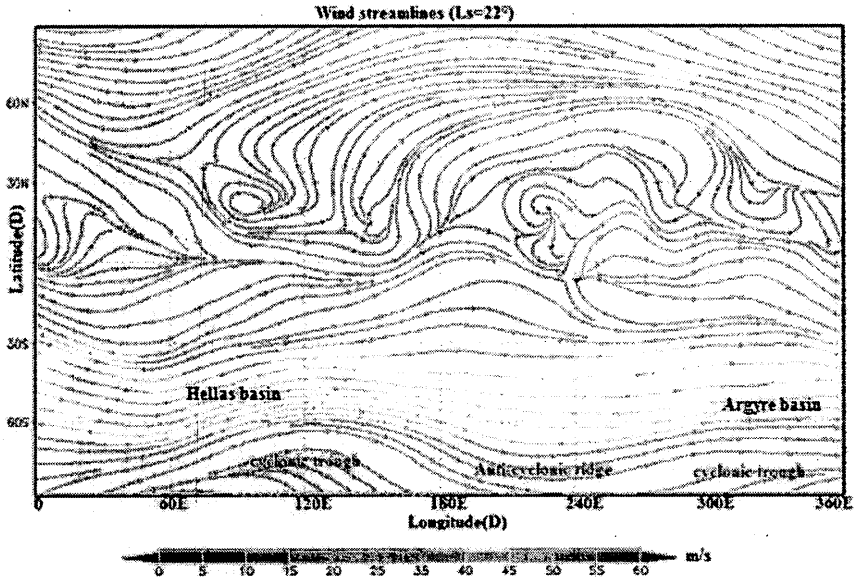

Figure 5.11a: Wind streamline snapshot at 460 Pa (Ls = 22°).

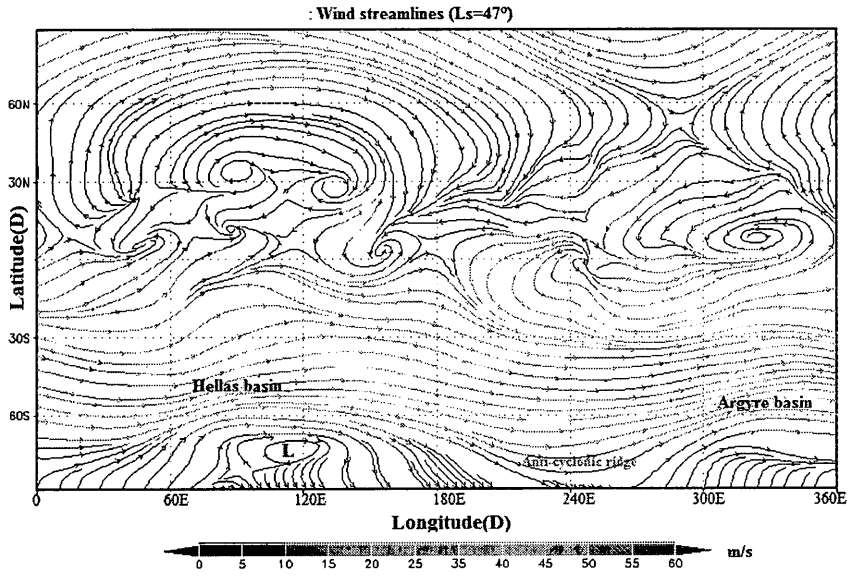

Figure 5.11b: Wind streamline snapshot at 460 Pa (Ls = 47°).

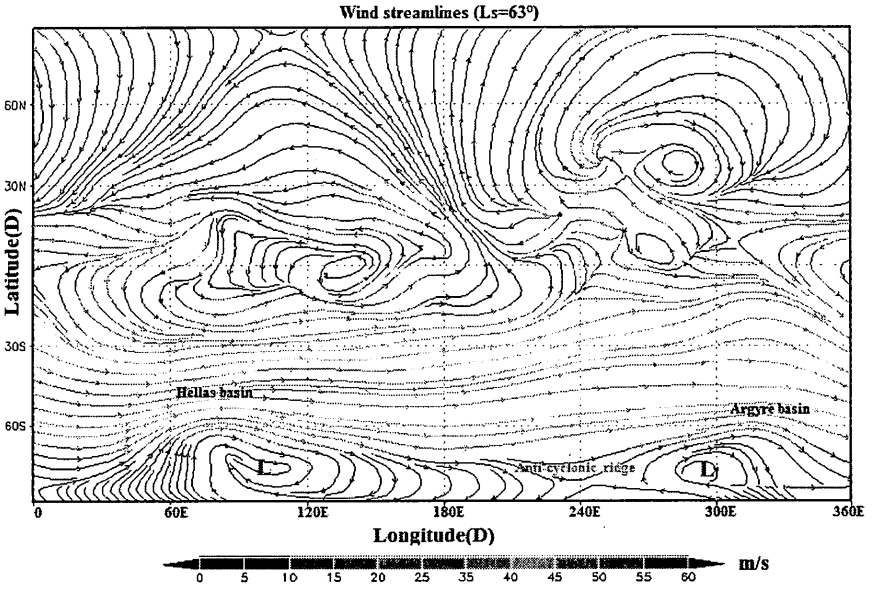

Figure 5.11c: Wind streamline snapshot at 460 Pa (Ls = 63°).

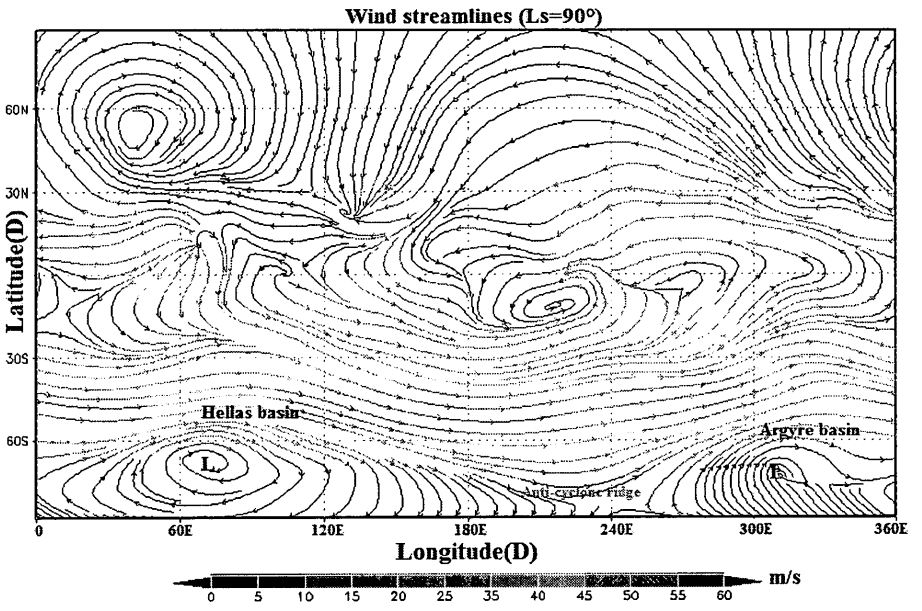

Figure 5.11d: Wind streamline snapshot at 460 Pa (Ls = 90°).

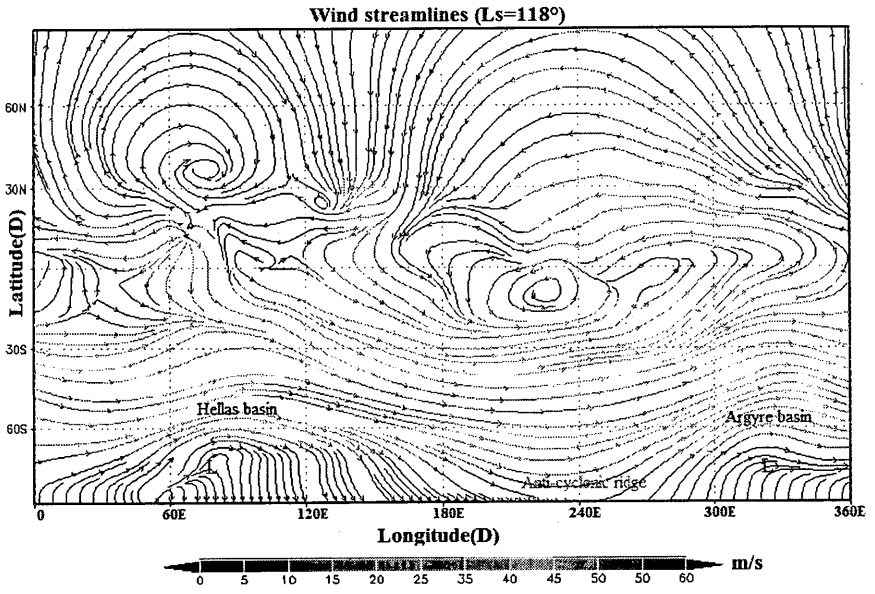

Figure 5.11e: Wind streamline snapshot at 460 Pa (Ls = 118°).

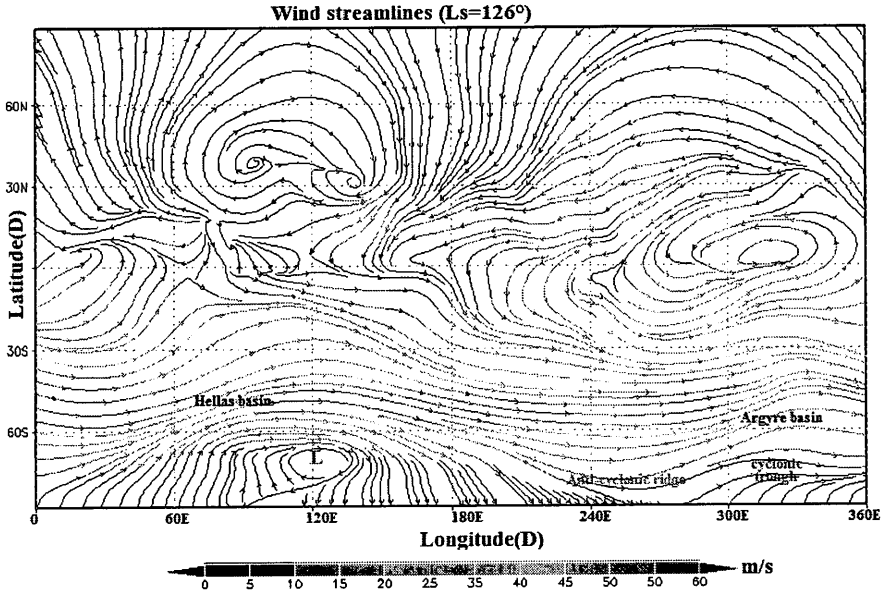

Figure 5.11f: Wind streamline snapshot at 460 Pa (Ls = 126°).

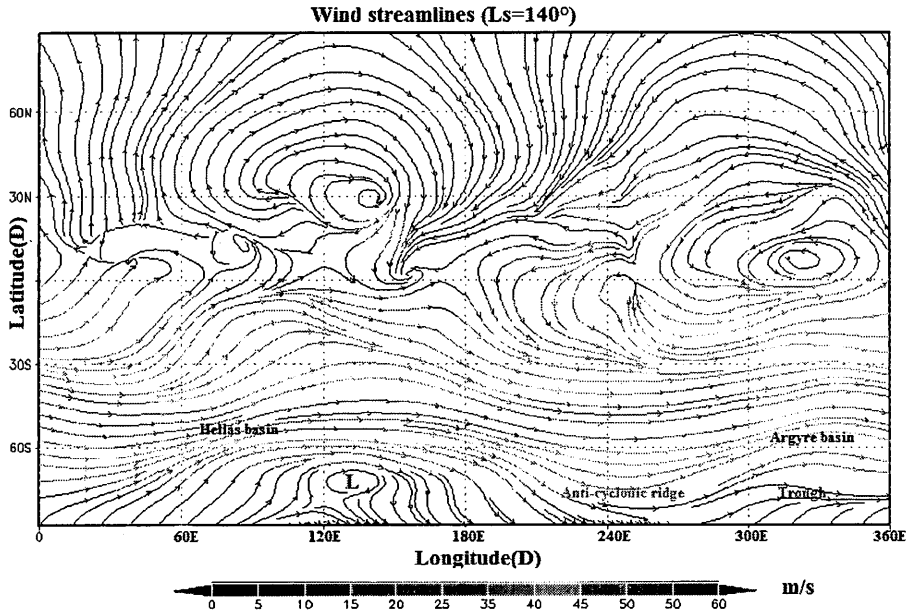

Figure 5.11g: Wind streamline snapshot at 460 Pa (Ls = 140°).

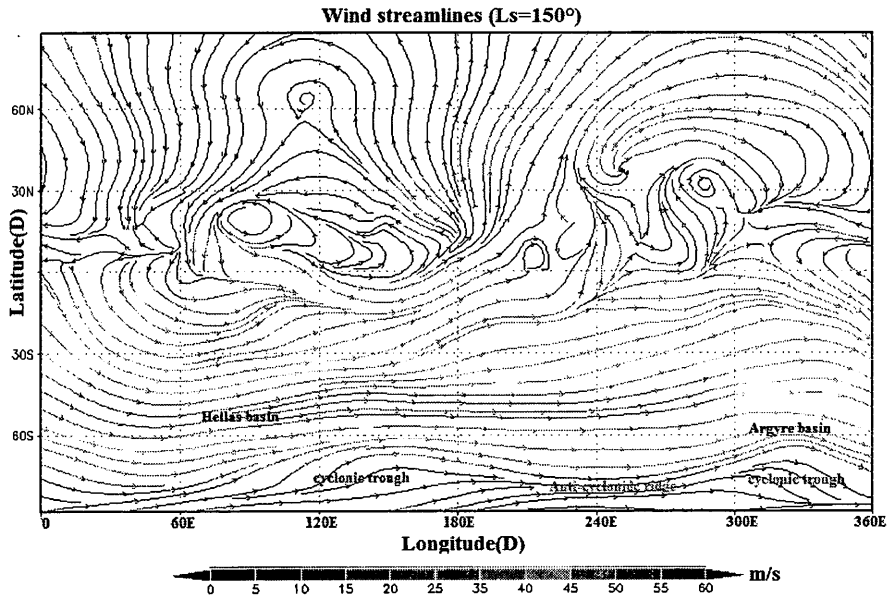

Figure 5.11h: Wind streamline snapshot at 460 Pa (Ls = 150°).

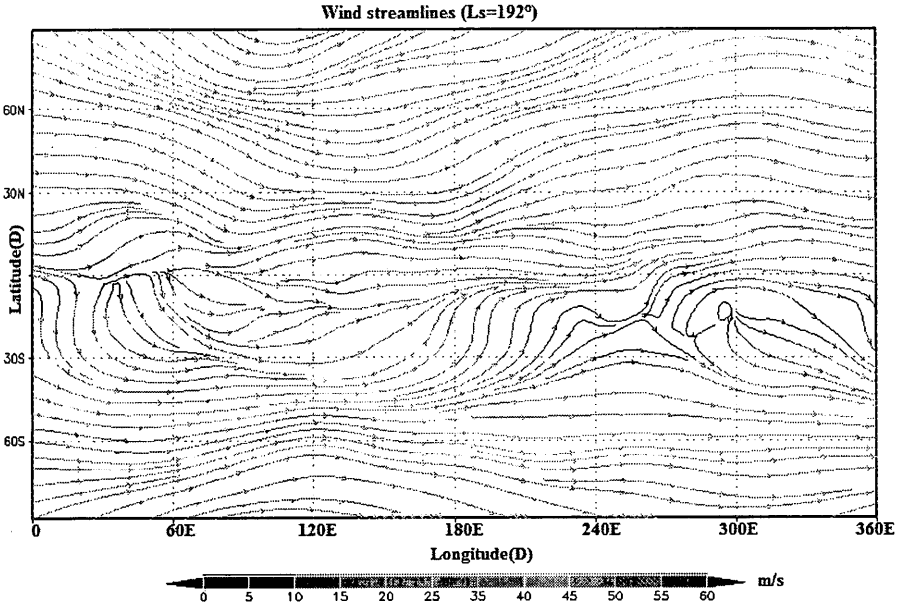

Figure 5.11i: Wind streamline snapshot at 460 Pa (Ls = 192°).

Figure 5.11j shows Martian global condensate clouds Observed by the Mars Global Surveyor Mars Orbiter Camera for the Second Martian Year (Wang, 2004). This Figure confirms the occurrence of the both eastern and western cloud systems during the period of study. These two cloud systems can be controlled by two mentioned cyclonic systems shown by wind streamlines analysis. As we can see in Figure 5.11j, the eastern cloud system around the Hellas basin persists stronger and longer than the western system. This Figure also shows that these two cloud systems get a gradual weakening after Ls = 150° and both of them disappear after Ls = 187° as we showed in wind streamlines study.

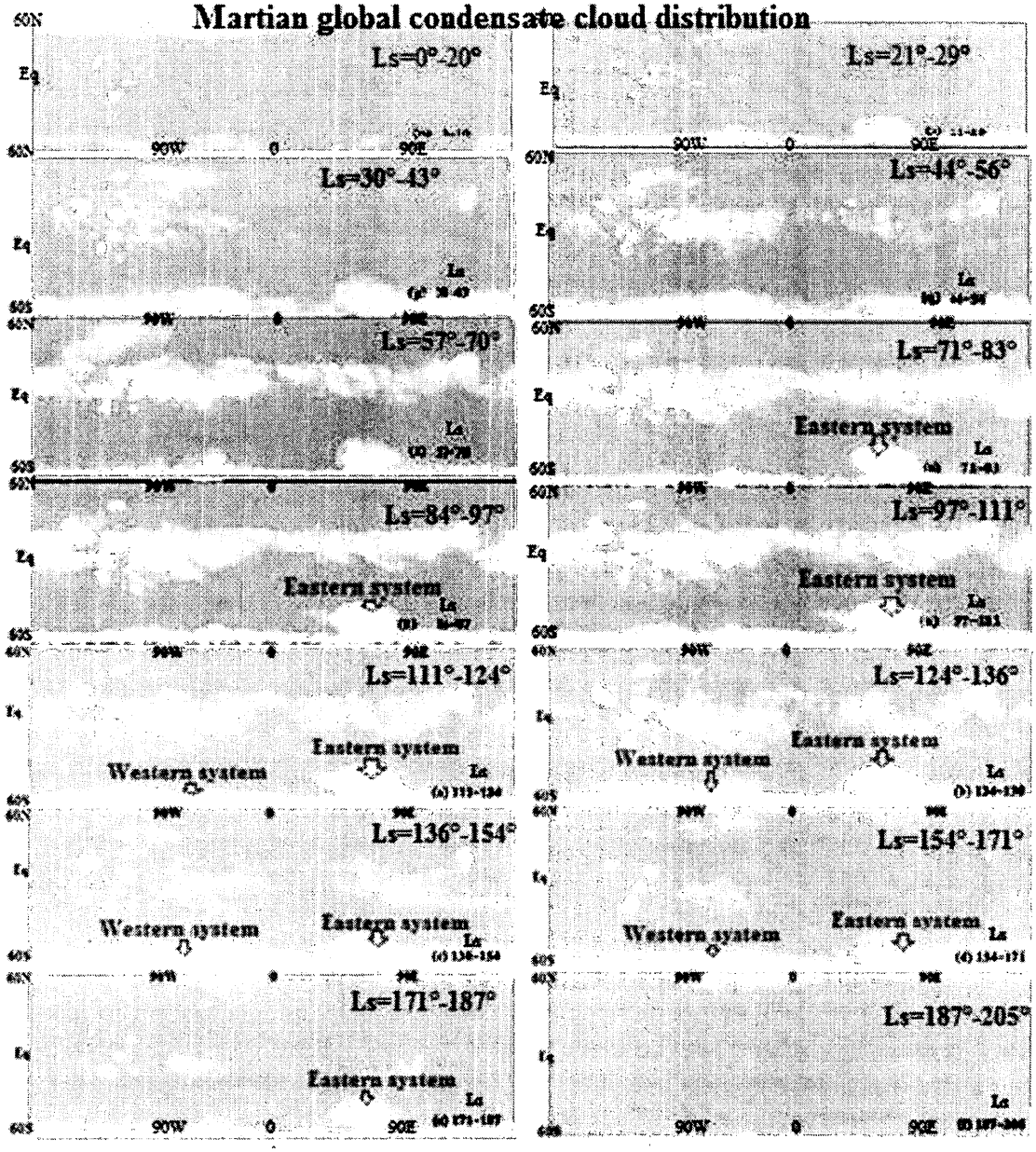

Figure 5.11j: Martian global condensate cloud distribution observed by the Mars Global Surveyor Mars Orbiter Camera for the Second Martian Year in the equatorial maps between 60N-60S (Wang, 2004). The panels are averaged for the accompanying Ls intervals. The Eastern/Western system notes have been added to this figure.

5.5.1 Weather Patterns during Southern Winter with Consideration of the Sensitivity of the Model to Initial Conditions

In order to conduct a more detailed investigation of the differences between GM3 and results from an earlier model which was published by Colaprete et al., (2005), the GM3 has been run with similar assumptions to those made by Colaprete. Specifically the model has been run at a lower resolution of 5°x6° and with the dust optical depth of τ = 0.3. Figure 5.11.1a shows wind streamlines at 400 Pa at Ls = 90. This figure shows a cyclonic system in the southern western hemisphere whereas the eastern hemisphere is controlled with warm anti-cyclonic ridge. A temperature-pressure distribution at Latitude 70 °S has been presented in Figures 5.11.1b. This figure shows a cold trough around 270°E and 80 Pa (in the western hemisphere) and a warm air ridge centred around 60°E and 100 Pa (in the eastern hemisphere). Thus GM3 with similar assumptions shows the same flow pattern as Colaprete et al., (2005). As noted earlier, the standard GM3 (with τ = 0.15) shows two cyclonic systems controlling the Martian southern winter pattern. Between these two cyclonic systems the pattern is anti-cyclonic (Figure 5.11.2a). The vertical structure of the temperature field for the same time and latitude (70°S) shows two cold troughs centred at 70°E below 100 Pa and 270°E below 20Pa.

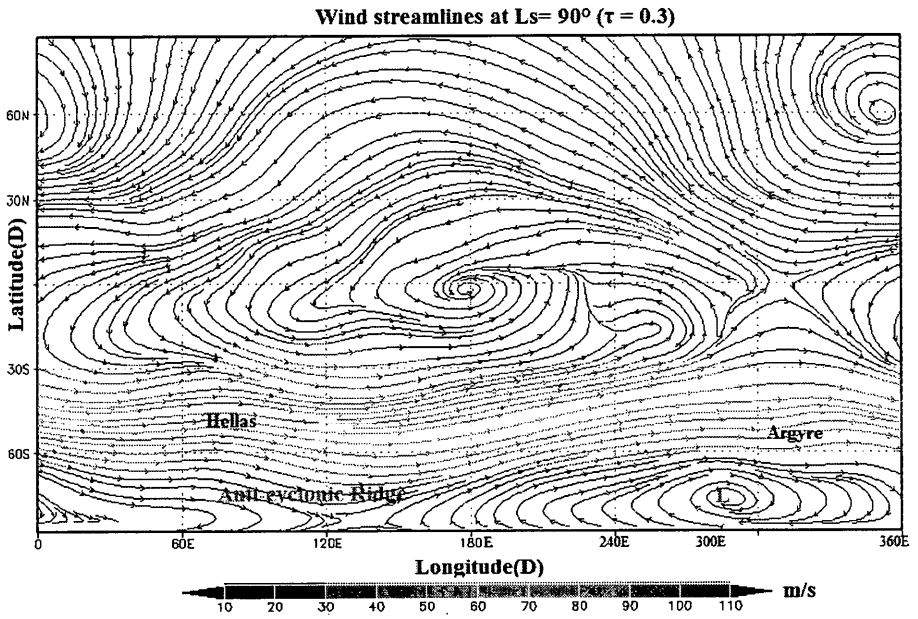

Figure 5.11.1a: Wind streamlines at 400Pa (Ls = 90°, GU 5°x6° and τ = 0.3).

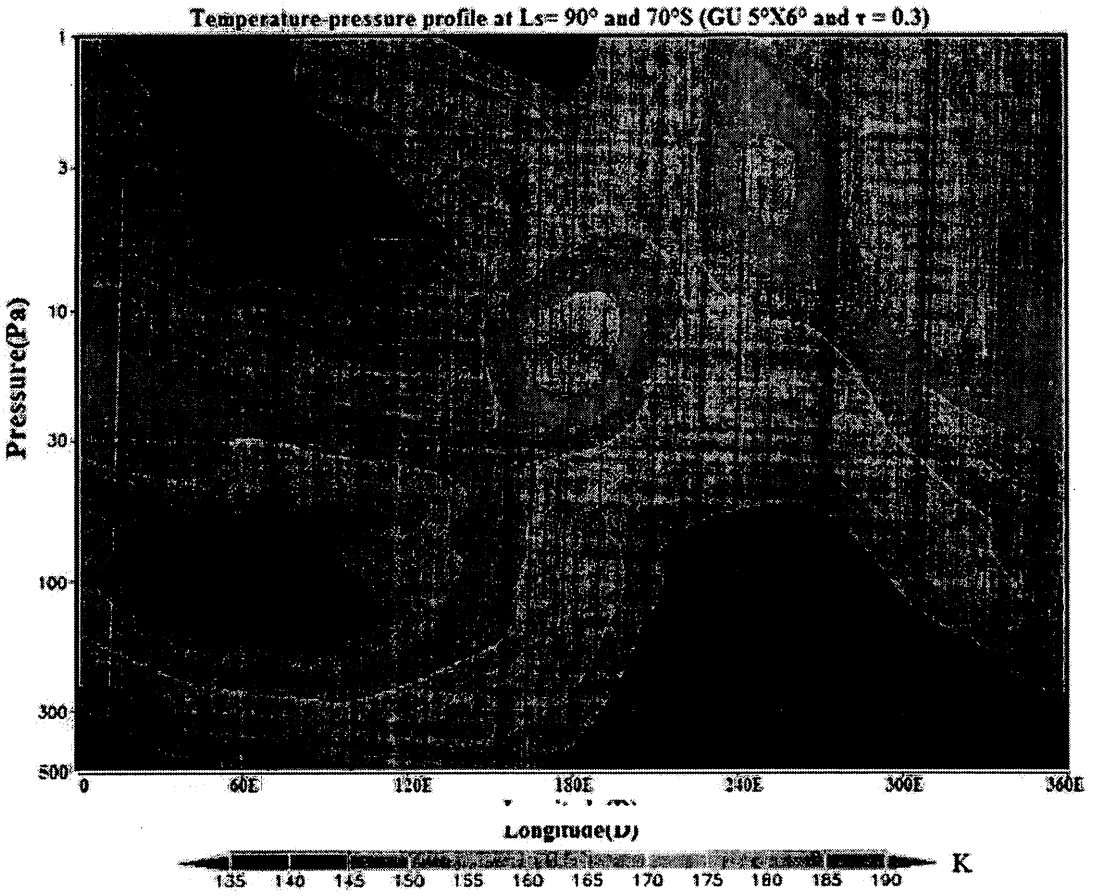

Figures 5.11.1b: A 2-D temperature-pressure profile at Ls = 90° and 70°S (GU 5°X6° and $\tau = 0.3$).

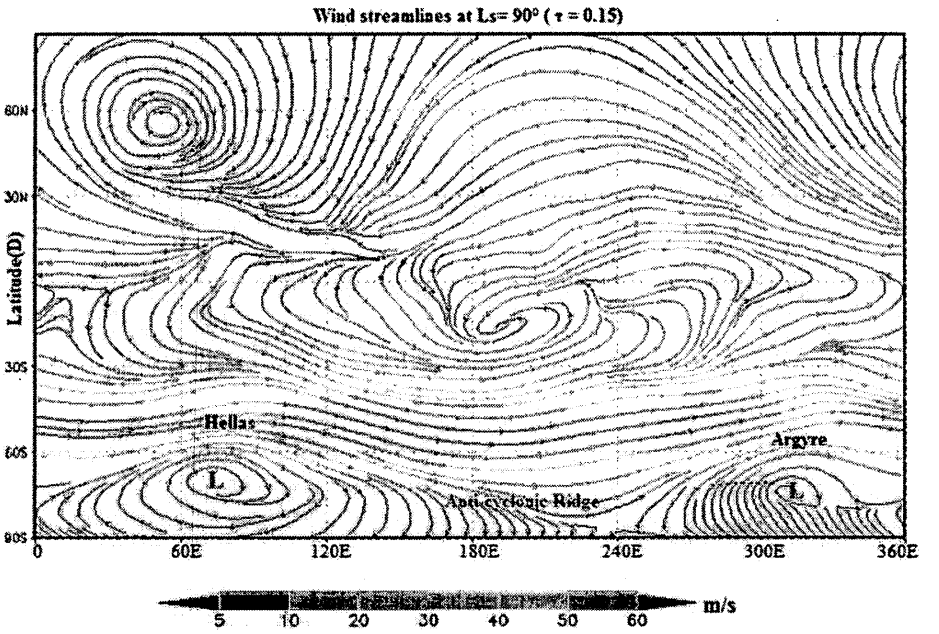

Figure 5.11.2a: Wind streamlines at 400 Pa (Ls = 90°, standard model).

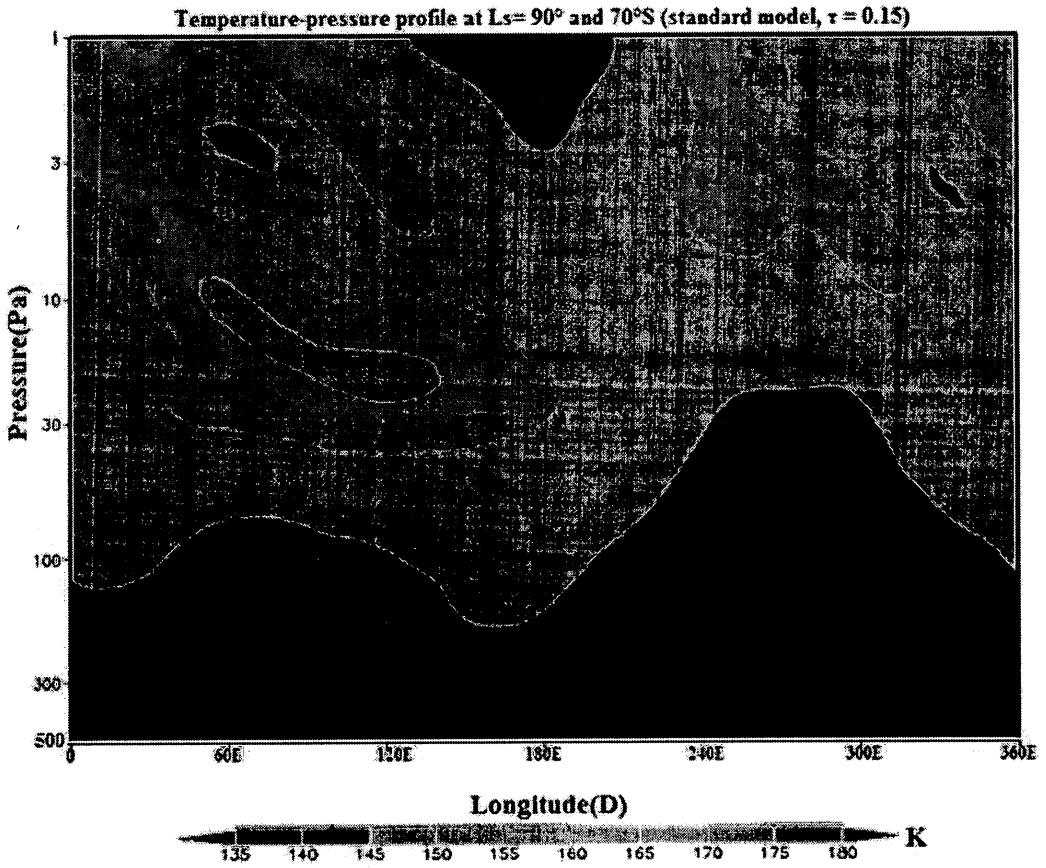

Figures 5.11.2b: A 2-D temperature-pressure profile at Ls = 90° and 70°S (standard model)

It is remarkable that only resolution changing (running at 5°x6° instead of 4°x4°) does not make significant issue. Figures have not shown here. So it is concluded that the model predictions are sensitive to atmospheric dust loading.

The standard GM3 model was run for the second year and the result shows that formation of these two cyclonic systems is a regular winter feature which is expected to occur every year. Figures 5.11.3a and5.11.3b show wind streamlines at 460 Pa around the first southern winter and around the second southern winter respectively.

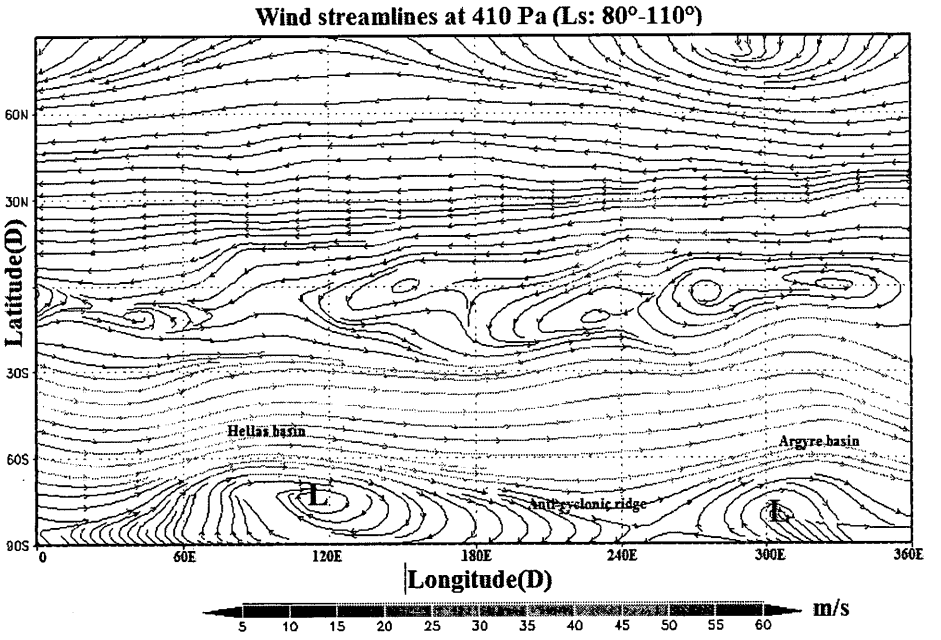

Figure 5.11.3a: Wind streamlines (temporally averaged) at 410 Pa during first winter in the southern hemisphere (Ls = 80°-110°).

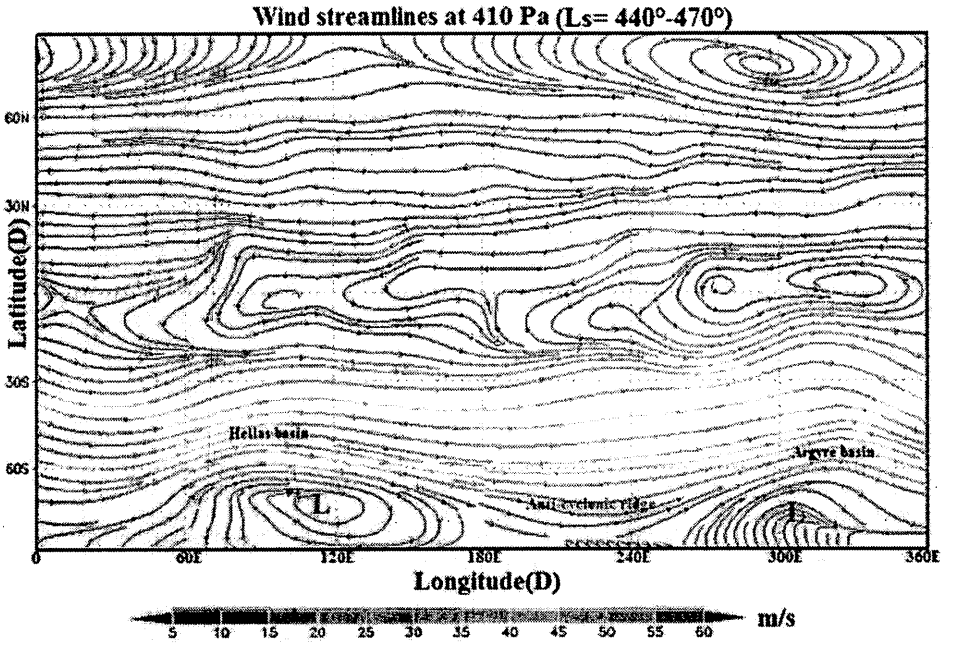

Figure 5.11.3a: Wind streamlines (temporally averaged) at 410Pa during second winter in the southern hemisphere (Ls = 440°- 470°).

5.6 South Polar Cap Albedo Modification in the Global Mars Multiscale Model

As noted earlier, the surface albedo data in the Global Mars Multiscale Model was obtained from the Mars Global Surveyor (MGS) Thermal Emission Spectrometer (TES) visible near-IR data (Christensen et al., 2001), and the thermal inertia map was derived from the MGS TES thermal bolometer data (Putzig and Mellon, 2007). Thus the albedo map which is used in the model represents a mean state of albedo for all seasons of the planet. However, the albedo derived from observations made by the Thermal Emission Spectrometer on board the Mars Global Surveyor (MGS) indicates significant seasonal differences in albedo between cryptic and non-cryptic regions (Colaprete, et al.,

2005). So, to better represent physical processes occurring in polar regions the albedo should be modified to account for seasonal change, driven by the formation of surface ice[12]. The standard GM3 physics code does not consider the difference between cryptic and non-cryptic albedo values and assigns the same values for both cryptic and non-cryptic regions (see Figures 5.12a and 5.12c). Therefore in this work, albedo and thermal inertia values have been modified at the south polar cryptic and non-cryptic areas (see Figures 5.12b and 5.12d). In the standard GM3 version, in the north polar area the albedo (Figures 5.12a and 5.12c) varies between 0.5 (at 84.9°N) to 0.22 (at 71.6°N) while thermal inertia (Figure 5.12a) changes from 400 $Jm^{-2}s^{-0.5}K$ to 300 $Jm^{-2}s^{-0.5}K$. In this work the albedo (Figure 5.12b) for the north cap varies from 0.54[13] (84.9°N) to 0.22 (at 71.6°N) and thermal inertia values are the same as in the standard model (Putzig and Mellon, 2007; Byrne et. al., 2008). A higher value is assigned for the albedo of the non-cryptic regions (240°E and 0°E and 0°E and 30°E) in the southern polar region. These regions are covered with a blanket of CO_2 ice (residual CO_2 ice cap) which does not evaporate even in the southern summer. As discussed in the next section, the temperature of permanent CO_2 ice areas should be fixed at the CO_2 condensation temperature year round because of contact with the atmosphere (see section 5.7). For the cryptic region, which mostly lies between 75°S and 85°S and 50°E and 210°E, lower values (see below) have been considered. In the standard model the albedo for latitudes larger than 83°S

[12] Also this modification will likely be very important in the water cycle simulation of the model.

[13] In this work we have not emphasized on Martian north polar cap albedo, so we have just considered a small increasing changes in albedo values in the modified version rather than standard version.

have the fixed value 0.5 but in the modified version (GM3-M1), the albedo varies from ~0.78 to ~0.3 at non-cryptic regions and ~0.25 to ~0.15 at cryptic regions (Vincendon et al., 2007; Langevin et al., 2007; Byrne et al., 2003; Forget et al., 1998). Also thermal inertia has been modified slightly and varies between 150-50 ($Jm^{-2}s^{-0.5}K$) in non-cryptic regions (Putzig and Mellon, 2007). Here these values are assigned in the physics code and the model was run for nearly one Martian year, starting from initial condition at Ls = 80°.

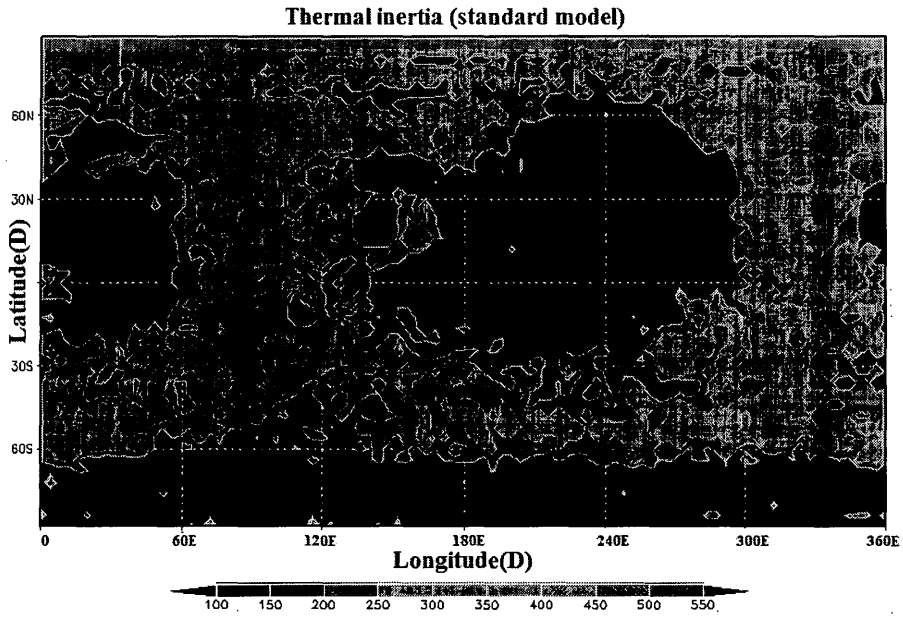

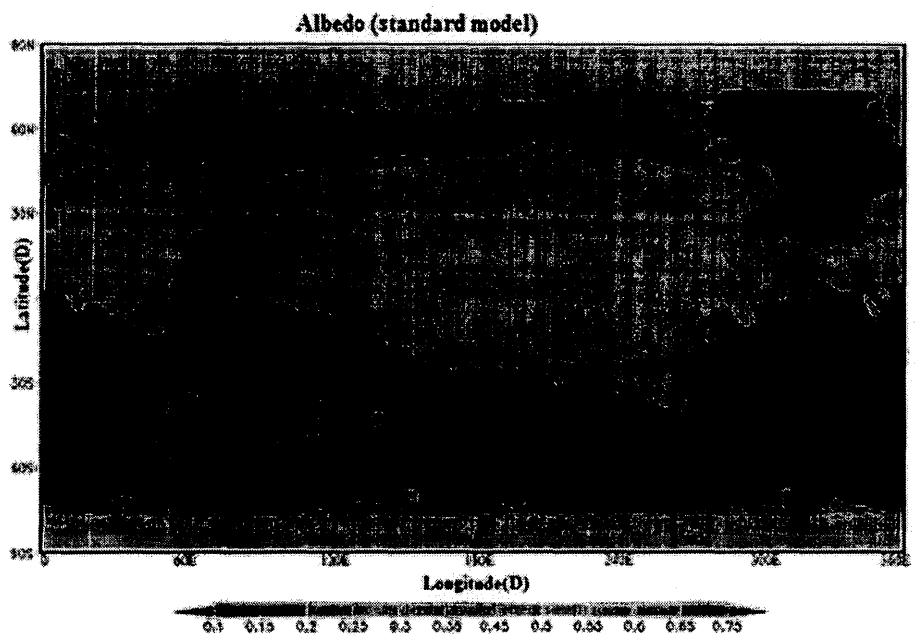

Figure 5.12a: The map of thermal inertia (top) in thermal inertia units (TIU) of $Jm^{-2}K^{-1}S^{-1/2}$ and albedo (bottom) of Mars (standard model).

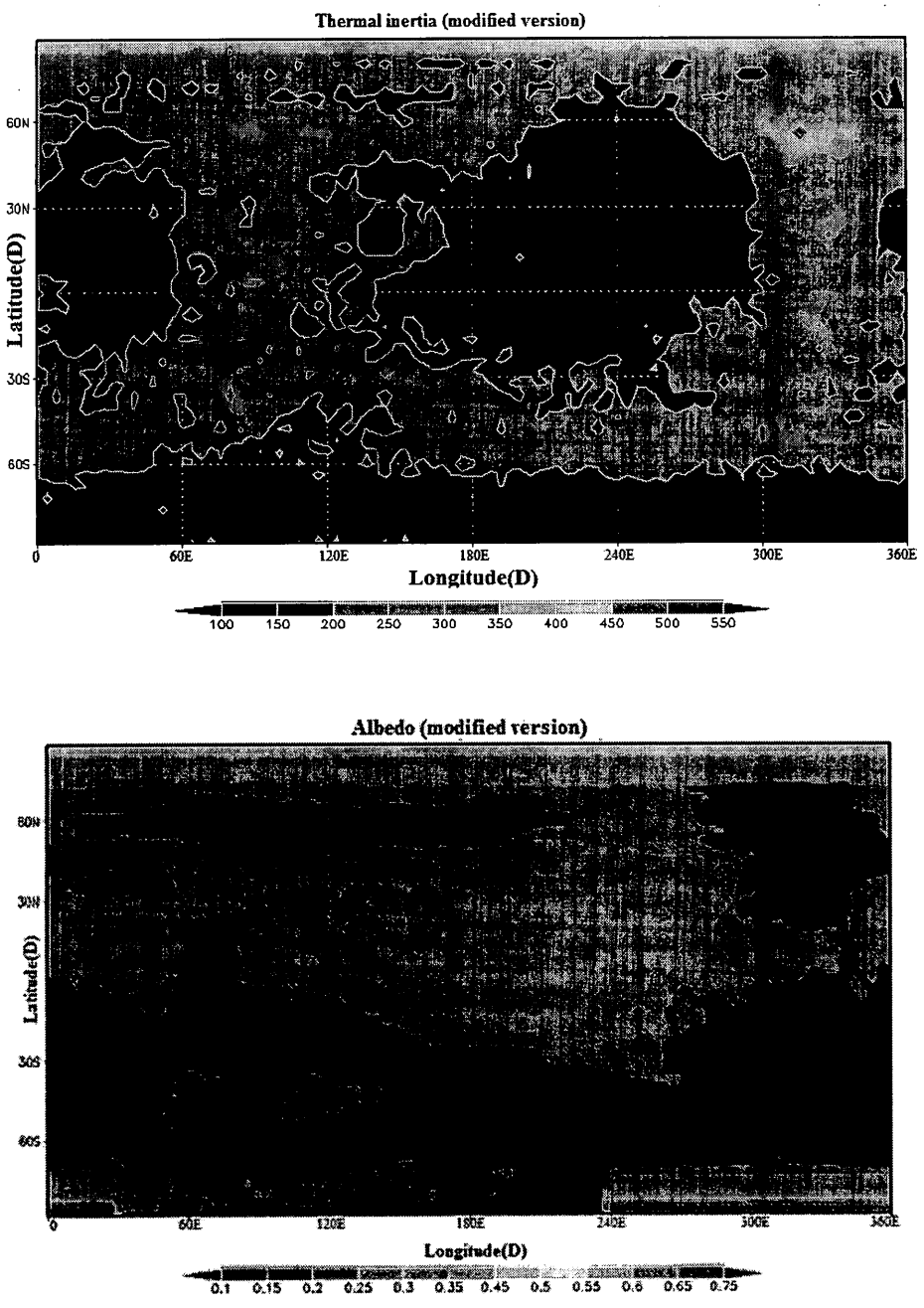

Figure 5.12b:The map of thermal inertia (top) in thermal inertia units (TIU) of $Jm^{-2}K^{-1}S^{-1/2}$ and albedo (bottom) of Mars (modified version).

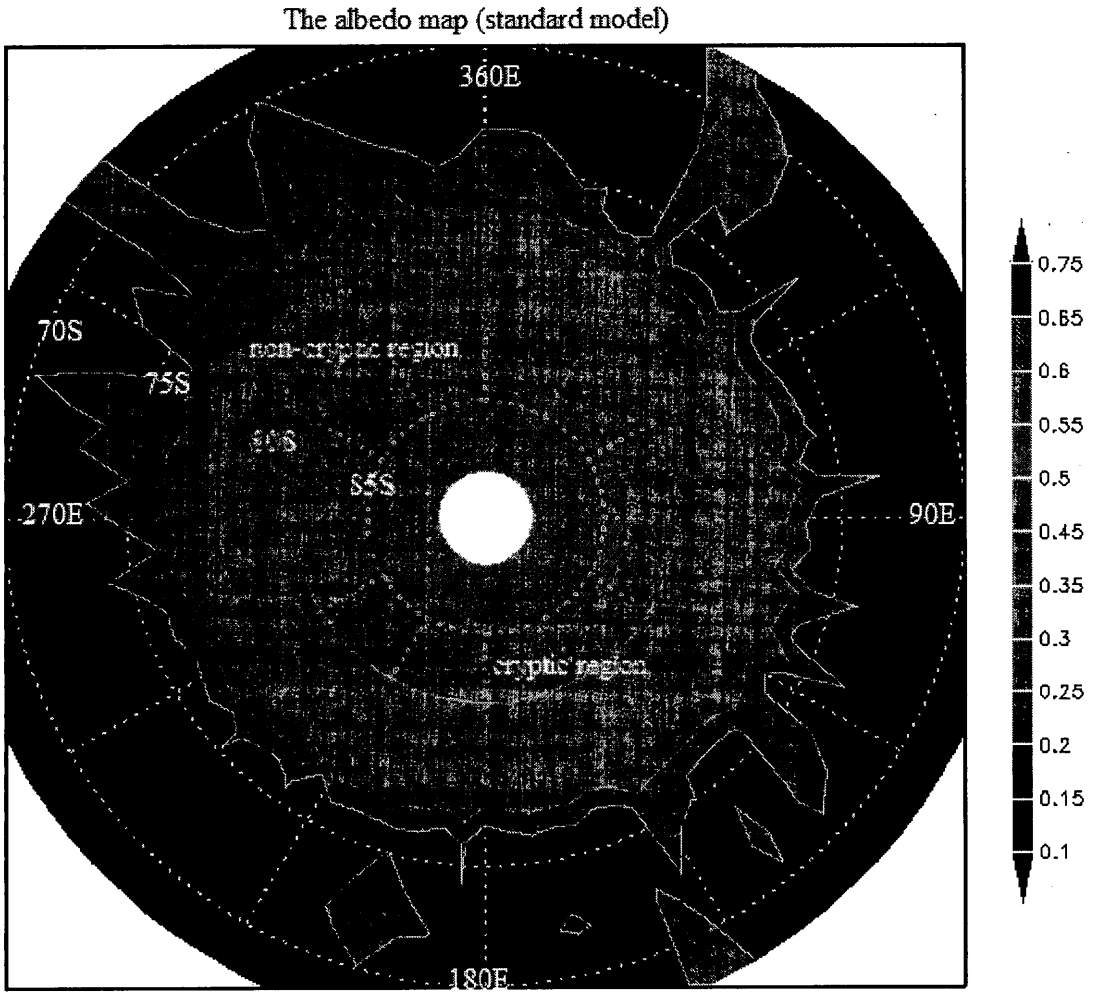

Figure 5.12c: Albedo map of the south polar cap (standard model).

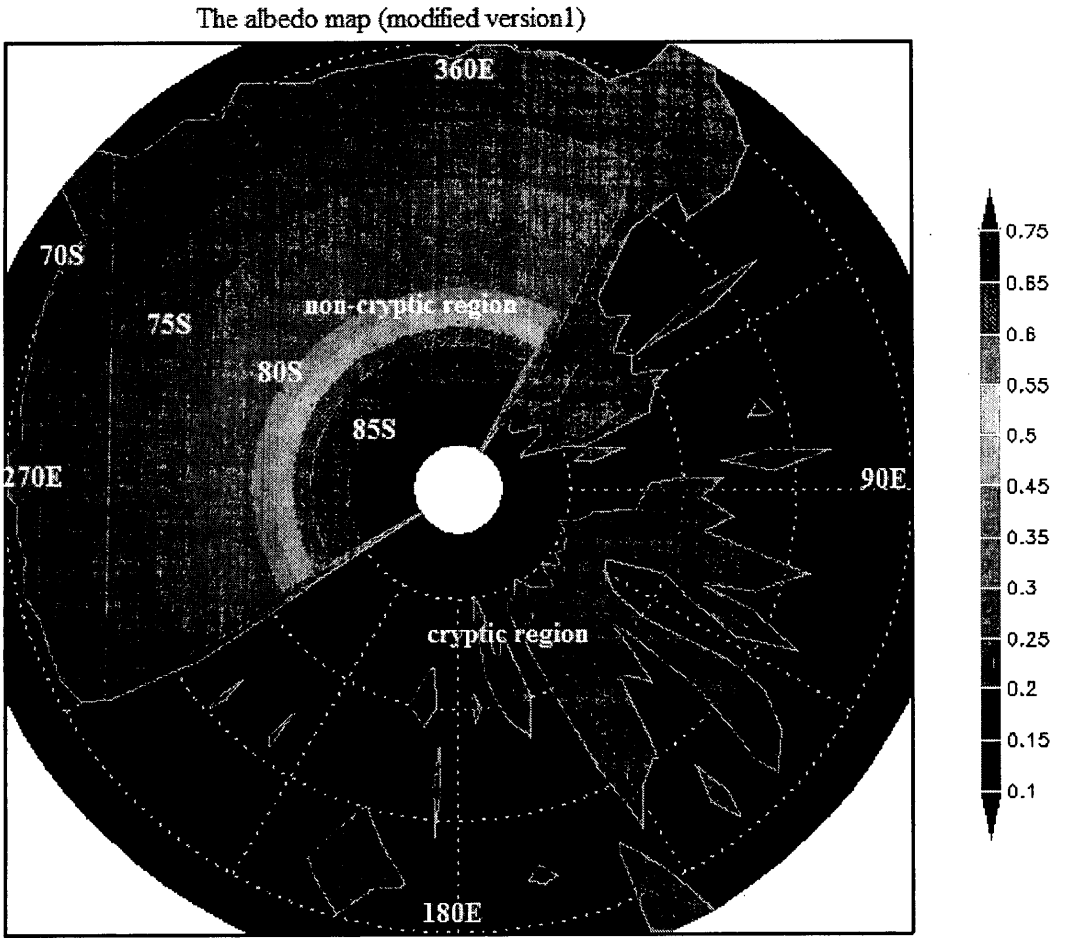

Figure 5.12d: Albedo map of the south polar cap (modified version).

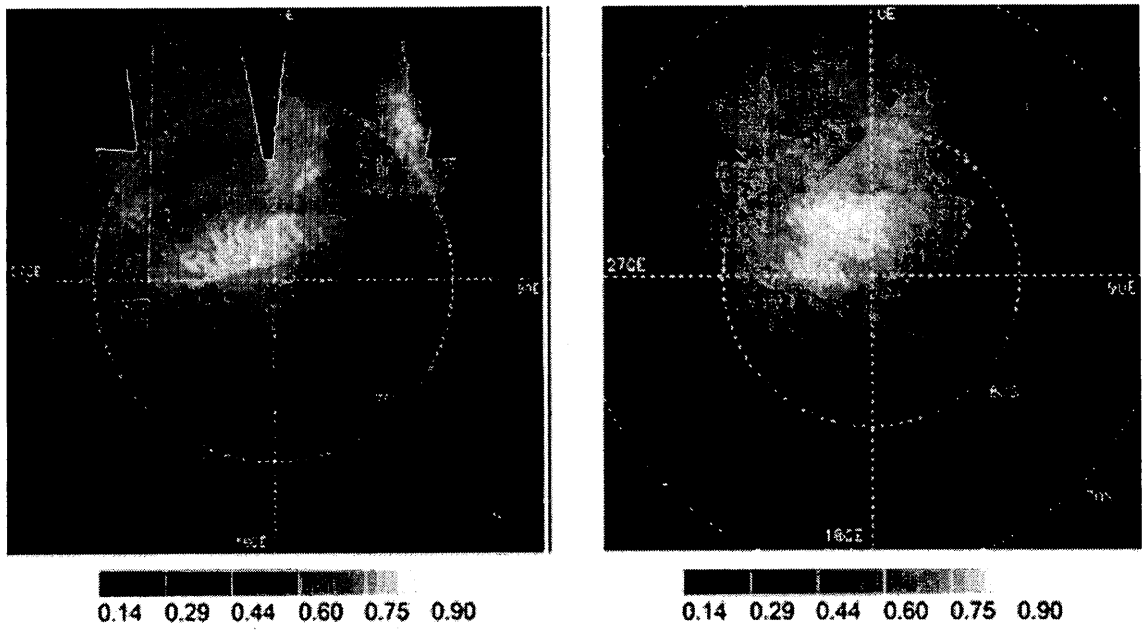

Figure 5.12e: Albedo maps of the south polar cap averaged over Ls = 236.4°–241.9° (left) and Ls = 261.6°-262.7° (right) from observations of the south seasonal cap of Mars during recession in 2004–2006 by the OMEGA visible/near-infrared imaging spectrometer on board Mars Express of Mars (Vincendon et al., 2007).

As discussed earlier, by the beginning of the southern spring, the atmosphere warms up and the seasonal ice cap begins to shrink. The frost zone (cryptic region) with the lower albedo gradually loses its ice. During the southern late spring and the shrinking of the seasonal ice cap, the cryptic region is almost free of ice whereas the non-cryptic region (with higher albedo) would still have ice cover. So, it would be seem that the southern late spring is the best time to investigate the asymmetrical pattern of the southern[14] ice cap (see Figure 5.15c).

[14] The images of Mars' north polar cap (http://www.psi.edu/press/archive/20090914marsco2) were taken by NASA's Hubble Space Telescope (HST) show that the recession of the northern seasonal polar cap from early to late spring follows a symmetrical pattern.

Figure 5.13a shows a snapshot of CO_2 ice mass per square grid point[15] at Ls 237° (between Martian southern spring and summer) in a south polar stereographic map projection for the standard model. Figure 5.13b shows the same time period but with modified albedo and thermal inertia. It can be seen that a large area around the cryptic region between 150°W and 300°W (or between 60°E and 210°E) has less surface ice than Figure 5.13a. Figure 5.13c is a photo mosaic of the south polar cap at Ls = 237° observed by Viking Orbiter 2 during the extended Viking mission. This mosaic is composed of frames taken on orbit 225 (each orbit was completed in 24.66 hours), with a resolution of tens of meters per pixel and shows the south polar cap during the second part (from mid to late spring) of the southern spring (James et al., 1979). As we can see in this image the large areas between 150°W and 300°W (or between 60°E and 210°E) has less surface ice frost as discussed by James et al, (1979). A comparison of the Viking Orbiter 2 mosaic photo (Figure 5.13c) with the standard version (Figure 5.13a) and the modified version (Figure 5.13b) simulations, suggests that the modified version results in a better simulation than the standard version. On the other hand the modified simulation shows less ice mass around the cryptic region, whereas the standard version simulation shows more ice in the cryptic region. Figures 5.13a and 5.13b have shown the snapshots and Figures 5.14a and 5.14b show temporally averaged CO_2 ice mass ($x10^{12}$kg) in the L_s range 230°-260°(~40sols) in the standard model and modified albedo simulation

[15] The data generated by GM3 run for carbon dioxide ice is given in mass (kilograms) per unit area and was not saved on a per square metre. The grid "square" changes shape with latitude on a sphere and decreasing in size near the poles. Ice mass can be calculated in thickness (section 4.3, Mohammed, 2010).

respectively. As for the snapshot version, the time-averaged figure of the standard version shows a connected structure ice pattern at the south cap as opposed to the modified version which shows a very discrete structure and less ice mass around the cryptic region. As has been mentioned before, the south polar ice cap during late spring (Figure 5.13c) has a very asymmetric pattern and is nearly free of ice around the cryptic region. Thus the modified version shows an improved result for surface free ice at the cryptic region during southern hemisphere late spring compared with the standard version.

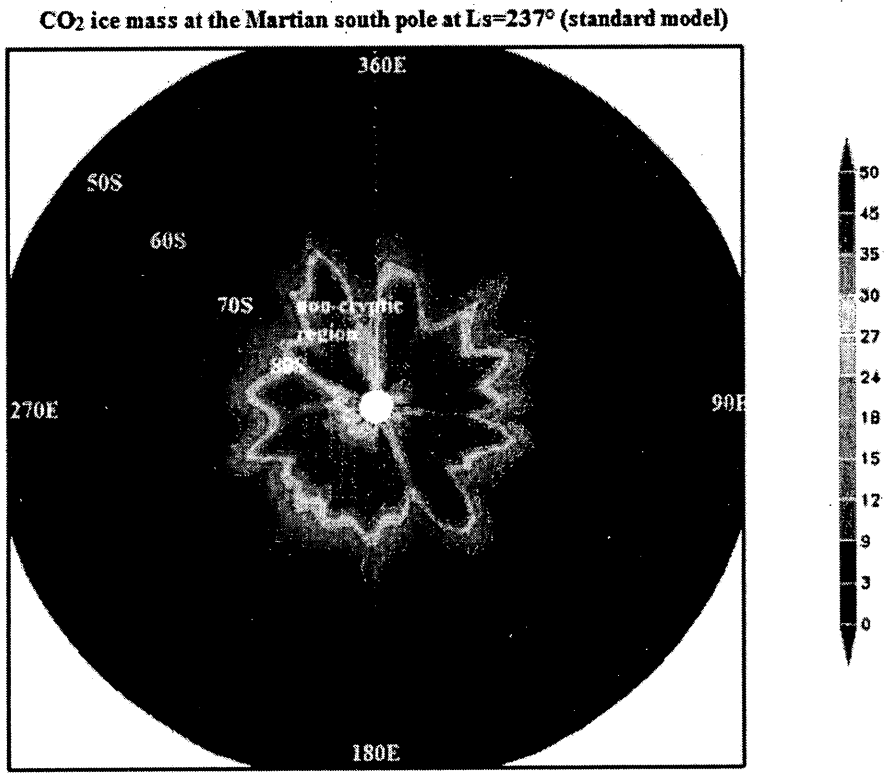

Figure 5.13a: A snapshot for the CO_2 ice mass at the Martian south pole ($x10^{12}$Kg) per square grid point at Ls = 237° (standard model).

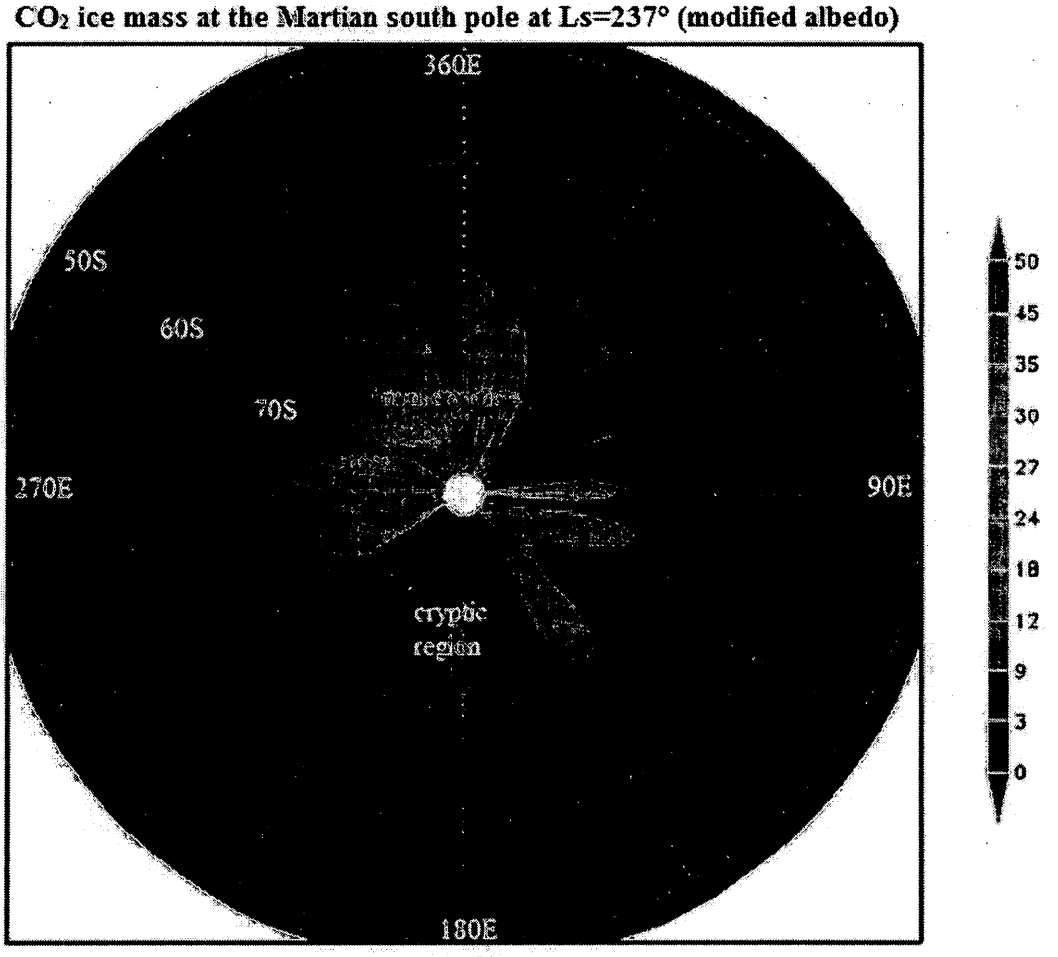

Figure 5.13b: A snapshot for the CO_2 ice mass at the Martian south pole ($x10^{12}$Kg) per square grid point at Ls = 237° (modified albedo).

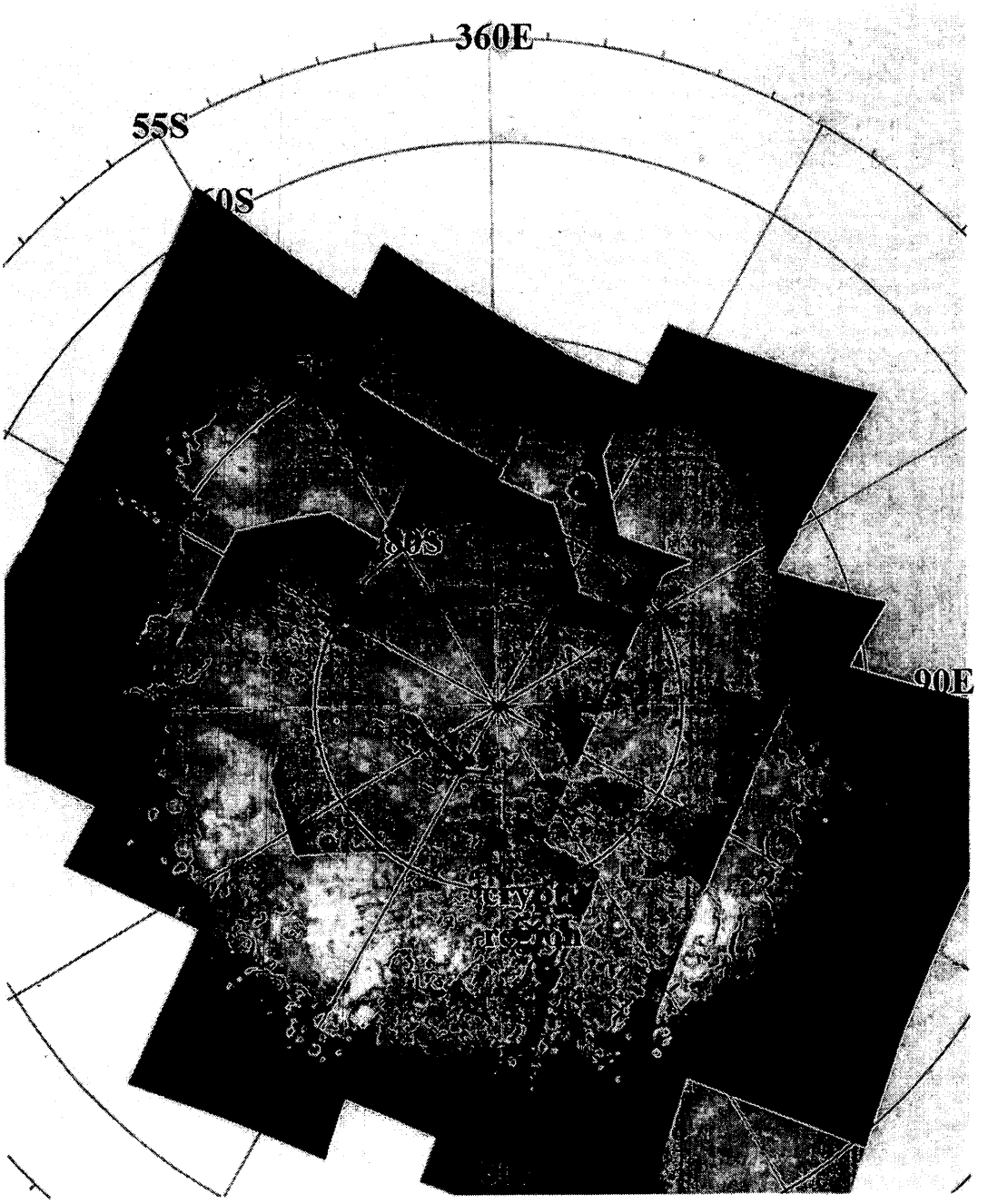

Figure 5.13c: A view of the entire south polar cap, observed by Viking Orbiter2 during the extended Viking mission at Ls = 237° (James et al., 1979).

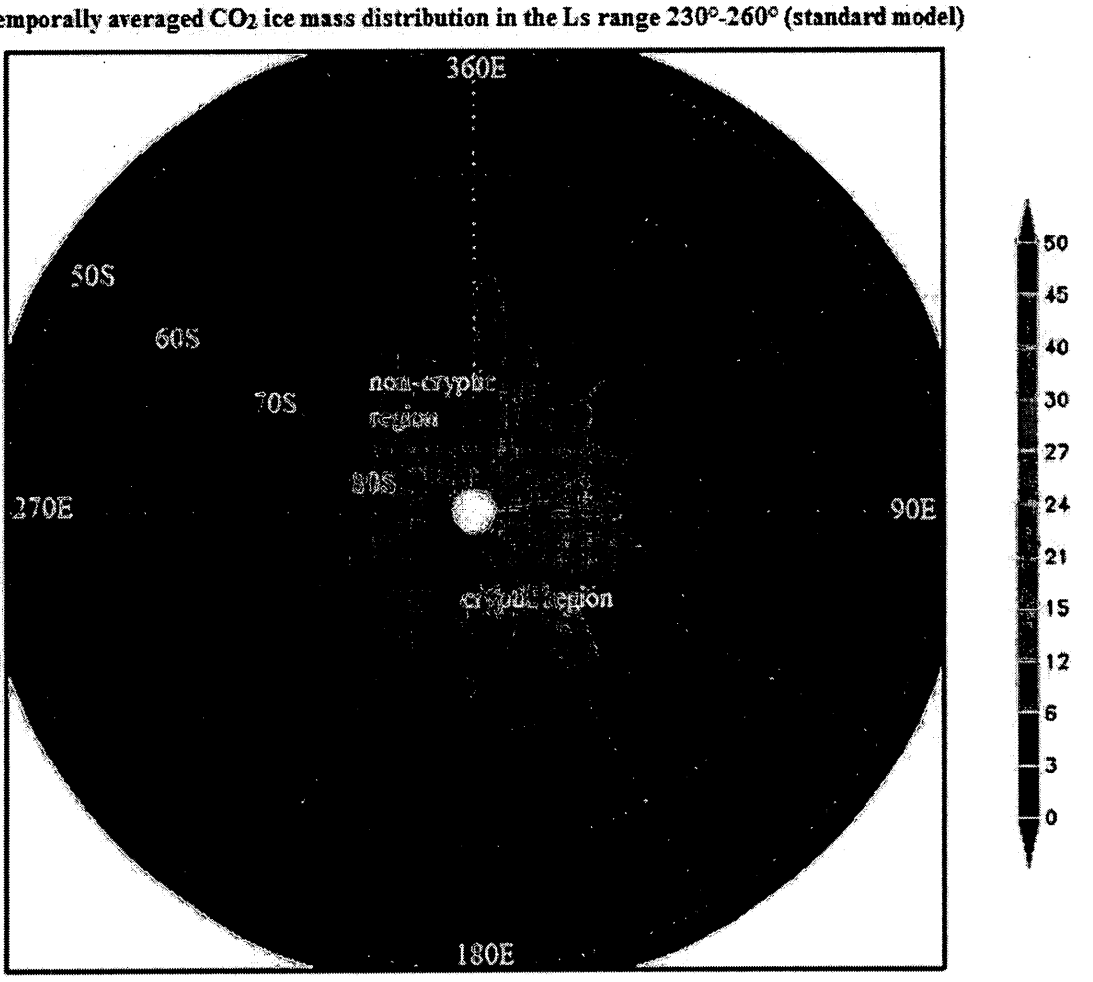

Figure 5.14a: A 2-D temporally averaged CO_2 ice mass distribution ($x10^{12}$kg) per square grid point in the Ls range 230°-260° (standard model).

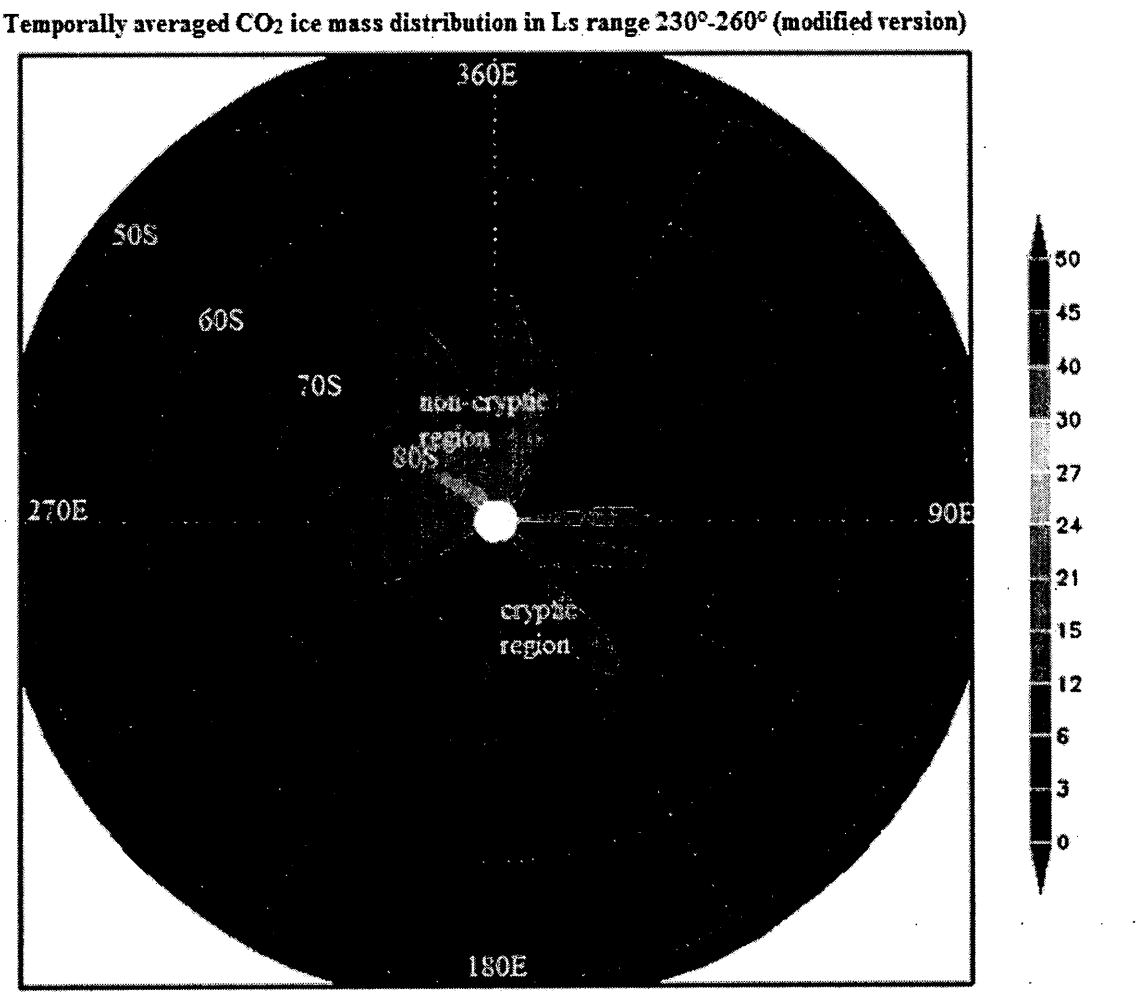

Figure 5.14b: A 2-D temporally averaged CO_2 ice mass distribution ($x10^{12}$kg) per square grid point in the Ls range 230°-260° (modified version).

5.7 South Polar Permanent Cap Simulation in the Global Mars Multiscale Model

After southern summer solstice (Ls = 270°), observations indicate that the south polar cap ice shrinks rapidly and by mid-summer (320°-340° Ls) it remains a relatively small residual ice cap (see section 1.3). In fact, most Mars General Circulation Models are able to fit the atmospheric budget and the seasonal caps reasonably well by tuning the seasonal cap albedos, emissivities, total CO_2 inventory in the system, and the subsurface thermal properties (Forget et al., 1999; Guo et al., 2010; Haberle et al., 2008; Kelly et al., 2006; Pollack et al., 1993). However, the residual CO_2 cap simulation remains more challenging because the simple energy balance models (with time-invariant albedo and emissivity values chosen to fit the Viking Landers pressures) used by all published General Circulation Model results do not predict the residual CO_2 ice cap (Guo et al., 2010). The GM3-v2 simulation also does not produce a permanent south CO_2 ice cap, and the physics code must be modified in order to capture the realistic physical and meteorological processes in the model.

Thus, we have investigated the atmospheric influence caused by the permanent south CO_2 ice cap in the model in order to see if it can significantly improve the representation of south polar meteorology. For example, what is the impact on predicted surface temperatures, surface pressures or cloud occurrence and possible initiation of dust storms in the south polar region during the southern summer period (see sections 5.7.2 and 5.7.3).

In this work, an artificial ice cap has been placed in the southern polar regions with areas closely approximating the location of the permanent CO_2 ice cap. The ice blanket was fixed initially in the physics module close to its observed location (James et al., 1979) and estimated ice thickness (Byrne et al., 2003; Smith et al., 2001; Malin et al., 2001). The artificial south polar residual CO_2 ice cap does not disappear at all times. A higher value of CO_2 ice mass (in Kg per square grid point)[16] at ~87°S has been allocated which decreases slightly with latitude to a minimum value of ice mass at 83°S of ice. This results in an artificial, permanent residual CO_2 cap with average CO_2 ice thickness around 8.6 metres. The southern pole has a permanent residual CO_2 cap, about 8 to 10 metres thick (shown by High Resolution Imaging Science Experiment, or HiRISE, on NASA's Mars Reconnaissance Orbiter[17]), that lies on top of the water ice (Byrne et al., 2003; Smith et al., 2001). So in this work, a blanket of ice was initially located on the surface at the geographical location of the south permanent CO_2 ice (88°S-83°S, 240°E-0°E and 0°E-30°E). The subsequent results use a permanent CO_2 ice cap of fixed size even during southern summer. Indeed, the non-cryptic region is covered with a blanket of CO_2 ice even in southern summer and is not eroded through summer sublimation, in agreement with the observation. Here, the model was run nearly for three Martian years, starting from Ls = 80°. The formation of the seasonal ice cap over the artificial south polar residual CO_2 ice cap during cold seasons is allowed while during the warm seasons

[16] See section 4.3 from Mohammed (2010).

[17] Radar waves which were sent from Mars Reconnaissance Orbiter reflect off surfaces within the ice and travel back to the orbiter. The reflected signals are different depending on the reflective properties of the ice i.e. what materials such as CO_2 ice or water ice and also the thickness (Phillips et al., 2011).

the evaporation from artificial residual ice cap is not allowed to reduce the thickness of the cap below the initial thickness. So the modified model version always has an initial artificial polar residual CO_2 ice cap present.

Figure 5.15a shows a snapshot of CO_2 ice mass per square grid point at Ls = 263° in a south polar stereographic map projection in the standard model. This plot shows nearly free ice cover on south polar cap as expected. Figure 5.15b shows a snapshot of CO_2 ice mass per square grid point at Ls = 263° in south polar stereographic map projection for the modified version. As can be seen in this plot, the permanent CO_2 ice cap is shown for modified version while the area between 50°E and 210°E (the cryptic region) has less ice than non-cryptic regions. Figure 5.15c is a photo mosaic of the south polar cap at Ls = 262.6° (shortly before southern summer solstice) observed by Viking Orbiter2 during the extended Viking mission. It is composed of frames taken on orbit 267 with a medium spatial resolution of the south polar cap in late spring (James et al, 1979). As discussed by James et al. (1979) this figure shows that the area between 150°W (210°E) and 300°W (60°E) has no ice cover. A comparison of Figure 5.15c with results from the modified version of GM3 (Figures 5.15a and 5.15b), confirms that is a reasonable representation of the Mars south polar residual CO_2 ice cap.

About 14 sols later around Ls = 270° the standard model version (Figure 5.16a) does not show the ice cap whereas the modified model (Figure 5.16b) shows the artificial residual south polar cap is still present. Figure 5.16c shows a photo mosaic of the south polar cap at Ls = 274.5° (about 8.3 sols after southern summer solstice) observed by the

Viking Orbiter 2 during the extended Viking mission for orbit 287 (James et al, 1979). It is clear that this modified version simulation is quite similar to the Viking photo mosaic. There is just a slight difference in time (4.5°in Ls or ~8sols) between the modified version simulation (Figure 5.16b) and the photo mosaic (Figure 5.16c). The cap keeps shrinking and by mid-summer (Ls between 320°and 340°) remains as a small residual cap. Figure 5.17a shows the modified model result for the south residual CO_2 ice cap at Ls = 321°.

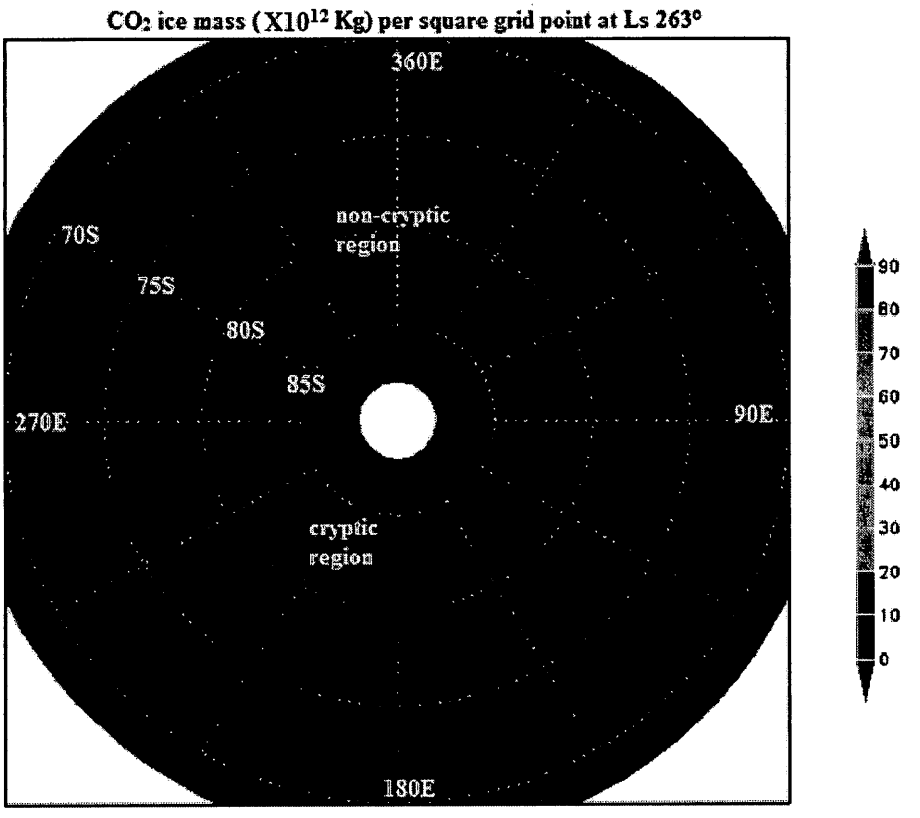

Figure 5.15a: A snapshot of CO_2 ice mass (x10^{12}Kg) per square grid point at Ls 263° (standard model).

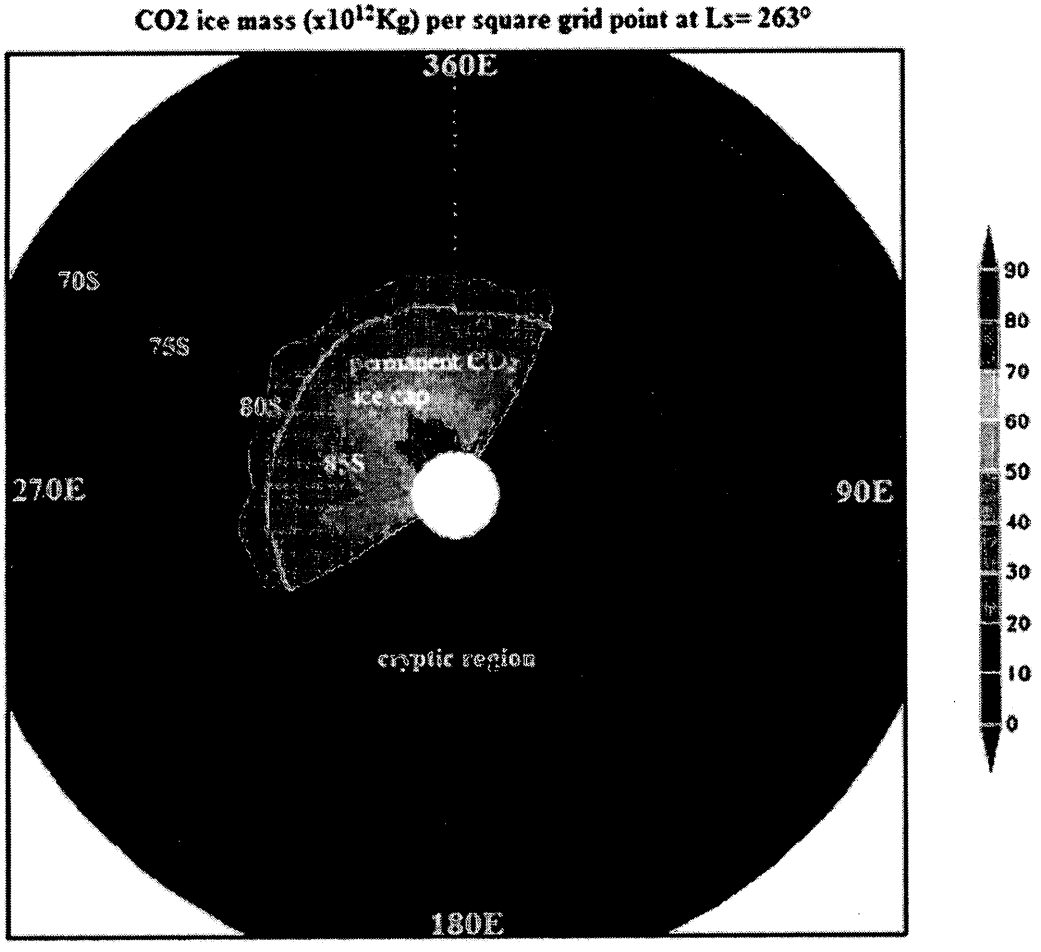

Figure 5.15b: A snapshot of CO2 ice mass (x10^{12}Kg) per square grid point at Ls = 263° (modified version).

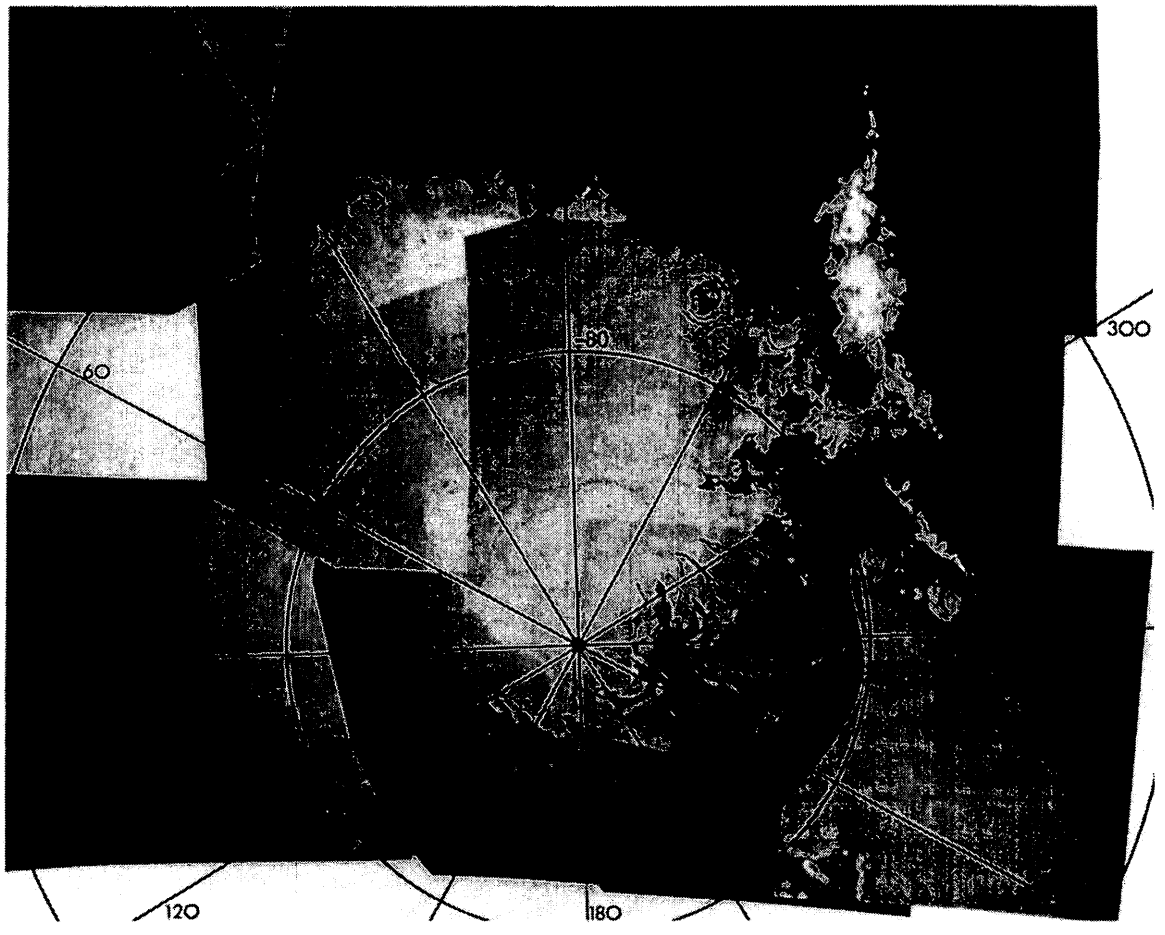

Figure 5.15c: CO_2 ice cap, observed by Viking Orbiter2 during the extended Viking mission at shortly before summer solstice (Ls = 262.6°). The south polar cap is asymmetric and its centre is displaced by about 6° from the pole (James et al., 1979).

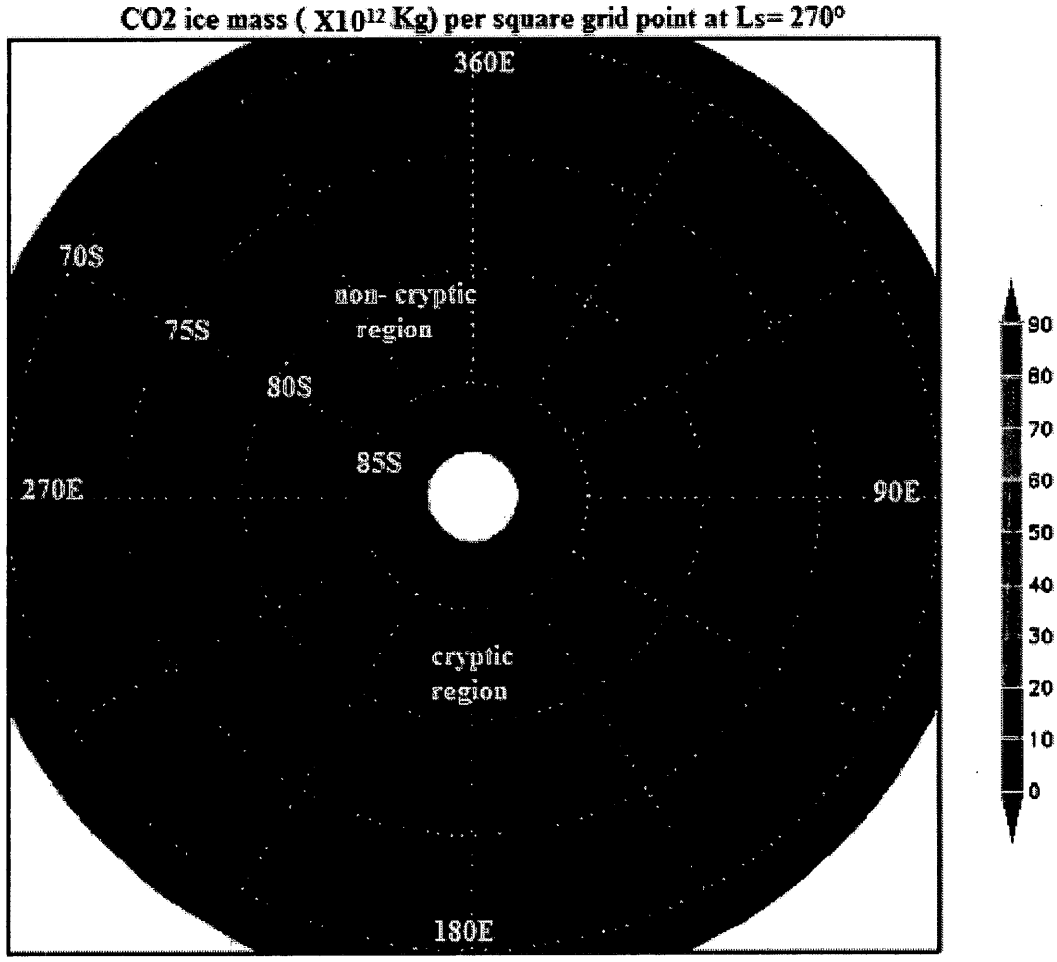

Figure 5.16a: A snapshot of CO_2 ice mass ($x10^{12}$Kg) per square grid point at Ls = 270° (standard version).

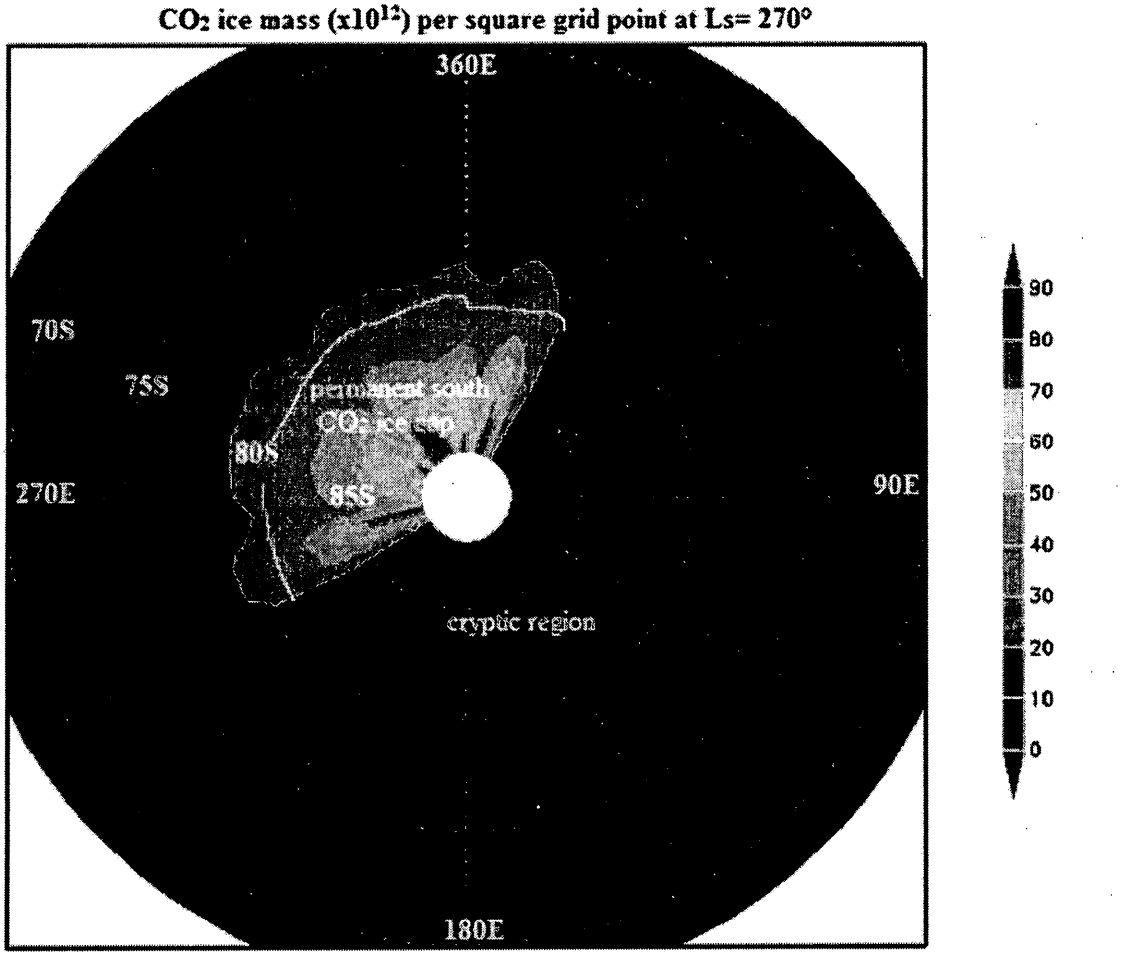

Figure 5.16b: A snapshot of CO_2 ice mass ($x10^{12}$) per square grid point at Ls = 270° (modified version).

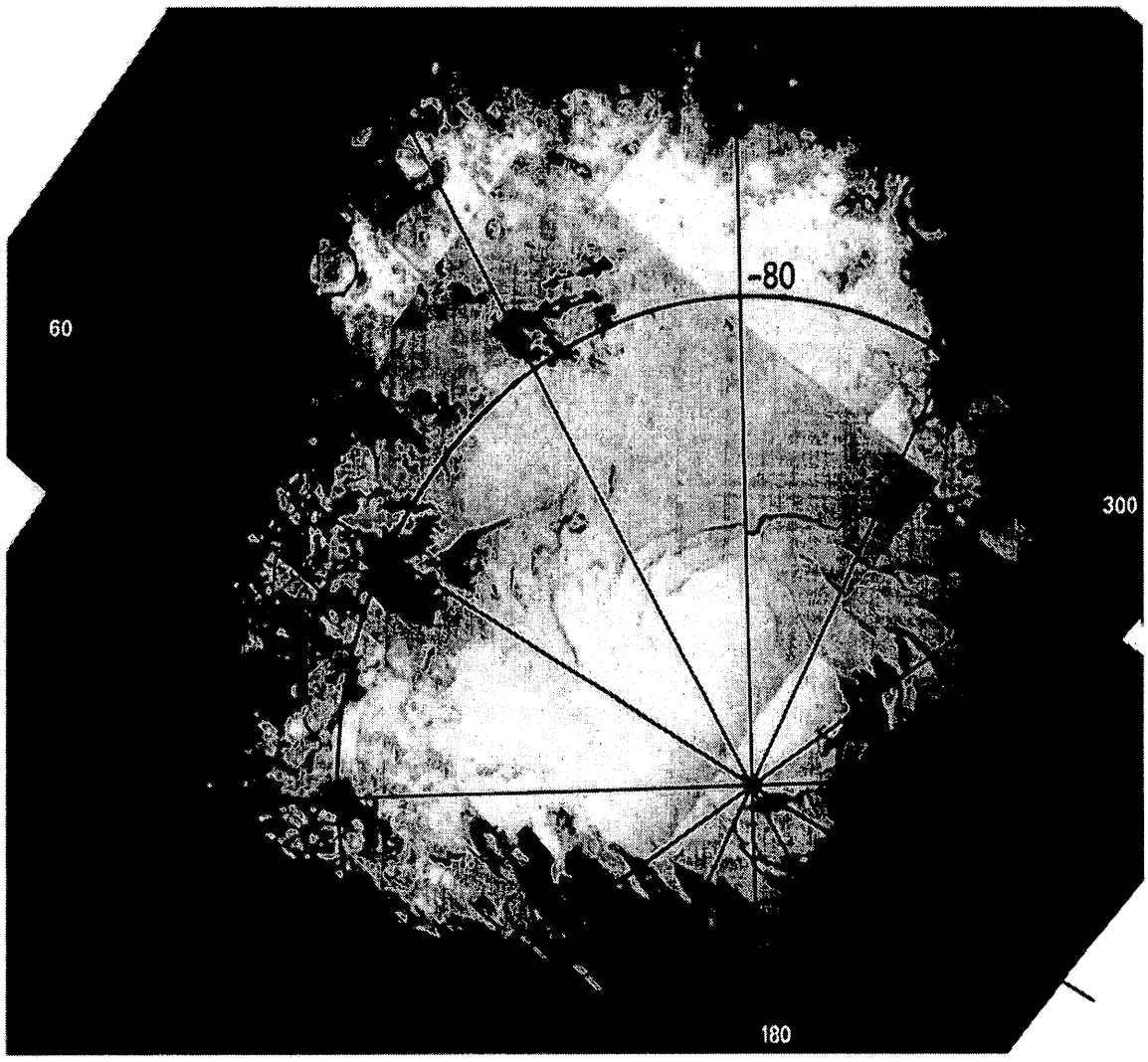

Figure 5.16c: CO_2 ice cap observed by Viking Orbiter2 during the extended Viking mission, at Ls = 274.5°, the south polar cap 6 sols after summer solstice (James et al., 1979).

Figures 5.17a shows a snapshot of the CO_2 ice cap at Ls = 321° in south polar stereographic map projection input from the modified version. Figure 5.17b is a photo-mosaic of south polar cap at Ls = 321.7° observed by Viking Orbiter2 (at first we show Viking images then Mariner image) during the extended Viking mission for orbit 370

(James et al., 1979). The color mosaic of Viking Orbiter2 observations shows the permanent south polar ice cap is about 400km across. Figure 5.16c also shows Mariner 9 B-Frame mosaic (Murray et al., 1972) of the south polar residual cap at Ls = 289.8° (around 60 sols earlier than Viking photo-mosaic). These high-resolution B-Frames were taken following the rapid recession of the ice cap. Frames were taken on orbits 116 through 188. They have been transformed to a common polar stereographic projection before the construction of the mosaics. These images have a spatial resolution about 300 metres with solar elevation angles ranging between 10°-15°. The shades of gray were optimized to detail ice covered areas, so that the ground (ice-free areas) appears. A comparison results from the modified version of the model (Figure 5.17a) with the observational data (Figures 5.17b and 5.17c) shows a better simulation than the standard version.

The modified version of GM3 has run for almost three Martian years and the results confirm that the artificial south polar residual CO_2 ice cap does not totally evaporate. Figure 5.17d shows the modified model results for the south residual CO_2 ice cap at, Ls = 335° and 695°.

Figure 5.17e shows standard and modified model results for the south residual CO_2 ice cap at, Ls = 90°, 180°, 270° and 360° respectively. Here we can see that the artificial south polar residual CO_2 ice cap is not allowed to disappear at all times in the modified version results.

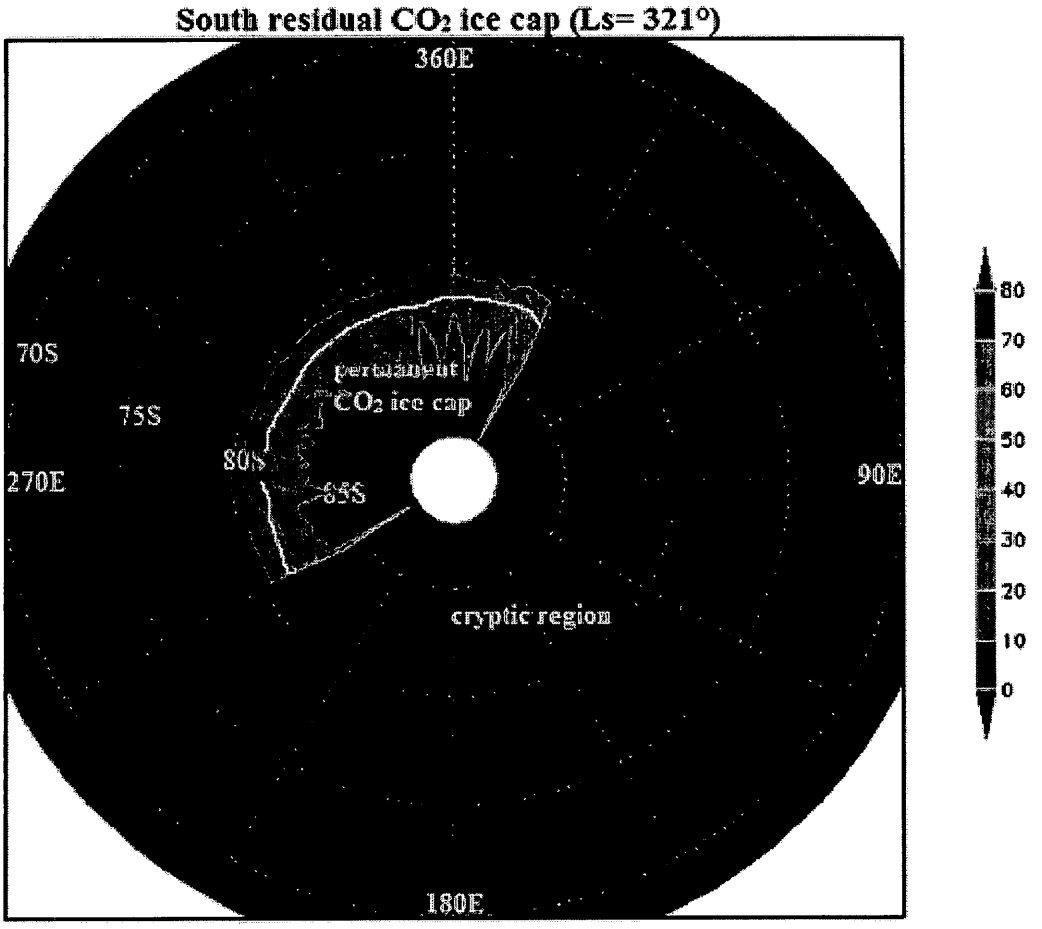

Figure 5.17a: Modified model result for the south residual CO_2 ice cap at, Ls = 321°. Ice mass is given by ($x10^{12}$Kg) per square grid point. The plot is not smoothed.

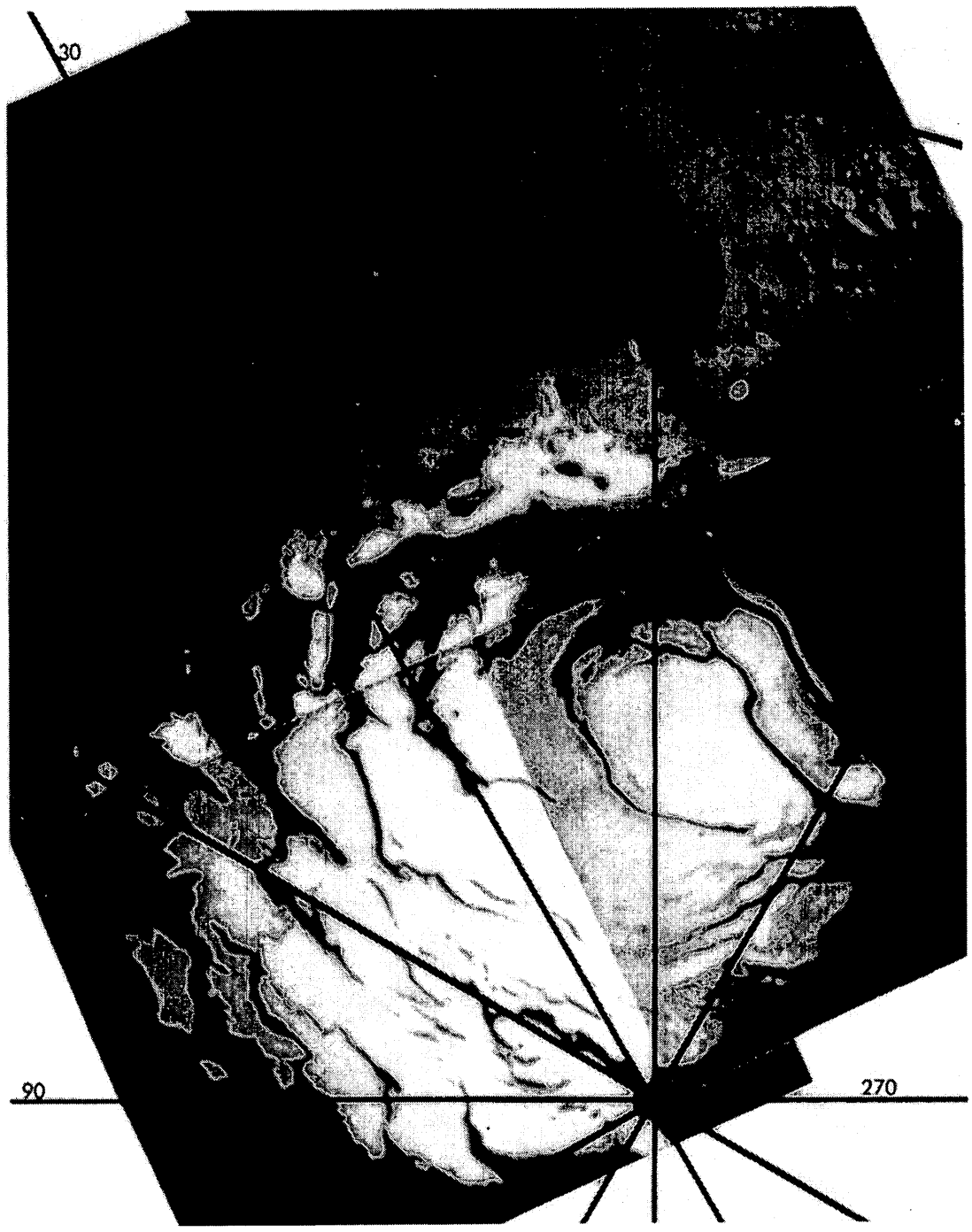

Figure 5.17b: CO_2 ice cap observed by Viking Orbiter2 during the extended Viking mission, at Ls = 321.7° (James et al., 1979).

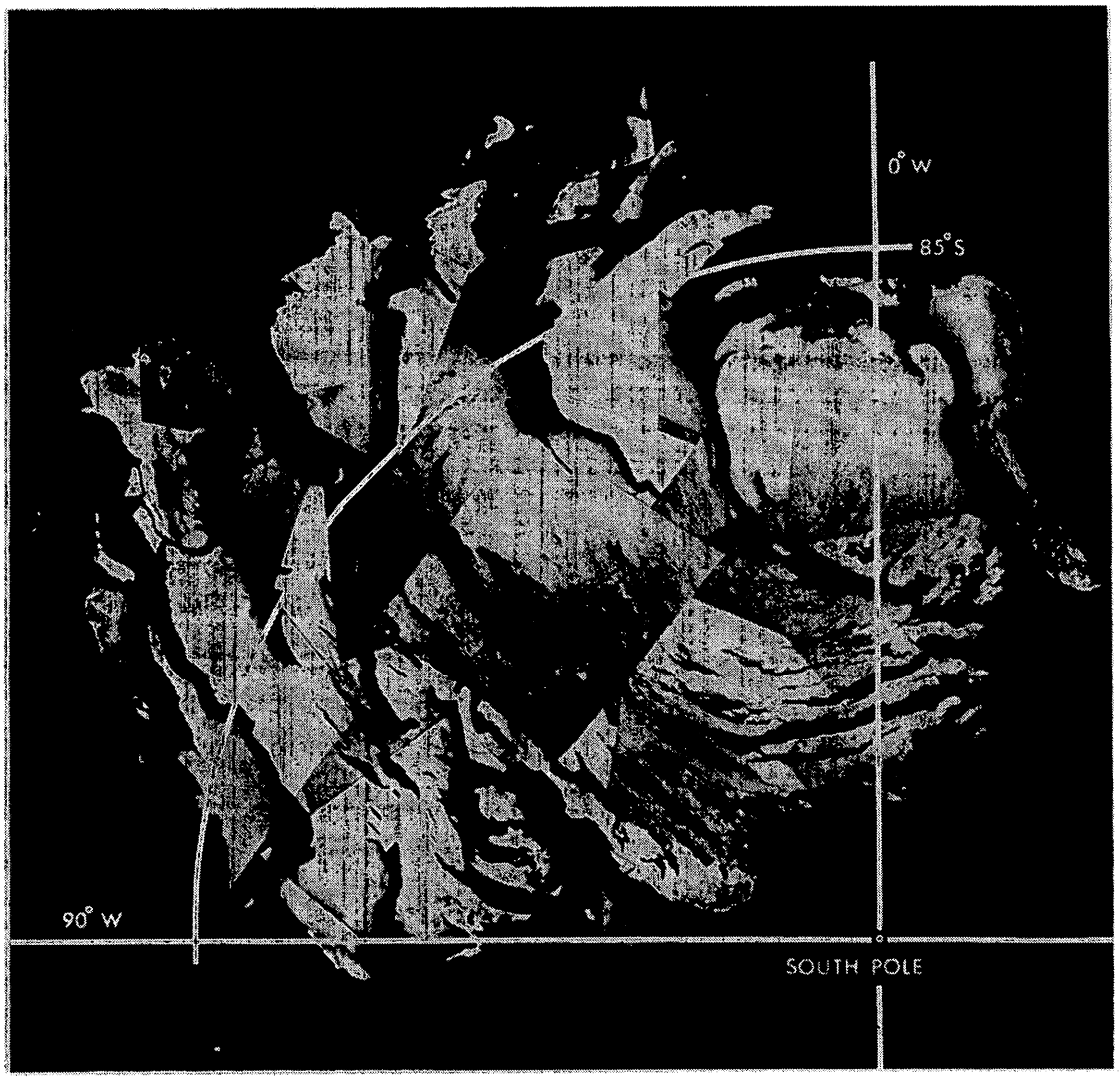

Figure 5.17c: Mariner 9B-Frame Mosaic of south polar cap following the rapid recession of the ice cap, at Ls = 289.8° (Murray et al., 1972).

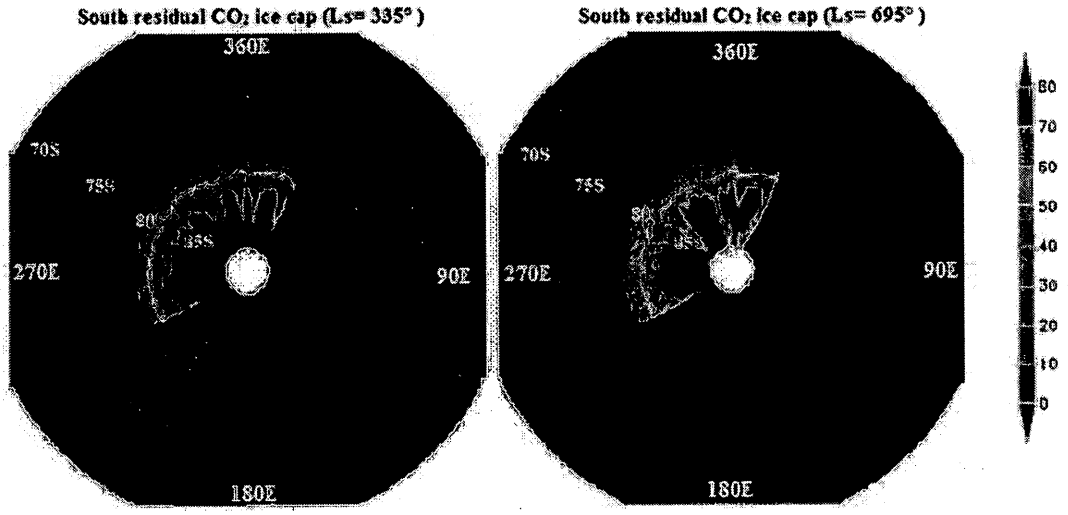

Figure 5.17d: Modified model result for the south residual CO_2 ice cap at, Ls = 335° and 695°. Ice mass is given by ($x10^{12}$Kg) per square grid point. The plots are not smoothed.

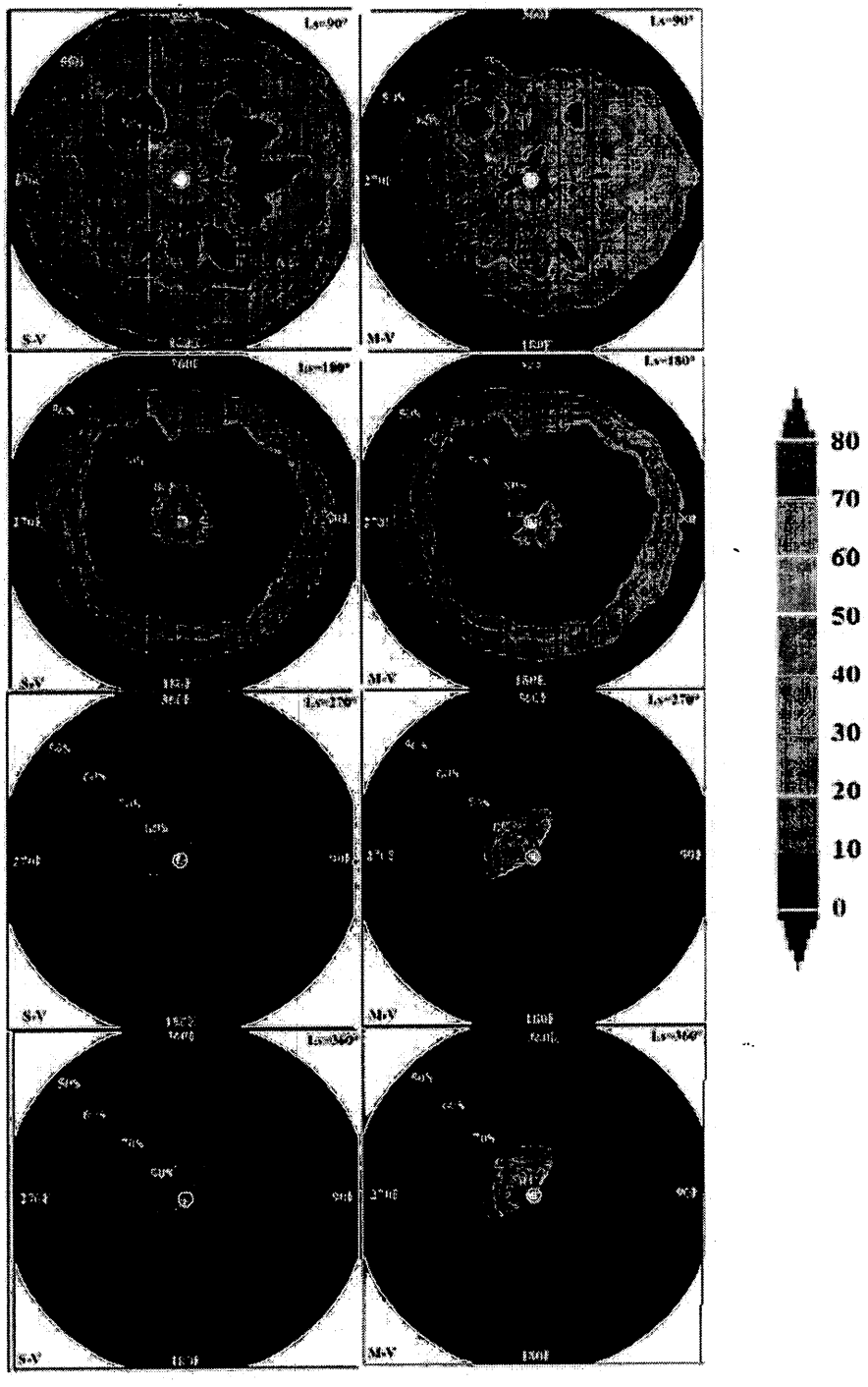

Figure 5.17e: Standard(S-V) and modified (M-V) model results for the south residual CO_2 ice cap (SRC) at, Ls = 90°, 180°, 270° and 360°. Ice mass is given by ($x10^{12}$Kg) per square grid point. The plots are smoothed.

5.7.1 The Modified Model South Polar Permanent Ice Cap Size Estimation

As noted earlier the diameter of the south residual cap as observed by Viking at Ls = 341° is approximately 400km (James et al., 1979).

The following provides an estimate of the artificial south residual ice cap. As has been; seen before, the area of permanent CO_2 covers between 90°S and 81.5°S in latitude and 240°E and 360°E in longitude plus between 90°S and 83°S in latitude and 0°E and 30°E in longitude. One degree of latitude on Mars is about 59.26 km. The grid "square" areas are really trapezoidal, not square. The areas scale with the cosine of the map's midpoint latitude. The total area is the sum of the two portions; (120° x 59.26 km) x (8.5° x 59.26 km) x cos (86°) and (30° x 59.26 km) x (7°x 59.26 km) x cos (87°) which is equal to 2.89×10^5 km^2 in area with diameter of approximately 537km. The artificial permanent cap diameter is almost 1.34 times bigger than the observed distance across the south residual ice cap (~400km) but given the model resolution this seems like a reasonable approximation, since our goal is to investigate the impact of a permanent CO_2 ice cap.

5.7.2 South Polar Permanent Ice Cap Surface Temperature

Figures 5.18a and 5.18b show surface temperature poleward of 70°S in a polar stereographic projection for Ls averaged between 290°-320° in the standard version and the modified version respectively. As can be seen in Figure 5.18b in the modified version, the average surface temperature at the permanent south polar cap in the coldest area is ~140-150K, controlled by the surface CO_2 ice, whereas in the standard version the surface

temperature at the same area is ~200-210 K. The OMEGA observations[18], which were made between 18 January and 11 February 2004 when it was late summer (~Ls = 330°) in the Martian southern hemisphere confirmed temperatures of 143 K at the southern permanent ice cap (Giuranna et al., 2008).

Figure 5.18c shows surface temperature poleward of 50°S in the same polar stereographical projection for Ls averaged between 240°-260° centred at Ls = 250° in the modified version. As it can be seen in this figure, the averaged surface temperature at the permanent south polar cap in the coldest area is ~140-150K. Figure 5.18d shows the measured south polar cap temperature at Ls = 251°. The data[19] used in this analysis is from the Mars Global Surveyor (MGS) Thermal Emission Spectrometer (TES). As it can be seen, the south polar permanent cap temperature observed by MGS is around 150K. Also the temperature away from the ice cap around 65°S measured by TES at Ls = 251° is ~263 K (-10° C) compared to predictions of ~255 K by the modified model version for Ls 240°-260°. The modified model surface temperature at the southern permanent ice cap is more realistic than the standard version.

[18] http://www.esa.int/SPECIALS/Mars_/Express/SEMYKEX5WRD_0.html
[19] http://astrogeology.usgs.gov/geology/mars-ice

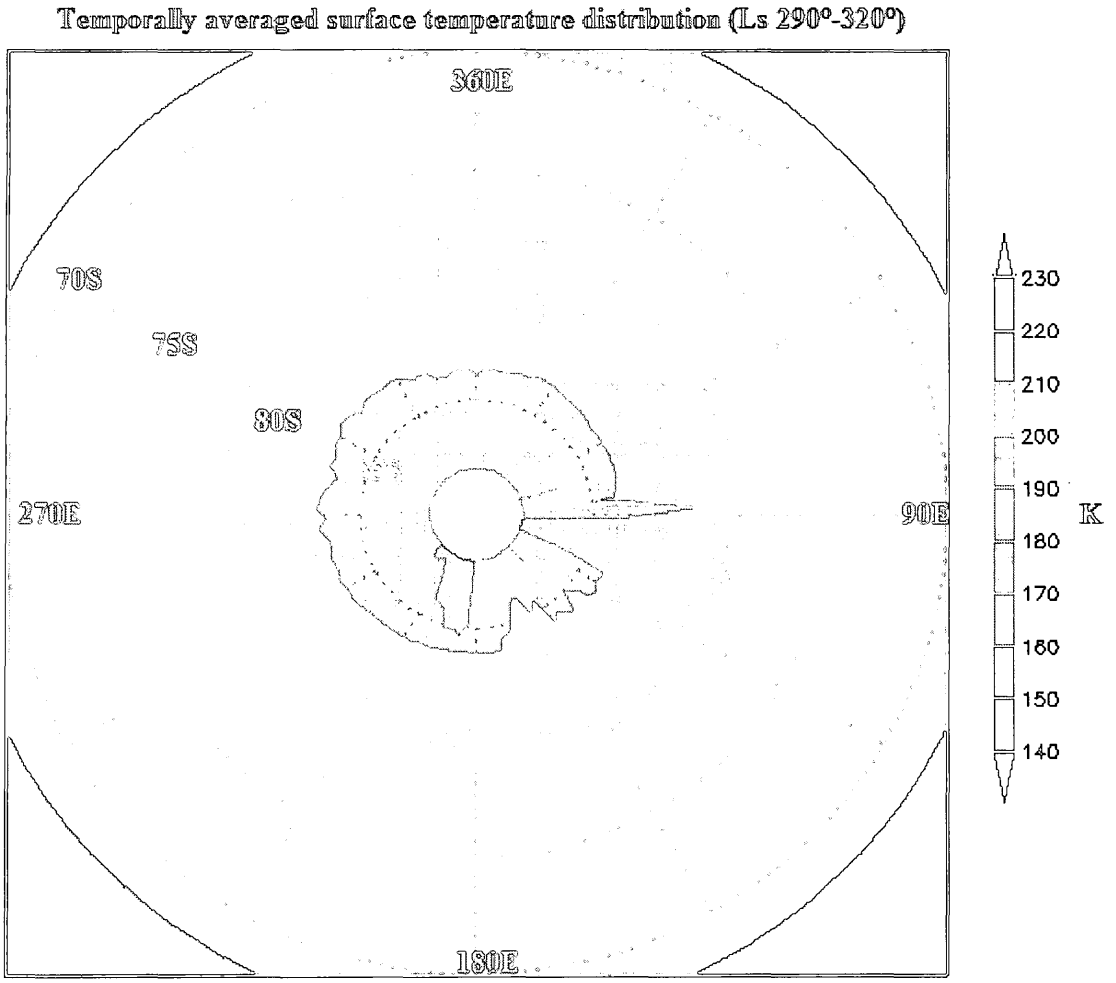

Figure 5.18a: A 2-D temporally averaged surface temperature distribution for Ls = 290°-320° (standard version).

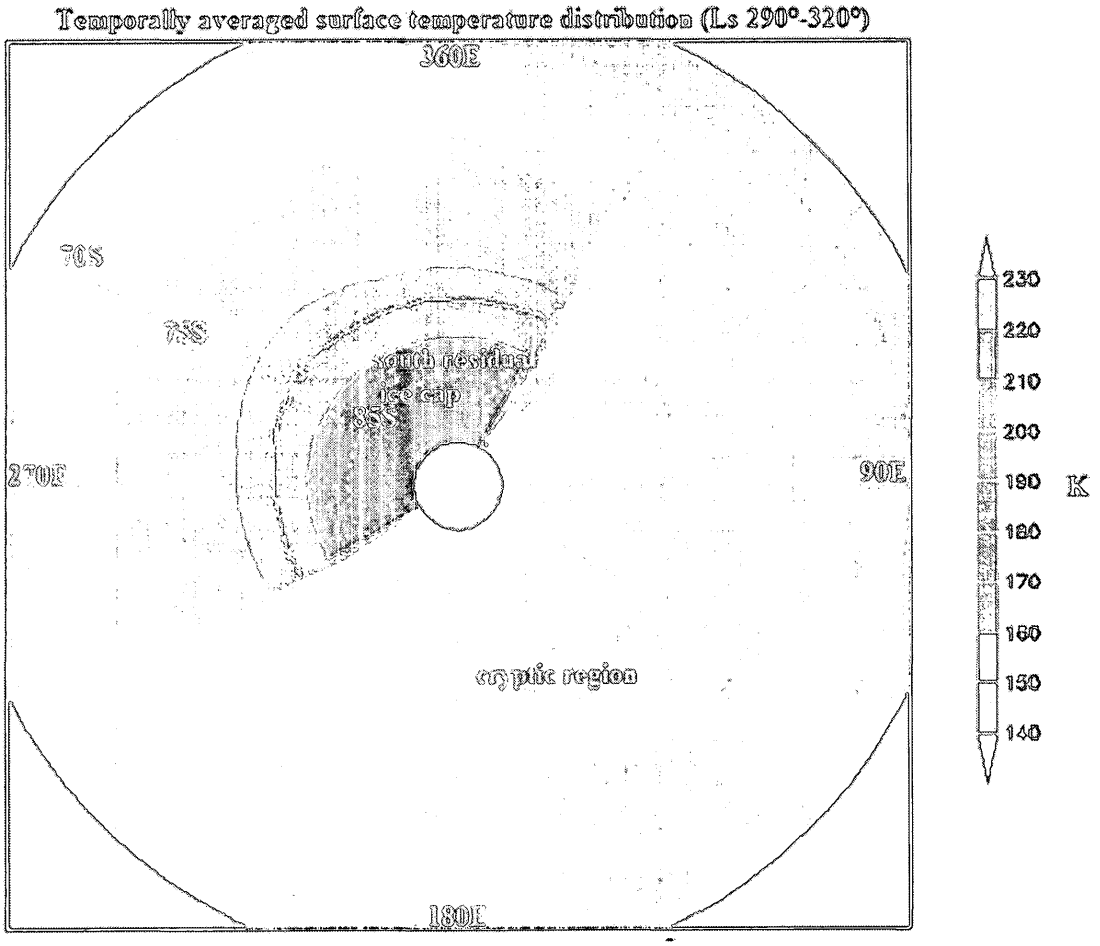

Figure 5.18b: A 2-D temporally averaged surface temperature distribution for Ls = 290°-320° (modified version).

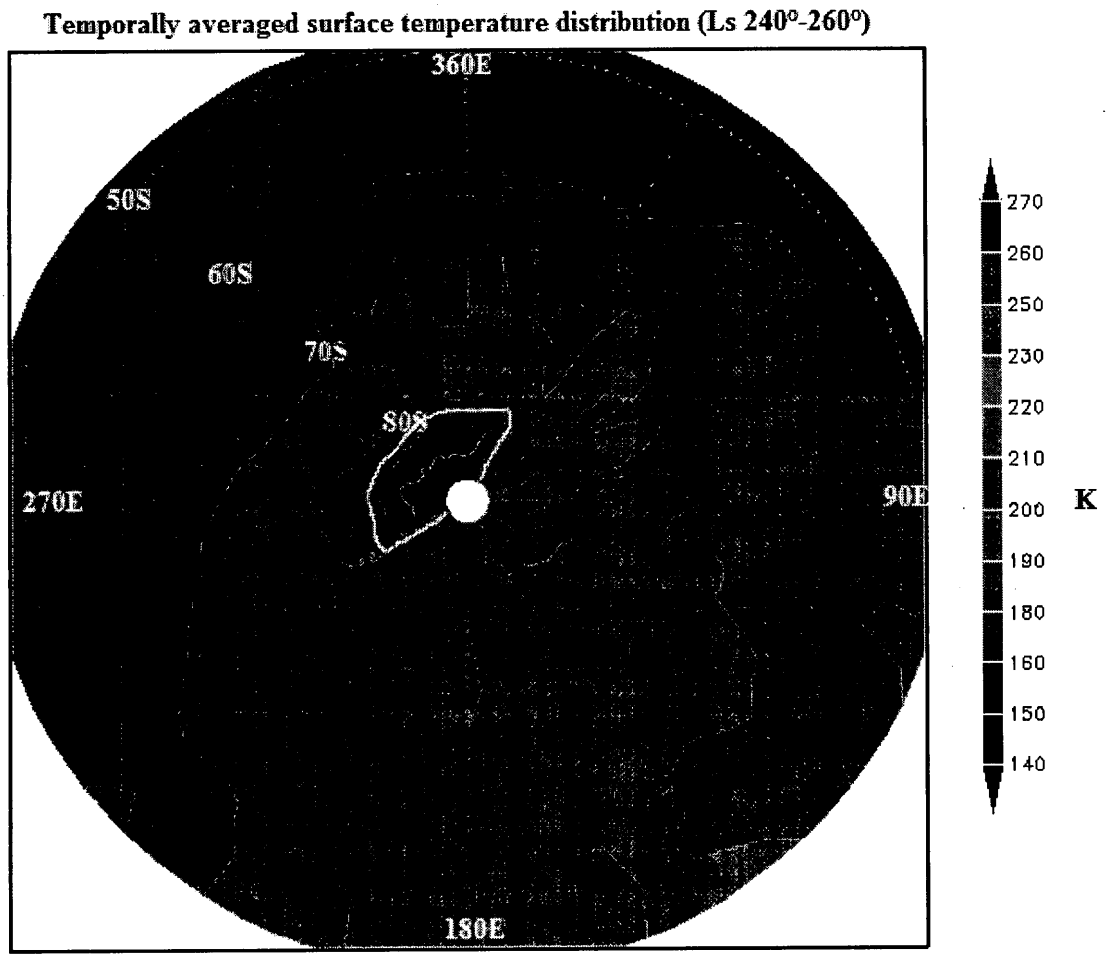

Figure 5.18c: A 2-D temporally averaged surface temperature distribution for Ls 240°-260° (modified version).

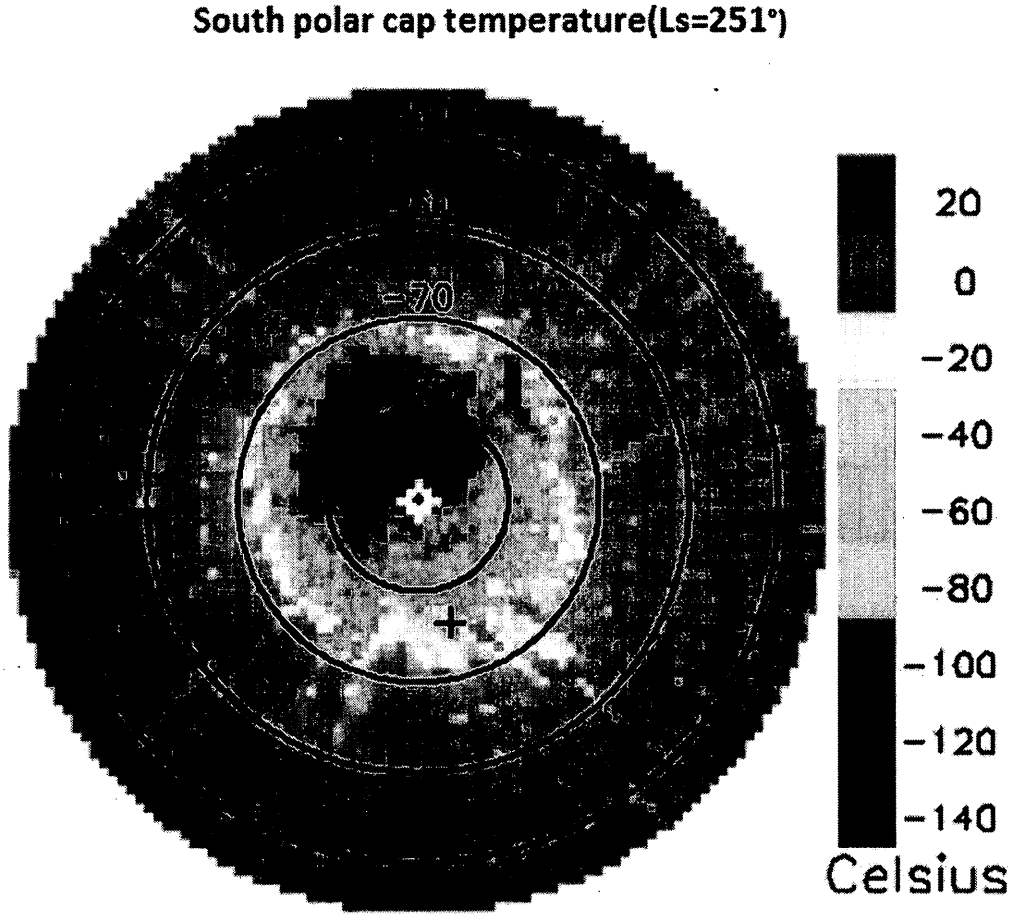

Figure 5.18d: South polar cap temperature at Ls = 251°. The data used in this analysis is from the Mars Global Surveyor (MGS) Thermal Emission Spectrometer (TES). Figure from http://astrogeology.usgs.gov/geology/mars-ice.

5.7.3 South Polar Cap Surface Pressure

Figures 5.19a and 5.19b show the actual surface pressure on a south polar stereographic map projection for Ls averaged between 290°-320° in the standard version and the modified version respectively. Clearly, there is a significant difference between these two scenarios with the stronger surface pressure gradient around the pole with a

lower value in the low pressure centre (4.6 mb comparatively to 4.8 mb) in the modified version rather than standard version. This difference can be very important in south polar meteorology during the southern summer. The existence of a surface pressure gradient associated with a cyclonic system (Figure 5.19b) along with a temperature gradient (Figure 5.18b) can cause the development of active weather systems such as cloud formation or increasing wind speed near the surface (see section 5.7.4) and also the possible initiation of dust storms in the south polar region during the southern summer period. This shows the impact of the south residual CO_2 ice cap on south polar summer weather structure.

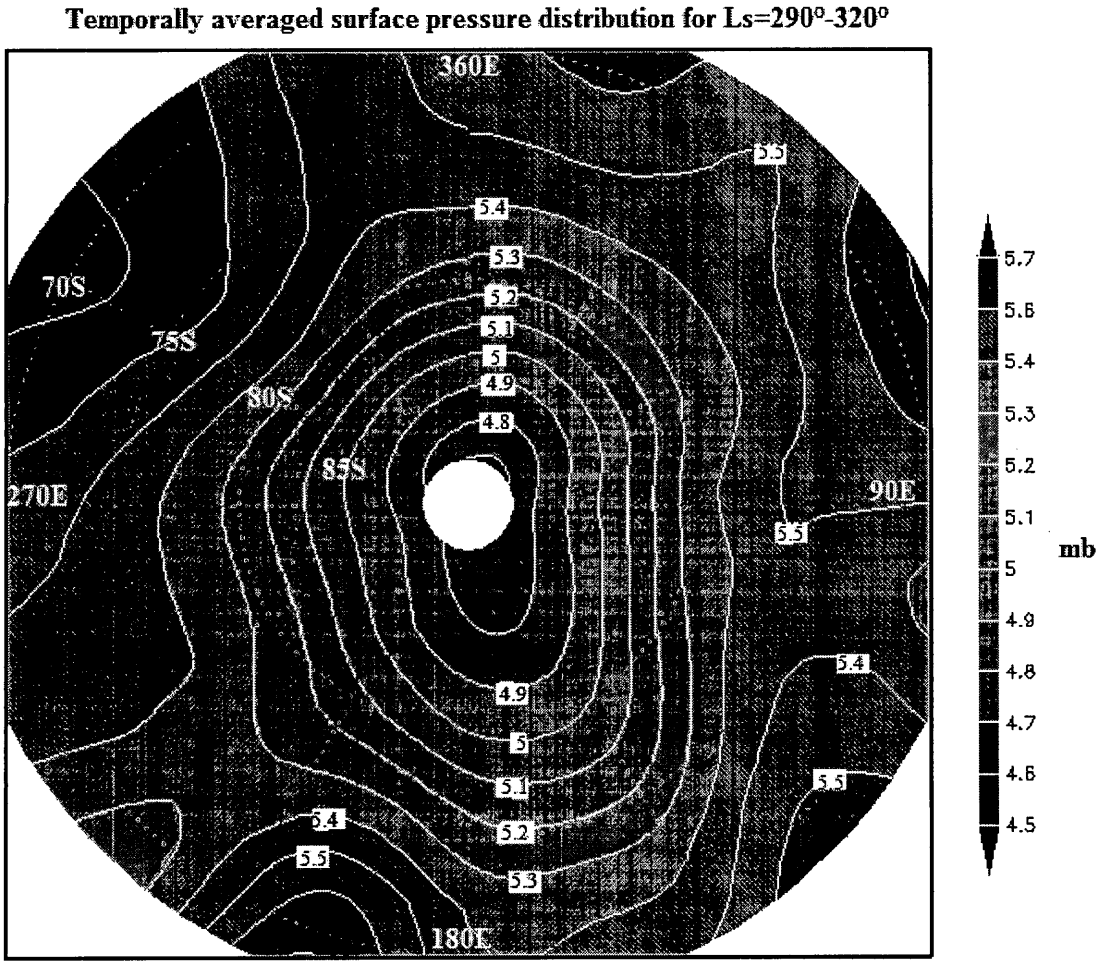

Figure 5.19a: A 2-D temporally averaged surface pressure distribution for Ls = 290°-320° (standard version).

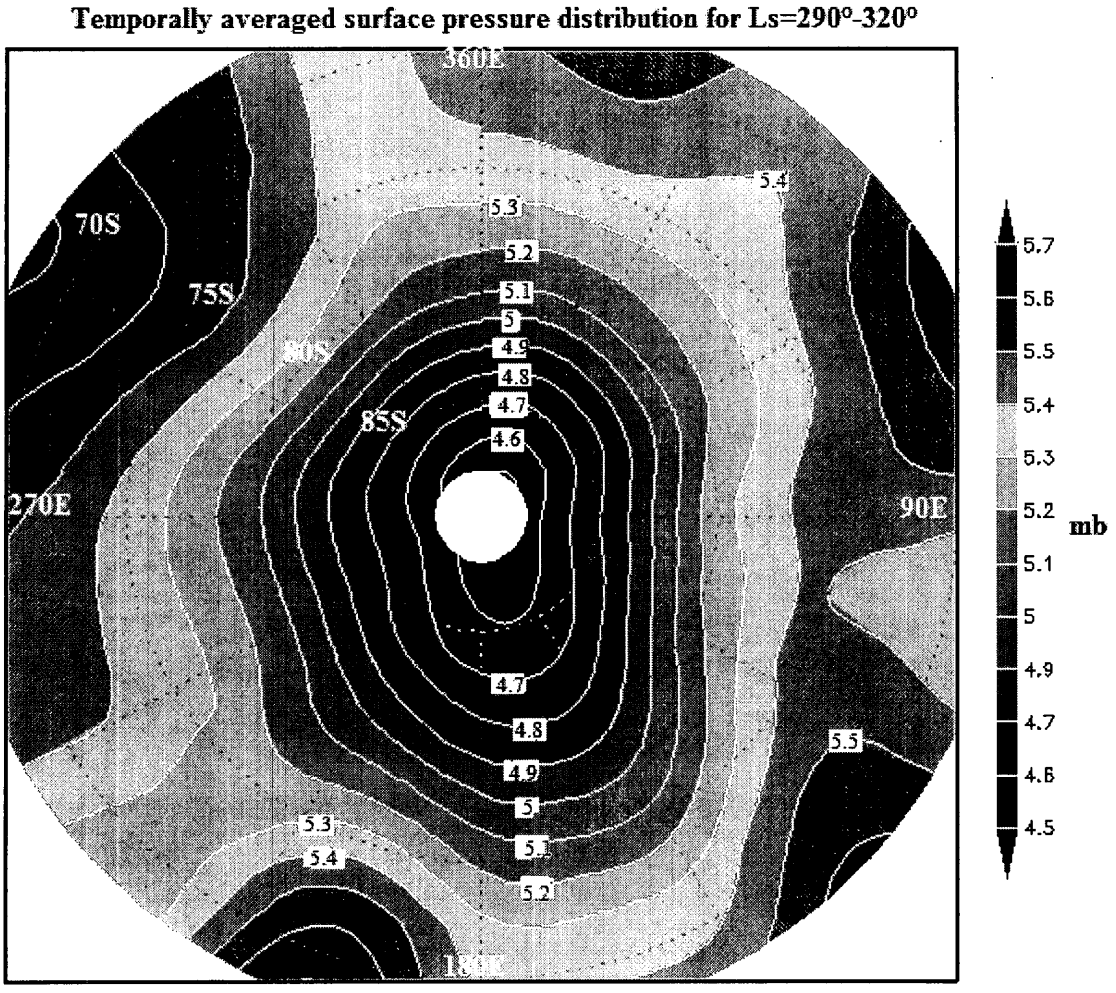

Figure 5.19b: A 2-D temporally averaged surface pressure distribution for Ls = 290°-320° (modified version)

5.7.4 South Polar Cap surface Winds

Figures 5.20a and 5.20b show the near-surface (10 metre) horizontal wind in a south polar stereographic map projection for Ls averaged between 290°-320° in the standard version and the modified version respectively. Clearly, there is a significant

difference between these two scenarios with the stronger zonal wind gradient around the permanent south polar cap area with a higher value in the core of the isotach lines (~22m/s compared to ~12 m/s) in the modified version compared to the standard version. This difference is very important because, the surface winds, which can reach to a maximum of 16 ms^{-1}, are linked to dust lifting (Holstein-Rathlou et al., 2010).

Figures 5.21a and 5.21b show the near surface zonal wind (10 metre) in a south polar stereographical map projection for Ls averaged between 290°-320° in the standard version and the modified version respectively. Clearly, there is a strong zonal wind shear around the permanent south polar cap area in the modified version which is not present in the standard version. This difference also can be seen in the meridional wind (figures not shown here). As we mentioned before (see section 5.7.3), this difference in the horizontal and zonal winds structure can be very important in south polar meteorology during southern summer and also in possible initiating dust storms. Figure 5.22 shows the typical dust activity during midsummer near the south pole (Toigo et al., 2002).

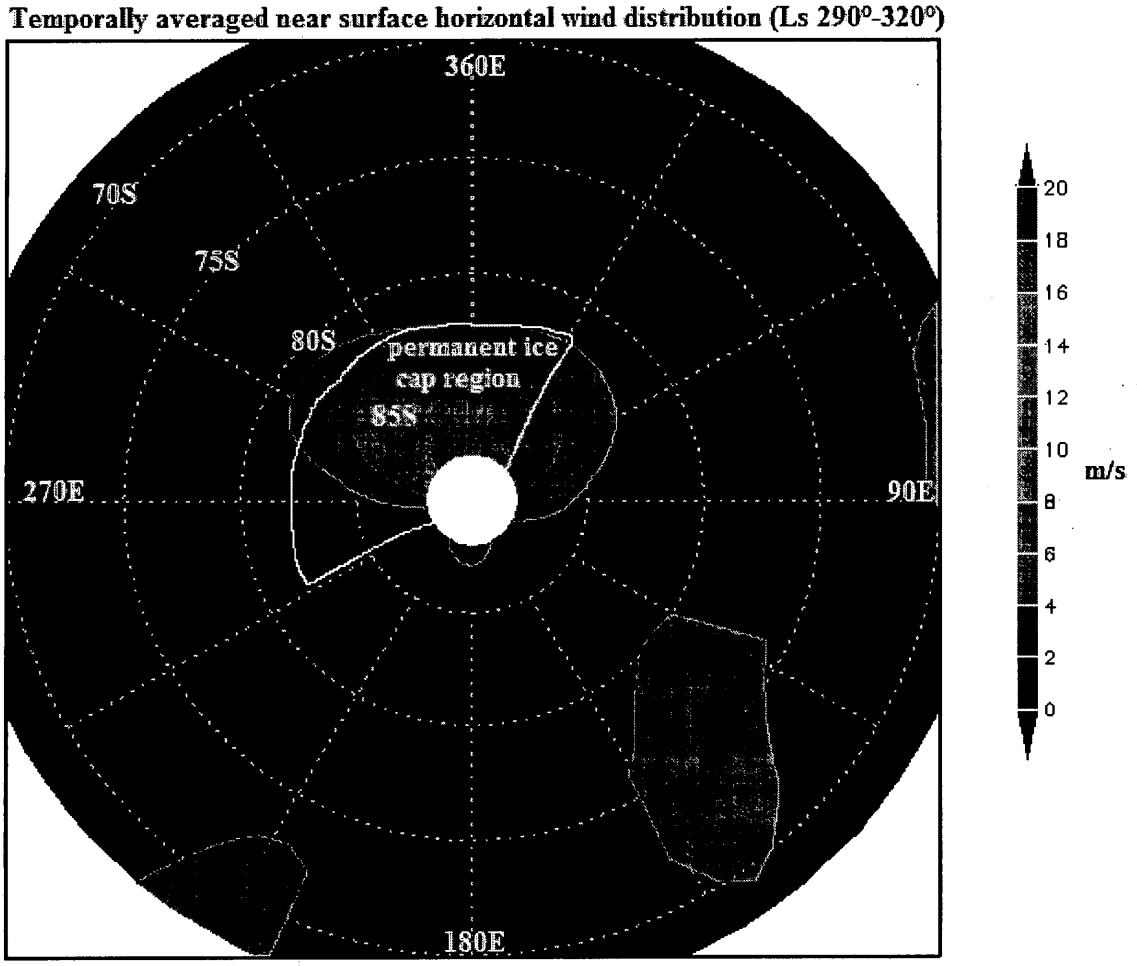

Figure 5.20a: A 2-D temporally averaged near surface (10m) horizontal wind (m/s) distribution for Ls 290°-320° (standard version). The highest value in the core of isotach lines is around 12 m/s.

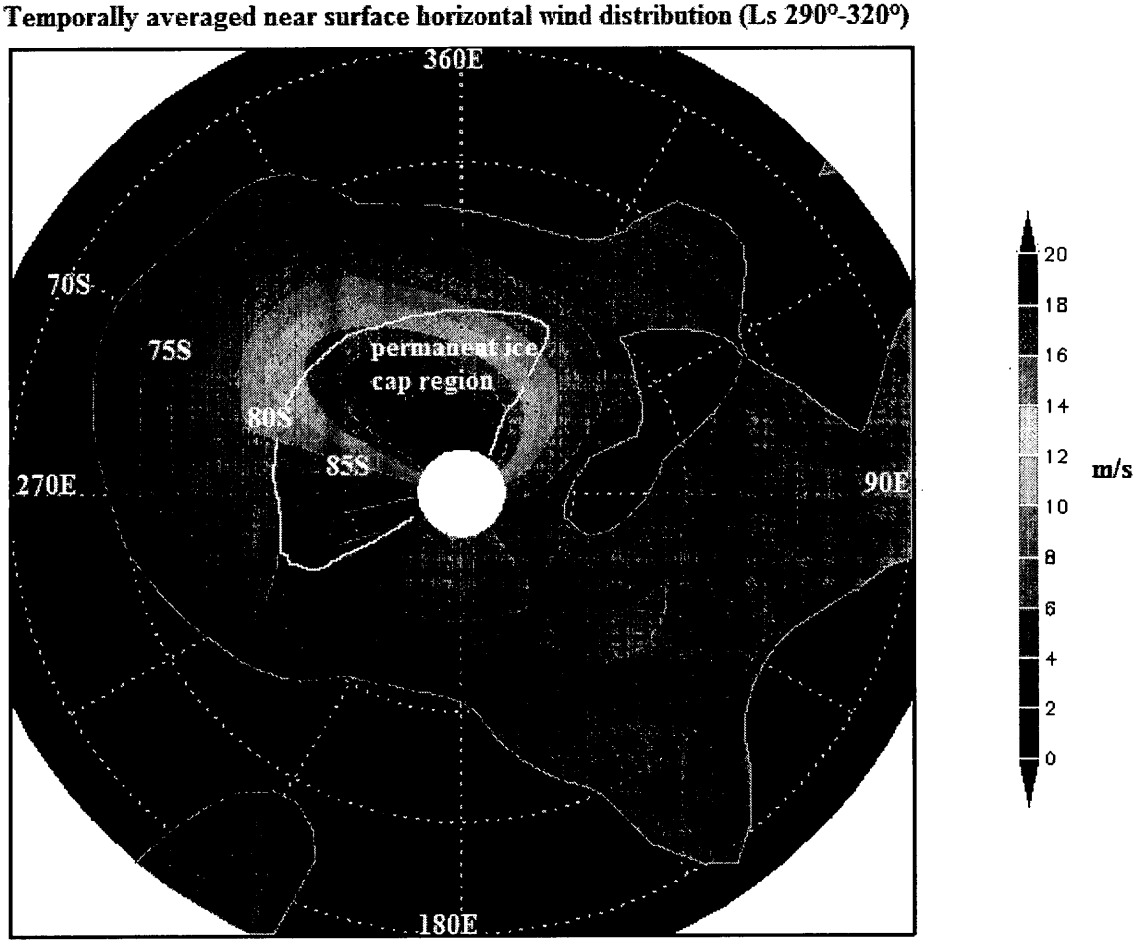

Figure 5.20b: A 2-D temporally averaged near surface (10m) horizontal wind (m/s) distribution for Ls 290°-320° (modified version). The highest value in the core of isotach lines is around 22 m/s.

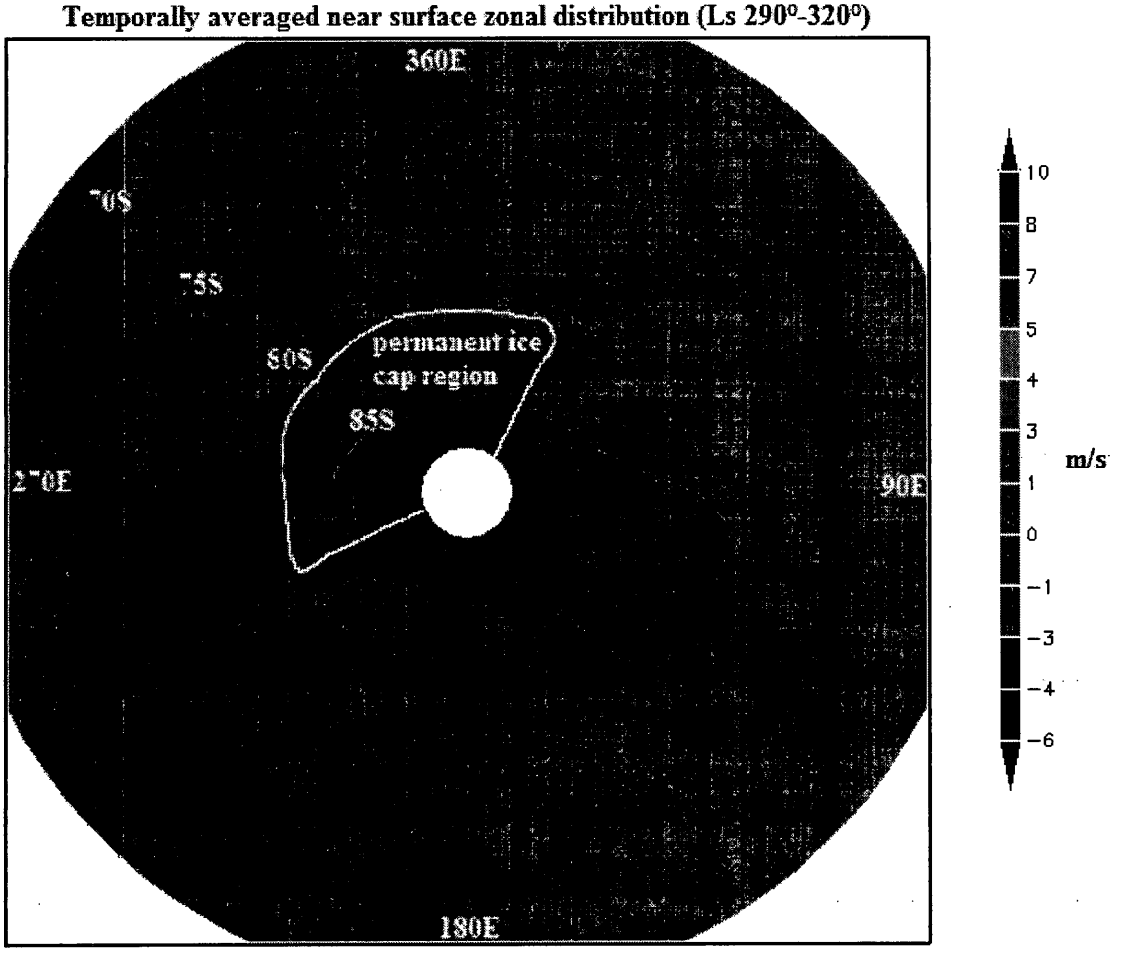

Figure 5.21a: A 2-D temporally averaged near surface (10m) zonal wind (m/s) distribution for Ls 290°-320° (standard version).

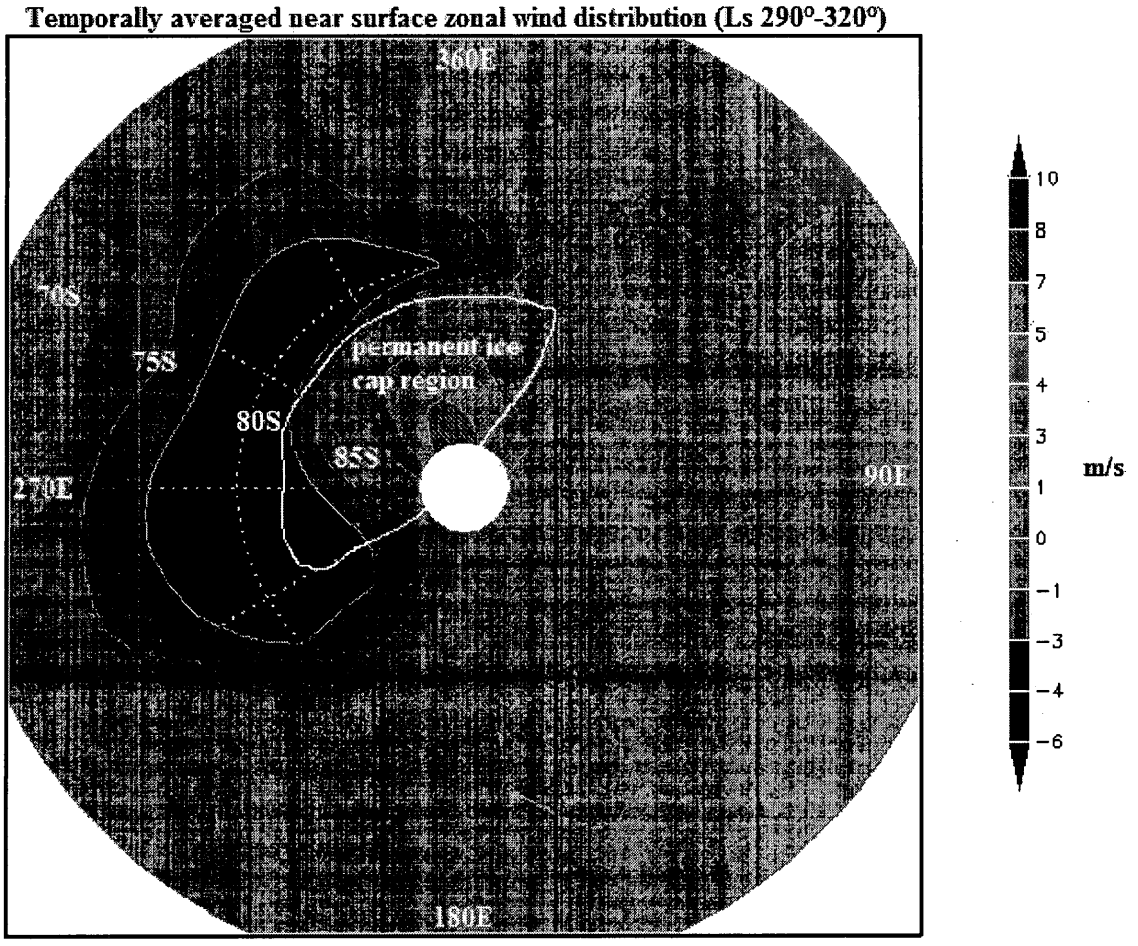

Figure 5.21b: A 2-D temporally averaged near surface (10m) zonal wind (m/s) distribution for Ls 290°-320° (modified version). There is a strong zonal wind shear around the boundary of the permanent south polar cap area.

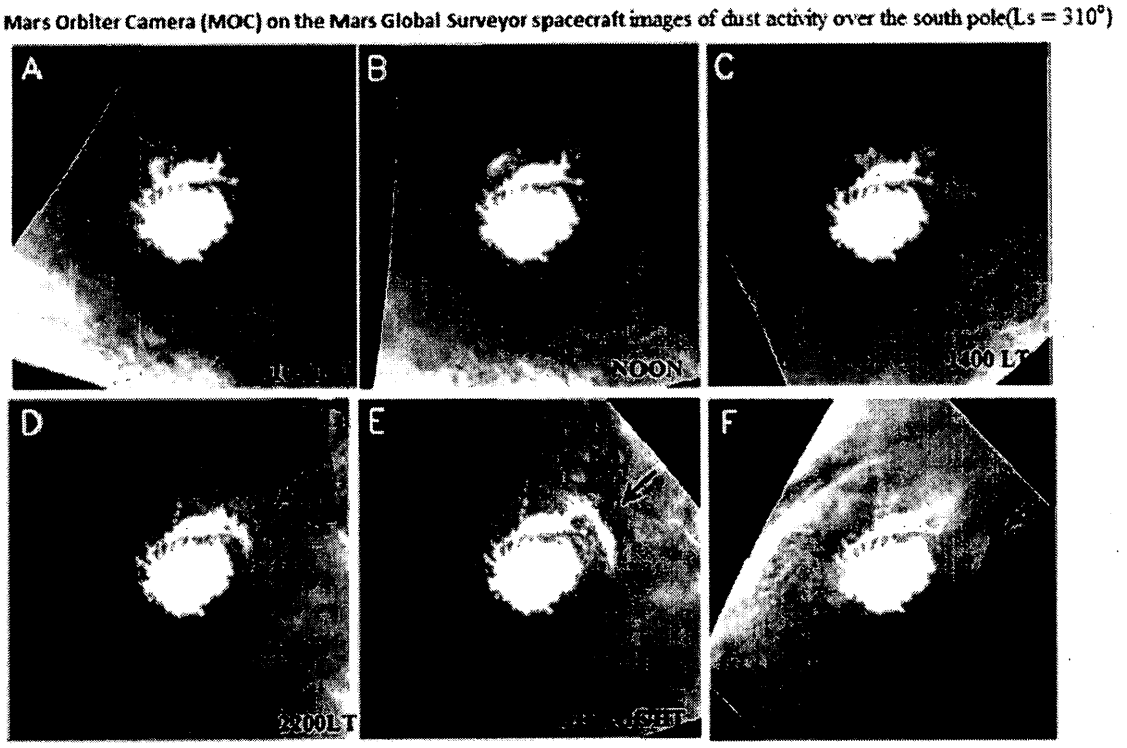

Figure 5.22: Mars Orbiter Camera (MOC) on the Mars Global Surveyor Spacecraft (MGS) images of dust activity over the south polar cap area at Ls = 310°. The black arrows show the dust clouds (Figure from Toigo et al., 2002).

Chapter 6

Conclusions and Future Work

The main objective of this thesis was to show how different local weather patterns can affect the structure of the Martian South Polar CO_2 Ice Cap. Following Colaprete et al. (2005) this study initially focused on the importance of topography and showed that topography influences the Martian south polar regional weather patterns during local fall and winter seasons. Local weather plays an important role as well as surface albedo values of the frost or snow cover over the Martian south polar cap.

So as the first step in this work, meteorological and physical simulations from Global Mars Multiscale Model (GM3-v2) were analysed with simulations for both a flat Mars and a Mars with realistic topography.The results revealed the impact of topography on different local weather systems and showed significant differences in the horizontal and vertical cross-section of temperature when topography was removed from the model. In our methodology, wind streamline analysis has been used. The wind streamline analysis

is a very good method to show the areas of convergence and divergence of mass flow (Saucier, 2003). Thus, patterns of motion can be interpreted immediately and certain peculiarities such as singular point (convergence or divergence) or the centre of a cyclonic or anti-cyclonic circulation for which streamlines are closed (Saucier, 2003) can be seen. The pattern of wind streamlines around the north pole during the northern winter has a nearly symmetric cyclonic pattern whereas the pattern at the south pole during southern winter has an asymmetric structure, which is associated with differences in local weather in the southern hemisphere. The distinct regional weather is a result of the dynamical forcing of the large scale topography of the Hellas and Argyre basins (Colaprete et al., 2005). Wind streamlines from Ls = 20° (early southern fall) to Ls = 200° (early southern spring) for each Ls have been analyzed. Wind streamline pattern analysis shows that around early southern fall (Ls = 22°), a cyclonic trough develops to the south east of Hellas basin (centred at 42.7°S and 70°E) in the eastern hemisphere. At this time we can see another cyclonic trough system (weaker than the eastern one) in the south west of the Argyre basin (centred at 49.7°S and 316°E) in the western hemisphere. Also the results show the development of the first cyclonic cell around middle fall (Ls = 47°) to the south east of Hellas (eastern hemisphere). After a time lag, around 30 Martian sols (Ls = 63°) a second cyclonic cell develops to the south west of Argyre basin (western hemisphere). The eastern cyclonic system was not reported by Colaprete et al. (2005). In their work, they have reported that the Martian winter weather is controlled by a cyclonic system near the south pole in the western hemisphere and a anti-cyclonic system in the

eastern hemisphere, again near the south pole. Here we have shown that there are two cyclonic circulations; one around the Hellas basin (in the eastern hemisphere) and the second one around the Argyre basin (in the western hemisphere). These results confirm what has been reported by Barnes and Tyler, (2007); Forget et al., (1998); and Leovy, (1979). Observation of the Martian global condensate clouds by the Mars Global Surveyor Mars Orbiter Camera for the Second Martian Year (Wang, 2004) confirms the occurrence of the both eastern and western cloud systems during the period of study. These two cloud systems can be controlled by the two mentioned cyclonic systems shown by wind streamline analysis. However, between the two cyclonic cells the pattern is anti-cyclonic. The anti-cyclonic system extends to the cryptic region while the expansion of the cyclonic systems covers the non cryptic regions. These two different regional weather patterns (cyclonic and anti-cyclonic systems) dominate most of the southern winter. These two distinct weather patterns (cyclonic and anti-cyclonic systems) have important impacts on the CO_2 vapour deposition during Martian winter around the pole. A cyclonic system will cause unstable weather conditions (e.g. cloud formation and precipitation) and therefore surface CO_2 ice accumulation is controlled by snow precipitation (with higher albedo) while the anti-cyclonic system causes relatively stable weather and frost accumulation is dominated by direct CO_2 vapor deposition (with lower albedo) at the surface. So it is the difference in these deposition styles that determines the cap albedo (Colaprete et al, 2005). Our model results also show that the anti-cyclonic pattern controls the weather between the two large scale basins. It extends and includes the cryptic region.

The eastern cyclonic system around the Hellas basin dominates the seasonal southern sub-polar weather pattern and persists longer than the western cyclonic system. However, wind streamline analysis from Ls = 150° to Ls = 200° shows a gradual weakening of these two cyclonic troughs. Then with the weakening of the south polar winter weather and formation of the southern spring weather pattern (increasing the temperature in the polar area) the ice cap experiences gradual shrinking based on the albedo of the surface ice cover. Observation of the Martian global condensate clouds by the Mars Global Surveyor Mars Orbiter Camera for the Second Martian Year (Wang, 2004) shows a gradual weakening of the western and eastern cloud systems after Ls = 150° and confirms that both systems disappear after Ls = 187° as we showed in wind streamlines study.

As described in section 5.1.1, there are two different styles of surface CO_2-ice formation (frost with direct deposition of CO_2-ice and CO_2 snow precipitation) over the Martian south polar regions to build up a seasonal ice cap during cold seasons. These two different deposition processes can control the south polar cap albedo. It is anticipated that small CO_2 ice grains or CO_2 snow, freshly precipitated to the surface result in bright surfaces or higher albedo while direct-depositing ice forms larger and rougher CO_2 frost grains on the surface resulting in darker surfaces or smaller albedo (Kieffer et al., 2000; Titus et al., 2001). Therefore, it is the darker frosty zones (cryptic region) that sublimate more rapidly during late spring and summer rather than the brighter areas covered by snow (Kieffer et al., 2000; Piquex et al., 2003). These two mechanisms result from different aspects of the dynamical forcing of the large scale topographical impacts of the

Hellas and Argyre basins (from NASA Ames Mars General Circulation Model and the second version of Global Mars Multiscale Model simulations).

Also due to the existence of the south polar residual CO2 ice cap (non-cryptic region) which remains covered by ice, even in the summer time, the albedo of the non-cryptic region is always different to the albedo of the cryptic region.

The standard GM3 physics code does not consider the difference between cryptic and non-cryptic albedo values. So as a second step in this work, the albedo values at the poles were modified to better represent the physical situation. It may be that the non-cryptic stable CO_2 ice cap is left over from a different era. Therefore, in this work, albedo and thermal inertia values have been modified in the south polar cryptic and non-cryptic areas. In the next step of this work albedo values were modified latitudinally and longitudinally at the south polar areas in the GM3 physics code. For the south polar CO_2 cap we have assigned higher values for albedo over the non-cryptic regions (residual CO2 ice cap) and we ensure that it is always covered by ice even in southern summer. For the cryptic region we have used lower albedo values (Vincendon et al., 2007; James et al., 2005; Byrne et al., 2003; Forget, 1998). Also thermal inertia has been modified slightly at non-cryptic and cryptic regions (Putzig and Mellon, 2007). Here these values were fixed in the physics code and the model was run nearly for more than two Martian years, starting from an initial condition at Ls = 80°. The new results show the asymmetrical pattern of CO_2 ice in cryptic and non-cryptic regions during the transition seasons in the Martian southern hemisphere. The model results for the second part of southern spring

(~Ls = 240°-260°) showed less surface ice mass than standard model version results around the cryptic region and more in relation to CO_2 ice mass distribution near the south pole.

However, the residual CO_2 cap simulation remains more challenging because the simple energy balance models (with time-invariant albedo and emissivity values chosen to fit the Viking Landers pressures) used by all published General Circulation Model results do not predict the residual CO_2 ice cap (Guo et al., 2010).

However, the seasonal carbon dioxide ice in the south polar regions is present in the surface ice simulation by the second version of the Global Mars Multiscale Model, but it does not produce a permanent south CO_2 ice cap, and so it must be modified in the physics code in order to capture the realistic physical (such as ice process detail; probably makes a bias in terms of total CO_2 ice) and meteorological processes in the model aside from ice formation. The permanent south CO_2 ice cap in the model can significantly improve south polar meteorology for example in predicted *surface* temperatures (see section 5.7.2), surface pressures, and dust activity or cloud occurrence (see section 5.7.4 and Figure 5.22) over the south cap during its summer.

So, as a third step in this work an artificial ice cap with an average CO_2 ice thickness around 8.6 metres in the southern polar regions based on Mars images was included. The ice blanket has been located initially in the physics module based on its observed location. Here, the subsequent results use a permanent CO_2 ice cap of fixed size even during southern summer. Indeed, the non-cryptic region is covered with a blanket of

CO_2 ice even in southern summer and is not eroded through summer sublimation, in agreement with the observations. Of course, the temperature of permanent CO_2 ice areas should be fixed at the CO_2 condensation temperature year round by contact with the atmosphere so its temperature always remains ~140-150K while the ice is in place. Also the formation of the seasonal ice cap over the artificial south polar residual CO_2 ice cap during cold seasons is allowed but the evaporation from the artificial residual ice cap is not allowed reducing the initial thickness of the artificial cap during the warm seasons. So the modified model version always presents an initial artificial polar residual CO_2 ice cap.

The results were compared for the southern summer (~ Ls = 263°, 270°and 321°) with the color mosaic images of Viking Orbiter2 and Mariner 9. Comparison of the modified model version plots with the observational data suggests a good correspondence. Here, the model was run for more than two Martian years, starting from Ls = 80° and the results confirm that the artificial ice cap does not evaporate and remains (i.e. Ls = 695°).

Also the surface temperature predicted by the modified version, for Ls averaged between 290°-320° at the permanent south polar cap, in the coldest area is ~140°-150°K (controlled by the existence of surface CO_2 ice) rather than ~200 K in the standard version. The OMEGA observations during late summer for the Martian southern hemisphere confirm the temperatures near 143°K at southern permanent ice cap (Giuranna et al., 2008). The simulation of the surface temperature at the southern polar regions is better realised than for the standard version.

A comparison of the surface pressure in the south polar stereographic map projection for Ls averaged between 290°-320° in the standard version and the modified version shows the stronger surface pressure gradient around the pole with lower value in the low pressure centre (4.6 mb comparatively to 4.8 mb) in the modified version rather than standard version. Also a comparison of the near-surface horizontal wind predicted by the modified and standard versions, for Ls averaged between 290°-320° at the south polar cap shows a significant difference between these two scenarios with the stronger horizontal wind gradient around the pole with higher value in the core *of isotach lines* (22m/s comparatively to 12m/s) in the modified version rather than standard version. Also, there is a strong zonal wind shear around the permanent south polar cap area in the modified version map analysis which cannot be seen in the standard version.

Thus, the existence of a surface pressure gradient associated with a cyclonic system along with surface temperature and a stronger wind gradient (which can be predicted by the modified version) can cause the development of active weather systems which induce cloud formation with increasing wind speed near the surface. It is also possible that dust lifting at the south polar region during the southern summer period could be initiated. This shows the impact of the south residual CO_2 ice cap on south polar summer weather structure and if future work confirms this, it has implications for the evolution of the Martian atmosphere.

6 Future Outlook

Here, the model results have shown the importance of large-scale topographical features of Hellas and Argyre basins in the southern Martian local winter weather patterns. Since, the topography has an important role in the Martian weather in a variety of ways ranging in large scale to small scale, future work is needed to carry out the model simulation in higher resolution to capture other topographical structures such as Chasma Boreale in the north polar cap and Chasma Australe in the south polar cap to better understand of Martian polar meteorology. The effect of local weather systems on dust storm formation will be another interesting issue. Also it is very important to understand the evidence of different types of terrestrial fronts (mentioned in chapter 3 for Earth) in Mars meteorological conditions. This can be another possible future work. Future work can be conducted to employ available data, to help validate the model results.

A better simulation of the size and thickness of the artificial permanent south polar cap will be another step in future works. Also possible future work can be carried out with a study of the other physical and meteorological processes (e.g. formation of "snow" and "frost") which can control the spatial and temporal variation of the albedo and the in-homogeneities of Martian south polar CO_2 ice cap. Study of the ice cap paleoclimatology is another interest.

Finally it would be useful to attempt to better simulate the Viking Lander 1 and 2 surface pressure cycle with the model rather the standard model version.

References

Ahrens, C. D. (2007). *Meteorology today: An introduction to weather, climate and the environment.* Canada: Thomson Higher Education.

Akingunola, A. (2008). Martian water cycle modeling with the second generation of the Global Mars Multiscale Model. PhD Thesis, York University.

Akingunola, A., McConnell, J. C., Kaminski, J., Fazel Rastgar, F., and Wu, D. (2008). The second generation of the Global Mars Multiscale Model. 6th Canadian Space Exploration Workshop, Canadian Space Agency, December 1-3, 2008.

Alson, M., and McEwen, M. (2005). A post-Pathfinder elevation of areocentric solar coordinates with improved timing recipes for Mars seasonal/diurnal climate studies. *Planetary and Space Science, 48,* 215-235.

Banfield, D., Conrath, B. J., Smith, M. D., Christensen, P. R., and Wilson, R. J. (2003). Forced waves in the Martian atmosphere from MGS TES nadir data. *Icarus, 161(2),* 319-345.

Barlow, N. G. (2008). *Mars: An introduction to its interior, surface, and atmosphere.* New York, NY: Cambridge University Press.

Barnes, J. R. (1980). Time spectral analysis of midlatitude disturbances in the Martian atmosphere. *J. Atmos. Sci., 37,* 2002-2015.

Barnes, J. R. (1981). Midlatitude disturbances in the Martian atmosphere: A second Mars year. *J. Atmos. Sci., 38,* 225-234.

Barnes, J. R. and Tyler, D. (2007). Winter weather on Mars: The unique southern hemisphere, International conference on Mars.

Benson, J. L., Kass, D. M., Kleinböhl, A., McCleese, D. J., Schofield, J. T., and Taylor, F. W. (2010). Mars' south polar hood as observed by the Mars Climate Sounder. *J. Geophys. Res., 115(E12015).* doi:10.1029/2009JE003554

Bibring, J. P., Langevin, Y., Poulet, F., Gendrin, A., Giancarlo, B., Moroz, V., ... The OMEGA team. (2004). Perennial water ice identified in the south polar cap of Mars. *Nature, 428,* 627-630.

Briggs, G. A. (1974). The nature of the residual Martian polar caps. *Icarus, 23*, 167-191.

Byrne, S., and Ingersoll, P. (2003). A sublimation model for Martian south polar ice features. *Science, 299*, 1051-1053.

Byrne, S., Zuber, M. T., and Neumann, G. A. (2008). Interannual and seasonal behavior of Martian residual ice-cap albedo. *Planet. Space Sci., 56(2),* 194-211.

Calvin, W. M., and Martin, T. Z. (1994). Spatial variability in the seasonal south polar cap of Mars. *J. Geophys. Res., 99(E10)*, 21143-21152. doi:10.1029/94JE02011

Christensen, P. R., and Moore, H. J. (1992). *The Martian surface layer.* In: Mars. Kieffer, H.H., Jakosky, B.M., Snyder, C.W., and Matthews., M.S. (Ed.). Tucson, AZ: University of Arizon Press, 686-729.

Christensen, P. R., Bandfield, J. L., Hamilton, V. E., Ruff, S. W., Kieffer, H. H., Titus, T. N., ... Greenfield, M. (2001). The MGS-TES experiment: Investigation description and surface science results. *Journal of Geophysical Res., 106,* 23823-23871.

Clifford, S. M., Crisp, D., Fisher, D. A., Herkenhoff, K. E., Smrekar, S. E., Thomas, P. C. ... Zwally, H. J. (2000). The state and future of Mars polar science and exploration. *Icarus, 144,* 210-242. doi:10.1006/icar.1999.6290

Colaprete, A., Barnes, J. R., Haberle, R. M., Hollingsworth, J. L., Kieffer, H. H., and Titus, T. N. (2005). Albedo of the south pole determined by topographic forcing of atmosphere dynamics. *Nature, 435*, 184-188.

Colines, M., Lewis, S. R., and Read, P. L. (1997). Gravity wave drag in a global circulation model of the Martian atmosphere: Parameterization and validation. *Adv. Space Res., 19(8)*, 1245-1254.

Conrath, B. J., Pearl, J. C., Smith, M. D., Maguire, W. C., Christensen, P. R., Dason, S., and Kaelberer M. S. (2000). Mars Global Surveyor Thermal Emission Spectrometer (TES) observations: Atmospheric temperatures during aerobraking and science phasing, *Journal of Geophysical Res., 105(E4),* 9509-9519.

Côté, J., Gravel, S., Méthot, A., Patoine, A., Roch, M., and Staniforth, A. (1998). The operational CMC-MRB Global Environmental Multiscale (GEM) model: Part I- Design considerations and formulation. *Mon. Weather Rev. 126*, 1337-1395.

Ditteon, R., and Kieffer, H. H. (1979). Optical properties of solid CO_2: application to Mars. *J. Geophys. Res., 84*, 8294-8300.

ESA website: http://www.esa.int/esaMI/Mars_Express/index.html

Fazel Rastgar, F., Akingunola, A., McConnell J. C., and Kaminski, J. (2008). Mesoscale modeling on Mars using GM3-GV, 6th Canadian Space Exploration Workshop, Canadian Space Agency.

Fazel Rastgar, F., McConnell, J. C., and Akingunola, A. (2011). Topography and albedo impact at Martian south polar CO_2 ice cap. Fifth Mars Polar Science Conference. http://www.lpi.usra.edu/meetings/polar2011/polar2011.authorindex.html

Festou, M. (Eds.). (2000). *Solar system ices.* Kluwer Academic Publishers. 477-507.

Forget, F. (1998). Mars CO_2 ice polar caps. In: Schmitt, B. et al., Solar System Ices, *Kluwer Academic*, 477-507.

Forget, F. (2004). Alien weather at the poles of Mars. *Science, 306*, 1298-1299.

Forget, F. (2007). *Water and climates on Mars.* In: Muriel Gargaud et al., (Eds.). Lectures in Astrobiology, Vol. II, *Adv. Astrobiol. Biogeophys.*, New York, NY: Springer Berlin Heidelberg, 103-122.

Forget, F., Pollack, J. B., and Hansen, G. B. (1995). Low brightness temperature of Martian polar caps: Co_2 clouds or low spectral emissivity?. *J. Geophys. Res., 100(E10),* 21219-21234. doi:10.1029/95JE02378

Forget, F., Hourdin, F., and Talagrand, O. (1998). CO_2 snow fall on Mars: Simulation with general circulation model, *Icarus, 131*, 302-316.

Forget, F., Hourdin, F., Fournier, R., Hourdin, C., Talagrand, O., Lewis S. R., ... Hout, J. (1999). Improved general circulation models of the Martian atmosphere from surface to above 80 km. *J. Geophys. Res., 104(E10)*, 24177-24194.

Forget, F., Costard, F., and Lognonne, P. (2006). Planet Mars. Springer, Chichester, 121-179.

Giuranna, M., Grassi, D., Formisano, V., Montabone, L., Forget, F., and Zasova, L., (2008). PFS/MEX observations of the condensing CO_2 south polar cap of Mars, *Icarus, 197*, 386-402.

Glasstone, S. (1968). *The Book of Mars.* NASA SP-179.

Guo, X., Richardson, M. I., Soto, A., and Toigo, A. (2010). On the mystery of the perennial carbon dioxide cap at the south pole of Mars. *J. Geophys. Res., 115(E4).* doi:10.1029/2009JE003382

Guzewich, S. D., Talaat, E. R., and Waugh, D. W. (2012). Observations of planetary waves and nonmigrating tides by the Mars Climate Sounder. *J. Geophys. Res., 117(E3).* doi:10.1029/2011JE003924.

Haberle, R., Joshi, M., Murphy, J., Barnes, J., Schofield, J., Wilson, G., ... Schaeffer, J. (1999). General circulation model simulations of the Mars Pathfinder atmospheric structure investigation/ meteorology data. *J. Geophys. Res., 104,* 8957-8974.
Haberle, R., Forget, F., Colaprete, A., Schaeffer, J., Boynton, W. V., Kelly, N. J., and Chamberlain, M. J. (2008). The effect of ground ice on the Martian seasonal CO_2 cycle. *Planet. Space Sci., 56(2),* 251-255. doi:10.1016/j.pss.2007.08.006

Hansen, C. J., Thomas, N., Portyankina, G., McEwen, M., Becker, T., Byrne, S., ... Mellon, M. (2010). HiRISE observations of gas sublimation-driven activity in Mars' southern polar regions: I. Erosion of the surface, *Icarus, 205,* 283-295.

Hayne, P. O., and Paige, D. A. (2009). Carbon dioxide snow cloud activity and polar winter emissivity: Mars climate sounder observations and model results. Third International Workshop on Mars Polar Energy Balance and the CO_2 Cycle, held July 21-24, 2009 in Seatde, Washington. LPI Contribution No. 1494, 23-24.

Hayne, P. O., Paige, D. A., Schofield, J. T., Kass, D. M., Kleinböhl, A., Heavens, N. G., and McCleese, D. J. (2012). Carbon dioxide snow clouds on Mars: South polar winter observations by the Mars Climate Sounder. *J. Geophys. Res., 117(E08014).* 1-23. doi:10.1029/2011JE004040

Heavens, N. G., Benson, J. L., Kass, D. M., Kleinböhl, A., Abdou, W. A., McCleese, D. J., ... Wolkenberg, P. M. (2010). Water ice clouds over the Martian tropics during northern summer. *Journal of Geophysical Res., 37(18),* L18202. doi:10.1029/2010GL044610

Heavens, N. G., McCleese, D. J., Richardson, M. I., Kass, D. M., Kleinböhl, A., and Schofield, J. T. (2011). Structure and dynamics of the Martian lower and middle atmosphere as observed by the Mars Climate Sounder: 2. Implications of the thermal structure and aerosol distributions for the mean meridional circulation. *J. Geophys. Res., 116(E01010),* 1-14. doi:10.1029/2010JE003713

Hinson, D. P., Wilson, R. J., Smith, M. D., and Conrath, B. J. (2003). Stationary planetary waves in the atmosphere of Mars during southern winter. *J. Geophys. Res., 108(E1).* doi:10.1029/2002JE001949

Hollingworth, J. L. (2007). Cyclogenesis and frontal waves on mars, seventh international conference on Mars. http://www.lpi.usra.edu/meetings/7thmars2007/

Hollingsworth, J. L., Haberle, R. M., Barnes, J. R., Bridges, A. F. C., Pollack, J. B., Lee, H. and Schaeffer, J. (1996). Orographic control of storm zones on Mars. *Nature, 380,* 413-416.

Hollingworth, J. L., Kahre, M. A., and Haberle, R. M. (2007). Mars dust: Atmospheric effects of large-scale extra tropical cyclogenesis and frontal waves. Seventh international conference on Mars. http://www.lpi.usra.edu/meetings/7thmars2007/

Hollingworth, J. L., Kahre, M. A., and Haberle, R. M. (2008). Mars' southern hemisphere: Influences of the great impact basins on extra-tropical weather and the water cycle. Williamsburg, Virginia: Third International Workshop on The Mars Atmosphere: Modeling and Observations.

Hollingsworth, J. L., and Kahre, M. A. (2010). Extratropical cyclones, frontal waves, and Mars dust: Modeling and considerations. *Geophys. Res. Lett., 37(22).* doi: 10.1029/2010GL044262

Holstag, A. A. M., and Boville, B. A. (1993). Local versus nonlocal boundary layer diffusion in a global climate mode. *J. Atmos. Sc., 48*, 1690-1698.

Holstein-Rathlou, C., Gunnlaugsson, H. P. , Merrison, J. P., Bean, K. M., Cantor, B. A., Davis, J. A., ... Goetz, W. (2010). Winds at the Phoenix landing site. *J. Geophys. Res., 115(E00E18).*

Holton, J. T. (2004). *An introduction to dynamical meteorology.* Elsevier.

Hourdin, F., Van, P. L., Forget, F., and Talagrand, O. (1993). Meteorological variability and annual surface pressure cycle on Mars. *J. Atmos. Sc., 50*, 3625-3640.

Hu, R., Cahoy, K., and Zuber, M. T. (2012). Mars atmospheric CO_2 condensation above the north and south poles as revealed by radio occultation, climate sounder, and laser ranging observations. *J. Geophys. Res., 117 (E07002),* 1-21. doi:10.1029/2012JE004087.

Hunt, G. E., and James, P. B. (1979). Martian extratropical cyclones. *Nature, 278.*

Jakosky, B. M. and Haberle, R. M. (1992). *The seasonal behavior of water on Mars.* Kieffer, H. H., Jakosky, B. M., Snyder, C. W., and Matthews, M. S. (Eds.). U. Arizona Press. 969-1016.

James, P. B. (1983). Condensation phase of the Martian south polar cap. Bull. *Am. Astron. Soc., 15*, 846-847.

James, P. B., Briggs, G., Barnes, J., and Spruck, A. (1979). Seasonal recession of Mars' south polar cap as seen by Viking. *J. Geophys. Res., 84(B6),* 2889-2922.

James, P. B., and North, G. R. (1982). The seasonal CO_2 cycle on Mars: An application of an energy balance climate model, *J. Geophys. Res., 87*, 10271-10283.

James, P. B., Keiffer, H. H., and Paige, D. A. (1992). The seasonal cycle of carbon Dioxide on Mars. University of Arizona press, Tucson, 934-968.

James, P. B., Bonev, B. P., and Wolff, M.J. (2005). Visible albedo of Mars south polar cap: 2003. HST observation, *Icarus, 174(2)*, 596-599.

James, P. B., Hansen, G. B., and Titus, T. N. (2005). The carbon dioxide cycle. *Advances in Space Research, 35*, 14-20.

Jian, J. J., and Ip, W. H. (2009). Seasonal patterns of condensation and sublimation cycles in the cryptic and non-cryptic regions of the South Pole. *Advanced in Space Research, 43,* 138-142.

Kelly, N. J., Boynton, W. V., Kerry, K., Hamara, D., Janes, D., Reedy, R. C., ... Haberrle, R. M. (2006). Seasonal polar carbon dioxide frost on Mars: CO_2 mass and columnar thickness distribution. *J. Geophys. Res., 111(E03S07),* 1-12. doi:10.1029/2006JE002678

Kieffer, H. H., Martin, T. Z., Peterfreund, A. R., and Jakosky, B. M. (1977). Thermal and albedo mapping of Mars during the Viking primary mission. *J. Geophys. Res. 82,* 4249-4291.

Kieffer, H. H., *Jakosky,* B. M., and Conway, W. S. (1992). *Mars (Space Science Series).* Tucson, AZ: University of Arizona Press.

Kieffer, H. H., Titus, T. N., Mullins, K. F., and Christensen, P. R. (2000). Mars south polar spring and summer behavior observed by TES: Seasonal cap evaluation controlled by frost grain size. *J. Geoohys. Res.105,* 9653-9700.

Kieffer, H. H., Christensen, P. R., and Titus, T. N., (2006). CO_2 jets formed by sublimation beneath translucent slab ice in Mars' seasonal south polar ice cap. *Nature, 442(7104)*, 793-796.

Kuroda, T., Medvedev, A. S., Kasaba, Y., and Hartogh, P. (2013). Carbon dioxide ice clouds, snowfalls, and baroclinic waves in the northern winter polar atmosphere of Mars, *Geophys. Res. Lett., 40,*1484-1488. doi:10.1002/grl.50326

Langevin, Y., Poulet, F., Vincendon, M., Bibring, J. P., and Gondet, B. (2006a). Observations by omega/mex of CO_2 and H_2O frosts in the seasonal caps during a full Martian year (01/2004 -11/2005). Second workshop on Mars atmosphere modelling and observations held February 27-March 3 in Granada, Spain. LMD, IAA, AOPP, CNES, ESA. 423.

Langevin, Y., Doute, S., Vincendon, M., Poulet, F., Bibring, J. P., Gondet, B., ... Forget, F. (2006b). No signature of clear CO_2 ice from the 'cryptic' regions in Mars' south seasonal polar cap. *Nature, 442(7104).*790-792.

Langevin, Y., Bibring, J. P., Montmessin, F., Forget, F., Vincendon, M., Douté, S., ... Gondet, B. (2007). Observations of the south seasonal cap of Mars during recession in 2004-2006 by the OMEGA visible/near-infrared imaging spectrometer on board Mars Express. *J. Geophys. Res.,112(E08S12)*, 1-32. doi:10.1029/2006JE002841

Laprise, R., and Girard, C. (1990). A spectral general circulation model using piecewise-constant finite-element representation on a hybrid vertical coordinate system. *J. Climate, 3,* 32-52.

Leonard, G. J., and Tanaka, K. L. (2001). Geologic map of the Hellas region of Mars: U.S. Geological Survey Geologic Investigations Series I–2694. pamphlet 10 p., 1 plate, scale 1:4,336,000, available at http://pubs.usgs.gov/imap/i2694/

Leovy, C. B. (1979). Martian Meteorology. *Annual Review of Astronomy and astrophysics, 17*, 387-413.

Leovy, C. B. (2001). Weather and climate on Mars. *Nature, 412,* 245-249.

Lian, Y., Richardson, M. I., Newman, C. E., Lee, C., Toigo, A. D., Mischna, M. A., and Campin, J. (2012). The Ashima/MIT Mars GCM and argon in the Martian atmosphere. *Icarus, 218(2),* 1043-1070.

Liou, K. N. (1974). Analytic two-stream and four stream solutions for radiative transfer. *J. Atmos. Sci., 31,* 1473-1475.

Liou, K. N. (1992). *Radiation and cloud processes in the atmosphere.* (487). New York, NY: Oxford University Press.

Litvak, M. L., Mitrofanov, I. G., Kozirev, A. S., Sanin, A. B., Tretyakov, V. I., Boynton, W. V., ... Saunders, R. S. (2005). Modeling of Martian seasonal caps from HEND/ODYSSEY data. *Advances in Space Research, 36*, 2156- 2161.

L´opez-Valverde, M. A., Edwards, D. P., L´opez-Puertas, M., and Rold´an, C. (1998). Non-local thermodynamic equilibrium in general circulation models of the Martian atmosphere 1. Effects of the local thermodynamic equilibrium approximation on thermal cooling and solar heating. *J. Geophys. Res., 103,* 16799-16812.

Määttänen, A., and Savijarvi, H. (2004). Sensitivity tests with a one-dimensional boundary layer model of Mars. *Bound. Layer Met., 113*, 305-320.

Malin, M. C., Caplinger, M. A., and Davis, S. D. (2001). Observational evidence for an active surface reservoir of solid carbon dioxide on Mars. *Science, 294,* 2146-2148.

Marlin, M. C. and Edgett, K. S. (2009). 40th lunar and planetary science conference. http://www.lpi.usra.edu/meetings/lpsc2009/

McCleese, D. J., Schofield, J. T., Taylor, F. W., Abdou, W. A., Aharonson, O., Banfield, D., ... Zurek, R. W. (2008). Intense polar temperature inversion in the middle atmosphere on Mars. *Nature Geosci., 1(11),* 745-749. doi:10.1038/ngeo332

McFarlane, N.A. (1987). The effect of orographically excited gravity wave drag on the general circulation of the lower stratosphere and troposphere. *J. Atmos.Sci., 44,* 1775-1800.

McGraw-Hill. (2003). Rossby wave. In *McGraw-Hill Dictionary of Scientific and Technical Terms.* (6th ed.). New York, NY: McGraw-Hill Professional.
McLandress C. and McFarlane N.A. (1993). The effect of orographic gravity wave drag on quasi-stationary planetary wave dynamics in the northern hemisphere middle atmosphere in winter. *J. Atmos. Sci, 50,* 1966-1990.

Mintz, Y. (1961). In the atmosphere of Mars and Venus publ. 994 (National Academy of Sciences- National Research Council, Washington, DC.

Mohammed, F. (2010). Atmospheric Correction of OMEGA Data from Mars Express to Detect Surface Composition, MSc. Thesis, York University.

Monin, A. S. and Obukhov, A. M. (1954). Basic laws of turbulent mixing in the atmosphere near the ground. *Tr. Akad. Nauk SSSR Geoph., 64,* 1963-1987.

Montmessin, F., Bertaux, J. L., Quémerais, E., Korablev, O., Rannou, P., Forget, F., ... Dimarellis, E. (2006). Sub visible CO_2 ice clouds detected in the mesosphere of Mars. *Icarus, 183*, 403-410.

Moudden, Y., and McConnell, J. C. (2005). A new model for multiscale modeling of the Martian atmosphere, GM3. *J. Geophys. Res, 110(E04001),* 1-13. doi:10.1029/2004JE002354

Moudden, Y., McConnell, J. C., Beagley, S. R., Lopez-Valverde, M. A., and Lopez Puertas, M., (2005). Meteorological results from the Global Mars Multiscale Model at the Viking 1 Lander site. *Advances in Space Research, 36(11),* 2169-2175.

Murray, B., Soderblom, L. A., Cutis, J., Sharp, R. P., Milton D. J., and Lrighton R. B. (1972). Geological framwork of the south polar region of Mars, *Icarus, 17,* 328-345.

NASA web site: http://www.nasa.gov/mission_pages/mars/main/index.html

Nelli, S. M., Murphy, J. R., Feldman, W., and Schaeffer, J. (2009). Characterization of the nighttime low-latitude water ice depositsin the NASA Ames Mars General Circulation Model 2.1 under present-day atmospheric conditions. *J. Geophys. Res., 114(E11003),* 1-12. doi:10.1029/2008JE003289

Ogohara, K., and Satomura, T. (2008). Northward movement of Martian dust localized in the region of the Hellas Basin, *Geophys. Res. Lett., 35(L13201)*, 1-6. doi:10.1029/2008GL034546

Paige, D. A., Herkenhoff, K. E., and Murray, B. C. (1990b). Mariner 9 observations of the south polar cap of Mars: Evidence for residual CO_2 frost. *J. Geophys. Res., 95,* 1319-1335.

Paige, D. A., and Wood, S. E. (1992). Modeling the Martian seasonal CO_2 cycle 2. interannual variability, *Icuras, 99(1),* 15-27.

Parish, H. F., Schubert, G., Hickey, M. P., and Waltersceid, R. L. (2009). Propagation of tropospheric gravity waves into the upper atmosphere of Mars, *Icarus, 203*, 28-37.

Petrosyan, A., Galperin, B., Larsen, S. E., Lewis, S. R., *Määttänen, A., Read, P. L., ...* Vázquez, L. (2011). The Martian atmosphere boundary layer. *Rev. Geophys., 49(RG3005),* 1-46.

Pettengill, G. H., and Ford, P. G. (2000). Winter clouds over the north Martian polar cap. *Geophys. Res. Lett., 27,* 609-612.

Phillips, R. J., Davis, B. J., Tanaka, K. L., Byrne, S., Mellon, M. T., Putzig, N. E., ... Sue, R. (2011). Massive CO_2 Ice Deposits Sequestered in the South Polar Layered Deposits of Mars. *Science, 332(6031),* 838-841. doi:10.1126/science.1203091

Pielke, R. A. (1990). *Mesoscale meteorological modeling.* San Diego, CA: Academic Press Inc.

Piqueux, S., Byrne, S., and Richadrson, M. I. (2003). Sublimation of Mars's southern seasonal CO_2 ice cap and the formation of spiders. *J. Geophys. Res.,108,* 1-9.

Plaut J. J., Picardi, G., Ivanov, A. B., Milkovich, S. M., Cicchetti, A., Kofman, W., ... Edenhofer, P. (2007). Subsurface radar sounding of the south polar layered deposits of Mars. *Science, 316(5821),* 92-95. doi: 10.1126/science.1139672

Plescia, J. B. (2004). Morphometric properties of Martian volcanoes. *J. Geophys. Res., 109(E03003).* doi:10.1029/2002JE002031

Pollack, J. B., Haberle, R. M., Schaeffer, F., and Lee, H. (1990). Simulation of the general circulation of the Martian atmosphere: 1. Polar processes. *J. Geophys. Res., 95(B2),* 1447-1473. doi:10.1029/JB095iB02p01447

Pollack, J. B., Haberle, R. M., Murphy, J. R, Schaeffer, J., and Lee, H. (1993). Simulations of the general circulation of the Martian atmosphere: 2. Seasonal pressure variations, *J. Geophys. Res., 98,* 3149-3181. doi:10.1029/92JE02947

Putzig, N. E., Mellon, M. T., Kretke, K. A., and Arvidson, R. E. (2005). Global thermal inertia and surface properties of Mars from the MGS mapping mission. *Icarus, 173,* 325-341.

Putzig, N. E., and Mellon, T. (2007). Apparent thermal inertia and surface heterogeneity of Mars, *Icarus, 191(1),* 68-94.

Read, P. L., and Lewis, S. R. (2004). *The Martian Climate Revisited.* New York, NY: Springer.

Renyu, H., Cahoy, K., and Zuber M. T. (2012). Mars atmospheric CO_2 condensation above the north and south poles as revealed by radio occultation, climate sounder, and laser ranging observations. *Journal of Geophysical Research: Planets, 117(E7),* 1991-2012.

Saito, R. (2006). Influence of the surface on the atmospheric circulation of Mars: Study with a general circulation model. PhD Thesis, International Max Planck Research School.

Saucier, W. J. (2003). *Principles of Meteorological Analysis.* Mineola, NY: Dover Publications.

Schofield, J. T., Barnes, J. R., Crisp, D., Haberle, R. M., Larsen, S., Magalhães, J. A., ... Wilson G. (1997). The Mars pathfinder atmospheric structure investigation/Meteorology (ASI/MET) experiment. *Science, 278(5344),* 1752-1758.

Schorghofer, N. (2007). Dynamics of ice ages on Mars. *Nature, 449,*192-195.

Smith, D. E., Zuber, M. T., and Neumann, G. A. (2001). Seasonal Variations of Snow Depth on Mars. *Science, 294,* 2141-2146.

Smith, D. E., Zuber, M.T., Solomon, S. C., Phillips, R. J., Head, J. W., Garvin, J. B., ... Duxbury, T. C. (1999). The global topography of Mars and implications for surface evolution. *Science, 284(5419),* 1495-1503. doi: 10.1126/science.284.5419.1495

Smith, M., Conrath, B., Pearl, J., and Christensen P. (2002). Thermal emission spectrometer observations of Martian planet-encircling dust storm 2001A. *Icarus 157(1),* 259-263.

Smith, M. D. (2002). The annual cycle of water vapor on Mars as observed by the Thermal Emission Spectrometer. *J. Geophys. Res., 107,* 5115-5134.

Smith M. D. (2004). Interannual variability in TES atmospheric observations of Mars during 1999-2003. *Icarus, 167,* 148-165.

Smith, M. D., Wolff, M. J., Lemmon, M. T., Spanovich, N., Banfield, D., Budney, C.J., ... Squyres, S.W. (2004). First atmospheric science results from the Mars Exploration Rovers Mini-TES. *Science, 306,* 1750-1753.

Sprague, A. L., Boynton, W. V., Forget, F., Lian, Y., Richardson, M. I., Starr, R. D., Metzger, A. E., Hamara, D., and Economou, T. E. (2012). Inter annual similarity and variation in seasonal circulation of Mars' atmospheric Ar as seen by the Gamma Ray

Spectrometer on Mars Odyssey. *J. Geophys. Res., 117(E04005),* 1-13. doi:10.1029/2011JE003873

Tanaka, K. L., and Scott, D. H. (1987). *Geologic map of the polar regions on Mars.* Flagstaff, AZ: U.S. Geological Survey.

Tellmann, S., Pätzold, M., Häusler, B., Hinson, D. P., and Tyler, G. L. (2013). The structure of Mars lower atmosphere from Mars Express Radio Science (MaRS) occultation measurements, *J. Geophys. Res. Planets, 118,* 306-320. doi:10.1002/jgre.20058

Thomas, P. C., Marlin, M. C., Edgett, K. S., Carr, M. H., Hartman, W. K., Ingresoll, A. P., ... Sullivan, R. (2000). North-South geological differences between the residual polar cap on Mars. *Nature, 404,* 161-164.

Thomas, P. C., James, P. B., Calvin, W., Haberle, R. M., and Marlin, M. C. (2009). Residual south polar cap of Mars: Interpretation and puzzles, 40th lunar and planetary science conference. http://www.lpi.usra.edu/meetings/lpsc2009/

Titus, T. N., Kieffer, H. H., Mullins, K. F., and Christensen, P. R. (2001). TES premapping data: Slab ice and snow flurries in the Martian north polar night. *J. Geophys. Res., 106,* 23181-23196.

Titus, T. N., Kieffer, H. H., and Christensen, P. R. (2003). Exposed water ice discovered near the South Pole of Mars. *Science, 299,* 1048-1051.

Toigo A. D., Richardson, M., Wilson, R., Wang, H., and Ingersoll, A., (2002). A first look at dust lifting and dust storms near the south pole of Mars with a mesoscale model. *J. Geophys. Res., 107(E7),* 1-13. doi:10.1029/2001JE001592

Toon, O. B., McKay, C. P., Ackerman, T.P., and Santhanam, K. (1989). Rapid calculation of radiative heating rates and photodissociation rates in inhomogeneous multiple scattering atmospheres. *J. Geophys. Res., 94(D13),* 16287-16301.

Vincendon, M., Langevin, Y., Poulet, F., Bibring, J. P., Gondet, B., and Joulet, D. (2007). Dust aerosols above the south polar cap of Mars as seen by OMEGA. *Icarus, 196,* 488-505.

Wang, H. (2004). Global observations of Martian clouds with the Mars orbiter camera of the Mars global surveyor spacecraft. PhD Thesis, California Institute of Technology.

Wang, H., Toigo, A. D., and Richardson, M. I. (2011). Curvilinear features in the southern hemisphere observed by Mars Global Surveyor Mars Orbiter Camera. *Icarus, 215,* 242-252.

Woiceshyn, P.M. (1974). Global seasonal atmospheric fluctuations on Mars. *Icarus, 22,* 325-343.

Yokohata, T., Odaka, M., and Kuramato, K. (2002). Role of H_2O and CO_2 Ices in Martian climate changes, *Icarus, 159,* 439-448.

Yamashita, Y., Kuroda, T., and Takahashi, M. (2007). Maintenance of zonal wind variability associated with the annular model on Mars. *Geophys. Res. Lett., 34(L16819),* 1-5. doi:10.1029/2007GL030069

Zuber M. T., Smith D. E., Solomon S.C., Abshire J.B., Afzal R.S., Aharonson O., ... Duxbury T. C. (1998). Observations of the north polar region of Mars from the Mars Orbiter Laser Altimeter. *Science, 282(5396),* 2053-2060.

Zurek, R. W., Barnes J. R., Haberle, R. M., Pollack, J. B., Tillman, J. E., and Leovy, C. B. (1992). Dynamics of the atmosphere of Mars. *Mars (A93-27852 09-91)*, 835-933.